ABSTRACT

Title of dissertation: DESIGN, MODELING, AND FABRICATION OF MICROROBOT LEGS

Dana Elise Vogtmann
Doctor of Philosophy, 2016

Dissertation directed by: Professor Sarah Bergbreiter
Department of Mechanical Engineering

This dissertation presents work done in the design, modeling, and fabrication of magnetically actuated microrobot legs.

Novel fabrication processes for manufacturing multi-material compliant mechanisms have been used to fabricate effective legged robots at both the meso and micro scales, where the meso scale refers to the transition between macro and micro scales. This work discusses the development of a novel mesoscale manufacturing process, Laser Cut Elastomer Refill (LaCER), for prototyping millimeter-scale multi-material compliant mechanisms with elastomer hinges. Additionally discussed is an extension of previous work on the development of a microscale manufacturing process for fabricating micrometer-sale multi-material compliant mechanisms with elastomer hinges, with the added contribution of a method for incorporating magnetic materials for mechanism actuation using externally applied fields.

As both of the fabrication processes outlined make significant use of highly com-

pliant elastomer hinges, a fast, accurate modeling method for these hinges was desired for mechanism characterization and design. An analytical model was developed for this purpose, making use of the pseudo rigid-body (PRB) model and extending its utility to hinges with significant stretch component, such as those fabricated from elastomer materials. This model includes 3 springs with stiffnesses relating to material stiffness and hinge geometry, with additional correction factors for aspects particular to common multi-material hinge geometry. This model has been verified against a finite element analysis model (FEA), which in turn was matched to experimental data on mesoscale hinges manufactured using LaCER. These modeling methods have additionally been verified against experimental data from microscale hinges manufactured using the Si/elastomer/magnetics MEMS process.

The development of several mechanisms is also discussed: including a mesoscale LaCER-fabricated hexapedal millirobot capable of walking at 2.4 body lengths per second; prototyped mesoscale LaCER-fabricated underactuated legs with asymmetrical features for improved performance; 1 cm^3 LaCER-fabricated magnetically-actuated hexapods which use the best-performing underactuated leg design to locomote at up to 10.6 body lengths per second; five microfabricated magnetically actuated single-hinge mechanisms; a 14-hinge, 11-link microfabricated gripper mechanism; a microfabricated robot leg mechansim demonstrated clearing a step height of 100 micrometers; and a 4 mm x 4 mm x 5 mm, 25 mg microfabricated magnetically-actuated hexapod, demonstrated walking at up to 2.25 body lengths per second.

DESIGN, MODELING AND FABRICATION OF MICROROBOT LEGS

by

Dana Elise Vogtmann

Dissertation submitted to the Faculty of the Graduate School of the
University of Maryland, College Park in partial fulfillment
of the requirements for the degree of
Doctor of Philosophy
2016

Advisory Committee:
Associate Professor Sarah Bergbreiter, Chair/Advisor
Professor Hugh Bruck
Professor S.K. Gupta
Associate Professor Jeff Shultz
Professor Elisabeth Smela

Acknowledgments

There are several individuals who deserve thanks for their aid and support during the completion of this work. First and foremost, I would like to thank my advisor, Professor Sarah Bergbreiter. Without her invaluable expertise, guidance, and mentorship, this work would not have been possible. I would also like to thank Professor S.K. Gupta for all his insights and advice, particularly in the field of compliant mechanisms and mechanism design.

I would like to thank my labmates at the Microrobotics Laboratory, Ryan St. Pierre, Ivan Penskiy, Alexi Charalambides, David Ma, Simpson Chen, and Hee Sup Shin for all their helpful feedback, ideas, collaborations, and conversation. I would also like to thank an alum of MRL, Aaron Gerratt, whose training and knowledge of microfabrication techniques were of great help to me.

I would like to thank my dissertation committee for their expertise and input on this work, including Professors Hugh Bruck, S.K. Gupta, Jeffrey Shultz, and Elisabeth Smela. Your words of encouragement and advice will stay with me.

I would also like to thank the staff at the Maryland NanoCenter FabLab, including John Abrahams, Jon Hummel, Mark Lecates, and Tom Loughran. My questions never went unanswered, and equipment training was always a joy rather than a chore.

Finally, I would like to thank my friends and family for all their encouragement. In particular I want to thank my fiancé, Adam Lee, whose constant, unwavering support has allowed me to see this dissertation through to the end.

Table of Contents

List of Tables

List of Figures

Chapter 1

Introduction

This dissertation presents work done in the design, modeling, and fabrication of magnetically actuated micro robot legs. Effective design and characterization methods for leg mechanisms are important for the development of capable legged robots at any scale. On the micro scale, however, fabrication becomes a particular challenge as well, and a thorough understanding of the unique complexities of microscale systems is necessary to design effective mechanisms. This work applies these considerations to the development of micro robotic legs, toward the goal of developing highly-capable legged micro robots. Micro robots are defined here as robots of only a few mm in length or smaller, with mainly μm scale features.

Legged micro robots with capabilities approaching those of ants or other small legged insects would allow networks of tiny, fast, strong platforms that can maneuver over obstacles several times their size to be deployed as sensor networks, collaborative builders, or search and rescue teams. Ultimately, to realize this goal of ant-like robotic networks, many technologies will need to converge, such as power, actuation, sensing, communication, and–the focus of this dissertation–capable microscale leg mechanisms. Leg mechanisms for ant-like robots would be able to carry the micro robotic platform at about 10 body length per second, navigate over rough terrain

without tripping or breaking, and carry the platform's weight and a payload of the same mass or more. With these requirements in mind, investigation toward these micro robotic legs can be carried out.

First, in order to understand and benefit from the advancements previously made in small scale robotic legs, a solid foundation in the current state of the art in miniature mobile robots is required.

1.1 Previous work in miniature mobile robotics

There has been much work done in the area of miniature legged robotics. Most of the current work is done at the meso scale– where meso scale robots are a few cm in length with mainly mm-scale features. The strides taken toward miniaturization at this level can be used to inspire and inform designs for further miniaturization.

iSprawl, the smallest of the Sprawl family of robots, is a 0.3 kg running hexapod fabricated using Shape Deposition Manufacturing (SDM), a process where multiple materials are deposited and milled on one another to create multi-material compliant mechanisms with embedded components. It is actuated using electrically driven push/pull cables to extend and retract its legs. This push/pull mechanism combined with the correct sprawl angle, a passive return hip, and a resonant driving frequency drive iSprawl. It is capable of running at speeds up to 2.3 m/s (15 body lengths per second). iSprawl is on the larger end of the meso scale, but it is worth mentioning here for several reasons. The use of a new manufacturing method–SDM–increases

robustness and decreases footprint by embedding hard components such as actuators into relatively soft materials which additionally act as structural components in the robot. The leg mechanisms also employ underactuation–that is, they have more degrees of freedom than actuators–which simplifies the leg design and removes the need for further bulky actuators. Additionally, the Sprawl family of robots takes inspiration from legged insects–namely the cockroach–in tuning leg and gait parameters, and have been used to investigate locomotion models such as the Spring Loaded Inverted Pendulum (SLIP) model[7]. Each of these aspects improves the performance of iSprawl in some way by reducing mass, increasing mobility, or informing the authors on the best gait parameters.

The Dynamic Autonomous Sprawled Hexapod (DASH) is a 16.2 g hexapedal walker fabricated using (a scaled up version of) Smart Composite Microstructures (SCM) to create foldable compliant mechanisms. It is actuated using a single DC motor and a differential drive mechanism, and a small SMA SmartServo to flex the frame to induce turning. It is capable of running at speeds up to 1.5 m/s (15 body lengths per second) [8]. Like iSprawl, DASH uses a new manufacturing method–in this case SCM–to create integrated structural and flexural components from lightweight materials without the need for fasteners, and which incorporates compliance into the legs for increased robustness, a biologically mimetic mass to relative leg stiffness ratio, and improved obstacle clearance near the robot's hip height. Although the legs are not underactuated, DASH reduces the number of actuators by reducing the

degrees of freedom, with the actuation for the legs coming from a single motor in the body, differentially driving a hip linkage for each leg over a single degree of freedom[7]. This reduces the mass of the system, but sacrifices some functionality. Again, the use of new fabrication processes, integrated compliance, minimal actuation, and investigation of biologically relevant locomotion models have helped improve the performance of this small robot.

The Harvard Ambulatory Micro Robot VP (HAMR-VP) is a 1.27 g quadrupedal walker also fabricated using SCM. It is driven using six piezoelectric actuators (2 for swing, and 4 for lift of each leg), and is capable of walking at speeds of up to 44.2 cm/s (10.1 body lengths per second). Like DASH, HAMR-VP uses SCM for lightweight, compliant mechanism design. Additionally, HAMR-VP does not use the scaled up SCM–meaning that the process is a very high-resolution one capable of producing extremely small mechanisms. Again, HAMR-VP is not underactuated, but the number of degrees of freedom was reduced from the nominal 8 to 6 via the actuation system where the swing of two legs is handled by a single actuator. It is also stated that HAMR-VP is intended for future use as a research platform into biologically inspired gait mechanics, and that the development of an insect-scale robot with similar performance characteristics was a driving factor in the robot's development [9]. New, small-scale compliant mechanism manufacturing methods and minimized actuation methods have improved the performance of HAMR-VP, and biologically-inspired testing has motivated its design.

The Robotic Autonomous Crawling Hexapod (RoACH) is a 2.4 g hexapedal walker also fabricated using SCM. It is actuated using two linear actuators–Shape Memory Alloy (SMA) coils with passive return mechanisms–and is capable of crawling at speeds up to 3 cm/s (approximately 1 body lengths per second) [10]. RoACH also uses SCM, allowing integrated structural and flexural components to be fabricated at a very small scale.

Mini-Whegs is a miniature quadrupedal robot that uses a different kind of leg, the wheel-leg, which uses rotating spokes to combine the benefits of wheels and legs. Several versions of Mini-Whegs have been developed. Some of its capabilities across different versions include wall climbing, jumping using an onboard mechanism separate from the legs, and running over 10 body lengths per second [11], [12]. Although Mini-Whegs is not especially biomimetic, several of its functions are biologically inspired–demonstrating that the abilities of biological systems can inspire very functional implementations in robotics without requiring that the exact form factor is retained.

On the micro scale, existing legged robots still require further development to reach near ant-like capabilities, but their achievements are impressive at this scale. A 10 mg solar-powered polysilicon microrobot, fabricated by Hollar et al., was able to demonstrate autonomous push-ups on two legs. This robot was fabricated with incorporated motors, control electronics, and solar cells for power. The legs were two silicon beams with rigid polysilicon hinges that allowed them to bend out of plane.

One robot was able to shuffle 3 mm to one side over 8 minutes, but the robot did not achieve forward motion [13].

A roughly 80 mg silicon micro robot with four legs, fabricated by Ebefors et al., was able to achieve forward motion. It was driven by thermal actuation of polyimide hinges to raise and lower forward- and backward-facing legs in sequence to walk forward. The use of polymer hinges also improved the durability of the legs. An example of this robot driven using offboard power was able to achieve speeds of 6 mm/s, or 0.4 body lengths per second [14].

More recently, two PZT micro robots were developed to investigate the dynamics of contact interactions in micro robotic legs. These two robots, a quadruped and a hexapod, respectively use off-the shelf or assembled lead zirconium (PZT) piezoelectric biomorph structures to created vertical motion in their legs. As these are mainly test structures, a horizontal component has not yet been incorporated, so forward motion has not been demonstrated [15].

Other micro scale robots include magnetic robots, such as the stick-slip locomotion-based Mag-μBots, which are actuated using an externally applied magnetic field [16]. Electrostatically actuated robots have been developed using a scratch drive actuators connected to a steering arm with clever control schemes on a specialized surface [17]. A combination of electrostatic clamping and magnetic fields applied at resonance are employed for actuation of ETH Zurich's MagMites [18]. Finally, jumping robots are also in development, such as the energetic nanoporous-silicon powered autonomous

thruster, and the unactuated prototype mechanism with mechanical energy storage in a spring leg, both featured in [19], [20], [21]. Each of these robots uses actuation and locomotion methods not typically seen at the macro scale. These locomotion methods are allowed either by the physics of microscale systems (as in the electrostatic attraction based systems or the jumpers which depend on extremely low mass) or by the small working areas which allow them to be actuated by close-range external fields (as in the magnetic systems). Many are also fabricated using novel fabrication processes, for incorporating active or compliant materials.

There has been much excellent work in the field of small legged robotics and micro robotics. However, legged micro robots have yet to be developed with physical capabilities approaching those found in nature. Figure 1.1 shows the locomotive performance of some of the current work compared to a selection of insect locomotion, along with the size/speed range that this work ultimately aims to move toward. This previous work toward the goal of insect-like performance suggests that novel fabrication methods with integrated compliant materials, accurate models of leg behavior, as well as novel, bio-inspired leg designs are useful for successful small-scale robotic locomotion. These have not all been present in previous legged microrobots. With these conclusions in mind, in depth investigation of legged locomotion on the micro scale is still required.

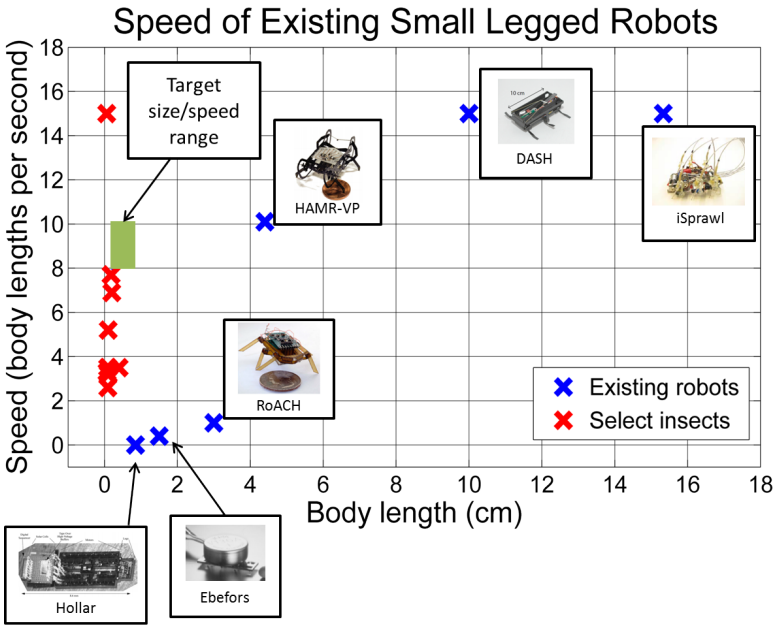

Figure 1.1: Speed vs. Body length of existing small robots, select insects, target size/speed range that this work aids to move toward. Data on selected insects are from [1], [2], [3],[4], [5], and [6].

1.2 Robot Legs at the Micro Scale

Locomotion at the micro scale is a challenging problem. Robots, on the macro or micro scale, could potentially crawl, walk, run, jump, or roll on wheels, but the choice at the micro scale is affected by several factors. Space for on-board power is limited, so cost of transport (CoT) must be low. Even mildly rough surfaces such as carpet or a concrete sidewalk become difficult terrain to navigate. Small objects become difficult obstacles that must be avoided or scaled. Due to scaling factors, the physics involved can be unintuitive, and the fabrication and physical implementation of mechanisms and actuators can be difficult to successfully execute.

Legs for walking or running provide an attractive option for locomotion of micro robots when each of these factors is addressed. Legged locomotion, whether walking or running, has a low CoT compared to jumping [22]. It also has the advantage over crawling and wheeled locomotion in rough terrain navigation. Walking has an advantage over running in ease of execution due to slower actuation speeds and reduced dynamic complexity, although running has a lower CoT. Both of these are modes of legged locomotion, however, and both have the implementation advantage over wheeled locomotion due to the difficulty of fabrication and problems with friction and wear in micro scale rotary systems [22].

All these factors make legged locomotion attractive in theory, but there are several challenges. These include suitable fabrication processes; actuator integration; understanding and modeling of mechanisms, dynamics, and physical interactions at this scale; and design of appropriate mechanisms. Discussion of each of these challenges and potential strategies for meeting each follows.

Material choice is a limiting factor in current fabrication processes for mechanisms on the millimeter to micrometer scale. For instance, there is currently a near complete reliance on rigid, brittle materials such as silicon or gallium arsenide to fabricate micro scale mechanisms. Integration of soft or active materials, such the work done by Gerratt et. al. to incorporate polydimethylsiloxane (PDMS) features into silicon MEMS structures [23], greatly improve the ability to create small-footprint highly flexible, robust mechanisms. Actuator selection is a complex problem for micro scale

mechanisms due to expectations of performance being somewhat more difficult to predict initially, as they are dependent on the repeatability of the fabrication process. Integration can be difficult as well due to the logistics of including the fabrication of the actuator with the fabrication of the rest of the system in a single monolithic process. Many of the most successful mobile microrobots have used external methods for their actuation, foregoing the added complexity of actuator selection, integration, or tethering to an external power supply ([16], [17], [18]). Applying this approach to a walking microrobot could greatly simplify the process of initial testing at the micro scale. Further discussion of challenges and existing fabrication and actuation methods is in Chapter 2.

Modeling for compliant joints is typically done using either Finite Element Analysis (FEA) (such as in [24]), which tends to be accurate but computationally expensive, or a single-spring pseudo rigid body (PRB) model ([25]), which is computationally inexpensive but is limited to a set of assumptions for the compliant hinge that do not include significant stretching. Models incorporating stretch in the joints are required for the fabrication methods which include elastomeric joints, such as the Si-elastomer MEMS mechanisms presented in [23], which could be useful for the fabrication of micro robotic legs. A more in-depth discussion on existing models is found in Chapter 3. Current understanding of the dynamics and physical interactions at this scale are limited by the lack of testing of dynamic legged microrobots. Recently, some testing has been done in this area to develop a dynamic contact model for mi-

cro robotic legs [15]. Additionally dynamic testing and observation of untethered or partially tethered legged micro robotic systems could contribute significantly to the understanding of the dynamics of running at this scale, and improve the ability to accurately model these systems.

Ultimately, to rival biological systems at this scale, leg mechanisms for micro robots must be able to push the robot forward, move quickly enough to propel the robot forward at around 10 body lengths per second, and must clear rough terrain. Although the microfabricated robots in this work do not achieve this kind of speed, they do represent a significant leap forward toward these mobility goals, and several principles contributed toward this success. Incorporation of highly flexible joints can save room that would otherwise be required for rigid-body joints or long silicon flexures, and restricting to as few actuators as possible saves space on the robot body. Simple designs are easier to fabricate and are less likely to fail. Underactuated legs are good choices for the balance of functionality and simplicity. Bio inspiration can also be useful for the design of micro robotic leg mechanisms. Each of these topics will be discussed in more detail throughout the document.

1.3 Outline of Dissertation

The document is divided into five chapters: fabrication, modeling, mechanism design, characterization of a magnetically microfabricated mechanism, and hinge modeling for a hexapedal microrobot. Broadly, the first three chapters discuss the

work done toward the realization of magnetically actuated microrobotic mechanisms, while the final two chapters explore these realized mechanisms in detail.

Chapter 2 discusses two fabrication processes developed for miniature robots. These processes include a meso scale all-polymer prototyping process for elastomeric mechanisms. The second process is a silicon MEMS process based on the process described in [23] and [19], with the additional incorporation of magnetic materials. Chapter 3 discusses modeling of the elastomeric hinges in the miniature flexible mechanisms fabricated using these processes. This includes an FEA model as well as a pseudo rigid body (PRB) model consisting of three springs – two torsional springs and one linear spring. Chapter 4 discusses robotic mechanisms which have been designed and fabricated using the elements introduced in the previous two chapters. These include a meso scale hexapedal walking robot, an asymmetric design for planar-fabricated robot legs, and a cm^3 magnetically actuated hexapedal walking robot developed using this leg design.

Chapter 5 introduces a single-link, single-hinge magnetically actuated mechanism. The actuation method used for this mechanism is discussed, and the unactuated hinge is experimentally characterized for both static and dynamic properties. The mechanism is then characterized under magnetic actuation and its static and dynamic properties are compared with a pseudo rigid-body model of the single-link mechanism. A microscale gripper mechanism is additionally presented to demonstrate the complexity of mechanisms possible to fabricate and actuate using the methods already

discussed. Chapter 6 introduces hinge-shape variations on the single-link mechanism and statically characterizes them under magnetic actuation. FEA, Single-spring and 3-spring pseudo-rigid body models are verified against the experimental results. A magnetically actuated microfabricated asymmetric leg mechanism similar to the mesoscale leg mechanism in Chapter 4 is also presented and modeled. Finally, a walking microfabricated magnetically-actuated hexapod robot is presented. This walking robot is demonstrated walking at up to 2.25 body lengths per second, standing under loads up to 495 mg, walking under loads of up to 86 mg, and walking over varied terrain including acrylic, wetted paper, and P100 grit sandpaper.

Finally, Chapter 6 provides the conclusion to this dissertation and an itemized list of the contributions of this work.

Chapter 2

Fabrication

Large scale robots have traditionally been fabricated using machined metal or plastic components, either off-the-shelf or custom-made for a specific application. Rotational and linear motion are generally achieved through rigid-body joints such as pin or prismatic joints. At small size scales (cm-scale and below), off-the-shelf parts become less of an option, due to lack of availability as well as the difficulty in assembling multiple individual parts. Thus, at smaller size scale, custom-made parts as well as monolithic fabrication processes become more attractive options. Additionally, due to the difficulty in assembly and the increasing problem of friction and wear between the two surfaces of a rigid-body joint at small size-scales, compliant mechanisms are a much more popular choice for miniature robotic mechanisms. Some rigid-body joints can be monolithically fabricated, such as in [26], but in general compliant hinges require fewer steps to fabricate monolithically, and there is no interface between two rigid bodies to experience wear. Fatigue can be a problem for compliant mechanisms, but proper material choices can lessen this issue. The compliance of the material used to fabricate the hinges is also an issue for these miniature robotic mechanisms.

At the cm-scale, ultra-compliant materials are relatively easy to incorporate into robotic mechanisms. Meso scale fabrication methods such as Shape Deposition

Manufacturing (SDM) [27] and Smart Composite Microstructures (SCM) [28, 29] demonstrate this. SDM is a somewhat larger scale manufacturing process where layers of different materials are deposited and milled to create 3D features which can have a variety of different properties, such as very low elastic modulus, and can include embedded features such as actuators. This process has been used to create robots such as Sprawlita [30]. SCM is a smaller scale process, though its limits are above that of MEMS processes. This process consists of layering sheets of flexible materials between sheets of laser-patterned rigid materials, creating flexible hinges at the gaps in the rigid materials. The resulting 2D sheets can be folded into 3D structures. This process has been used to create walking robots such as RoACH, DASH, and the RoboBee [10, 8, 31]. This process is capable of producing very small structures, but the material choices are somewhat limited.

Additional meso-scale processes for incorporation of compliant materials include multi-material injection molding and 3D printing. Multi-material injection molding involves injecting multiple materials, usually with significantly different material properties, into one or more molds to create a single part. The injection of each material can be done simultaneously or sequentially, and the part can be molded in a single mold with separate cavities for each material or in multiple molds, with the parts moldedj from one material being moved into subsequent molds. The latter technique has been used in the design and fabrication of a small (8.0 g) compliant drive mechanism for a micro air vehicle [32]. This is an attractive option with many material

choices, but requires careful mold design in addition to the mechanism design. 3D printers with multi material capabilities such as the Objet Connex are additionally capable of producing mechanisms with complex 3-dimensional geometry with embedded compliant materials. This can also include material gradients for reduction of stress concentrations at the interface between materials, or for specific behavior from the gradient parts, as in [33]. Although a wide variety of material properties are available, mechanisms printed this way are still limited to the 3D-printable materials available for the given system. These materials are relatively new and may not be well-characterized, and the materials' dynamic properties may not be comparable to flexible materials such as PDMS.

Micro scale fabrication processes have traditionally been limited in material choice as well. When fabricating compliant mechanisms from relatively rigid materials– such as the silicon typically used for microscale structures–long, thin geometry is needed for flexibility, as demonstrated in the fabrication of microscale polysilicon bistable mechanisms by Jensen et. al. [34], or in the out-of-plane microscale lamina emergent mechanism demonstrated by Zirbel et al [35]. Though these long beams of relatively rigid material have the advantage of being quite well-characterized, they can lead to a very large footprint and contribute to the overall fragility of the mechanism. Fragility can be a problem in traditional silicon-MEMS fabrication, such as that used to fabricate the solar powered crawling microrobot discussed in the previous chapter– though this microrobot used polysilicon pin hinges rather than silicon flexures [13].

The incorporation of more compliant materials within silicon mechanisms has been demonstrated by Ebefors et al. [14] and Erdem et al. [36], who both used thermal actuation of polyimide joints, as well as Gerratt et al. [23], who incorporated PDMS features directly into silicon MEMS structures. The latter process can be used to create flexible joints with a low spring constant even with short length scales. Particles such as carbon or silver can be mixed with the incorporated elastomer to create conductive flexible parts [37]. The addition of these compliant materials improves robustness as well, as suggested by the repeated jumping/landing cycles that were possible for the mechanism demonstrated in [20].

Toward filling some of the gaps in the existing fabrication methods described, two fabrication processes were developed for the fabrication of miniature compliant robotic mechanisms, Laser Cut Elastomer Refill (LaCER), and Embedded Magnet Polymer-MEMS. The two processes are described below.

2.1 LaCER

The majority of the material in this section is taken from "Multi-Material Compliant Mechanisms for Mobile Millirobots" [38].

The primary goal of this process, Laser Cut Elastomer Refill (LACER), is to demonstrate compliant mechanisms for millirobots with a wide variety of possible materials. It is also a larger scale version of the MEMS process described in [23] and [19] and can be used to inexpensively prototype mechanisms that will be microfab-

ricated. Current processes either provide a large range of possible materials with all their available properties–modulus, viscoelasticity, yield strength, etc.–or fabrication of features down to the mm-scale. This process aims to provide both. Figure 2.1 shows several test mechanisms made using this process–they are made using a variety of different materials, and the widths of the hinges shown are less than one mm.

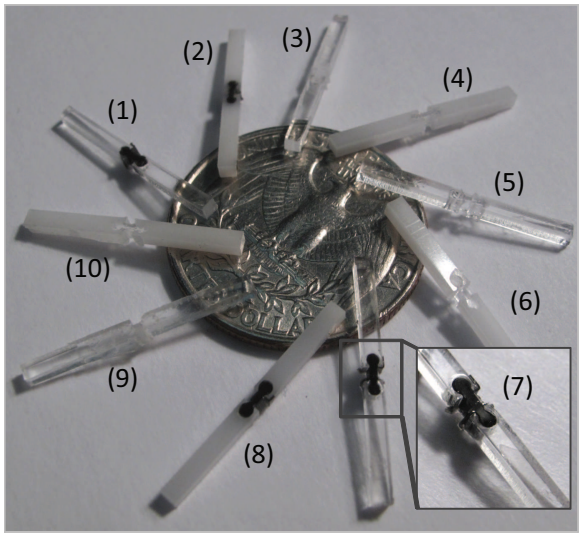

Figure 2.1: Material versatility: each sample has been fabricated using a different combination of materials. Combinations listed clockwise from (1): Acrylic with MRTV; Delrin with MRTV; Acrylic with Loctite 3525; Delrin with Loctite 3525; Acrylic with Sylgard 184 PDMS; Delrin with Sylgard 184 PDMS; Acrylic with conductive PDMS; Delrin with conductive PDMS; Acrylic with Loctite 3108; Delrin with Loctite 3108.

2.1.1 Process

The process begins with a blank sheet of the chosen rigid material (Figure 2.3a). First, a CAD drawing is made of the mechanism to be fabricated (Figure 2.2), including outlines of the rigid links, any geometry necessary for future assembly, as

well as outlines of the compliant joints. The mechanism may also be outlined for easy removal from the base material sheet. The design is then cut from the rigid material sheet using a laser cutter (Figure 2.3b). Each of the mechanisms demonstrated using this process have been cut from Delrin sheeting using a VersaLASER VLS3.60 desktop cutter with a 60 watt laser.

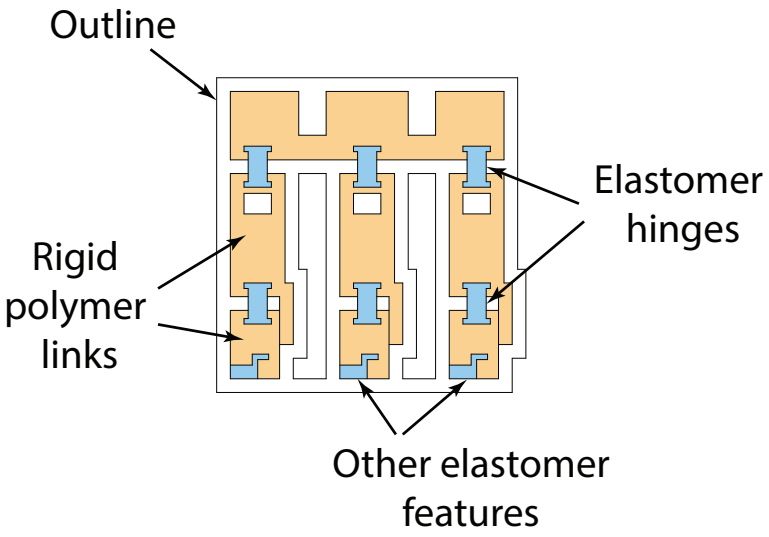

Figure 2.2: CAD outline drawing of a mechanism for LaCER fabrication. Color added for clarity.

Second, areas of the base material which are to be refilled by the joint material are removed (Figure 2.3c). This is achieved by applying a layer of adhesive tape to the back of the cut geometry to keep the majority of the parts in place while the parts to be removed are poked out from behind by a sharp pin. This is currently a manual step, but could be achieved by orienting multiple pins in place to remove all required pieces at the same time.

The third step is the application of the uncured joint material. In each of

the mechanisms presented, Dow Corning Sylgard 184 PDMS was used as the joint material. It was mixed at a ratio of 10:1 base to curing agent and then degassed in a vacuum for 20 minutes. The material is poured over the sections which were removed in step 2, with an unbroken layer of adhesive tape applied to the back of the piece to discourage the material from flowing out of the desired areas. Tape can also be used to mask areas of cut geometry where the joint material is not desired. After the material is poured, it is again degassed in a vacuum chamber. About 10 minutes is required for Sylgard 184 PDMS hinges. More material may then need to be added and degassed, until all desired sections are filled and free of air bubbles (Figure 2.3d).

The fourth step is the curing of the joint material. This may be done in air, possibly facilitated by heat, or by the application of UV light, depending on the refill material. For small joints such as those fabricated in this work, this curing time is generally 1 hour or less (Figure 2.3e). For 184 PDMS joints of a few mm thickness, joints were cured at 100 °C for 1 hour.

The fifth step is the planarization of the mechanism. Extra elastomeric material will likely remain on the surface of the part, as planarization before curing can result in reintroduction of air bubbles or slightly inadequate volumes of material inside a joint due to settling during curing. A wide razor blade can be used to wipe or cut away the extra material on the surface outside of the joints, resulting in a joint with edges flush to the face of the surrounding material (Figure 2.3f).

The sixth and final step is the removal of the complete mechanism from the

surrounding base material (Figure 2.3g). Care must be taken at this step to avoid breaking the joints by applying excessive torque, as well as to avoid delamination from the links while fully releasing from the non-structural rigid material. This step must be done carefully, with as uniform pressure as possible on all areas of the mechanism to be removed. After this step, the final product is a pre-assembled compliant mechanism which can then be used independently or as a part of a larger mechanism, such as in a leg for a hexapedal robot (Figure 2.4).

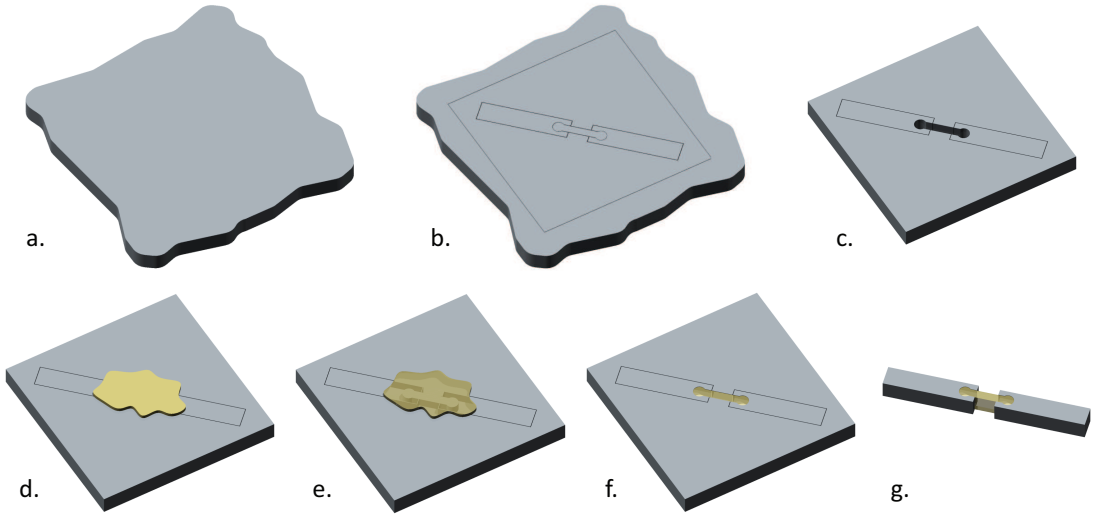

Figure 2.3: Process sequence for LaCER. (a) Rigid polymer sheet. (b) Laser cut design. (c) Remove hinge areas. (d) Pour hinge material. (e) Cure hinge material. (f) Planarize surface. (g) Release mechanim.

2.1.2 Characterization

The main advantage of this process is that it is very versatile. In theory, any material that can be laser cut can be used as the link material, and any material that can be flowed and cured can be used as the joint material (as in Figure 2.1). The size

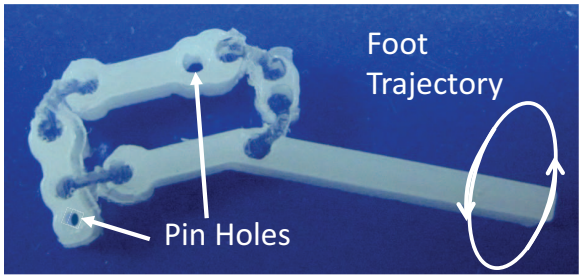

Figure 2.4: LaCER fabricated mechanism.

of the mechanism should be limited in either direction only by the resolution of the laser and the size of the cutting area.

In practice there are some factors that must be considered for this process. These include adhesion, fatigue, and aspect ratio. These should be characterized and understood in order to create a functional mechanism.

2.1.2.1 Adhesion

The adhesion between the two materials must be high enough that the joints will not easily peel away from the rigid links when put in tension or slip out when stressed laterally. However, since the same material that composes the links is also used as a mold to define the thickness of the joint, the materials must not adhere so well to one another that the mechanism cannot be removed as described in the final step in Section 2.1.1. Adhesion testing was carried out between two rigid materials; Delrin and acrylic; and two elastomeric materials; Sylgard 184 PDMS, and Insulcast MRTV-9.

To test the adhesion, samples of Delrin and Acrylic were fabricated with sections

of PDMS and MRTV protruding into them. The interfaces were fabricated with and without geometry to promote adhesion (Figure 2.5, right). The samples were then clamped in place and attached to a hanging platform from the end of the PDMS and MRTV sections (Figure 2.5, left). The hanging platform was attached by simply feeding a wire through the circle at the end of the sample. Mass was added incrementally, using small magnets to attach each increment, until the samples delaminated, and recorded the mass to failure, which was then converted to the force to failure. Table 2.1 summarizes the results of these tests. In all tests, the refill material delaminated from the interface before tearing.

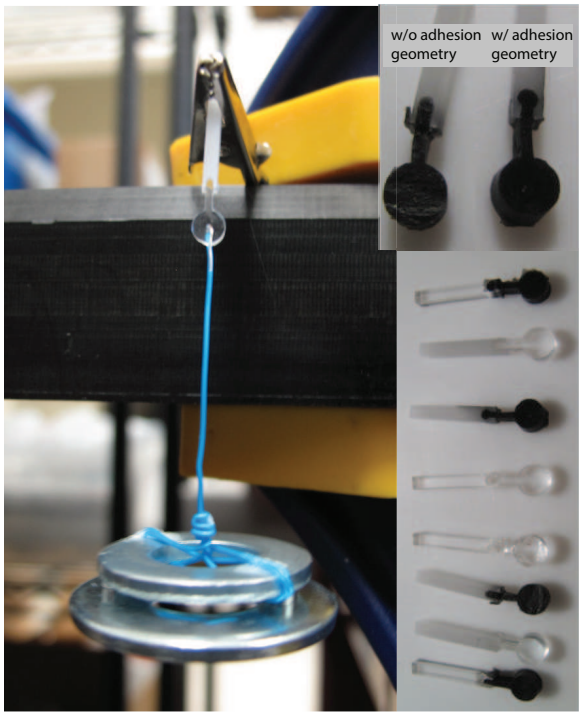

Figure 2.5: (Left) Adhesion test set up. (Right) Adhesion test samples.

Based on this data, PDMS appears to adhere better than MRTV to both Del-

Table 2.1: Tensile force to delamination for three trials of each sample type tested

Rigid Material	Elastomeric Material	Adhesion Geometry	Force to Delamination (mN) Trial 1	Trial 2	Trial 3
Delrin	PDMS	None	450	290	470
		Bulb	710	790	770
Delrin	MRTV	None	260	250	250
		Bulb	510	560	450
Acrylic	PDMS	None	160	100	70
		Bulb	740	760	660
Acrylic	MRTV	None	70	70	70
		Bulb	170	100	220

rin and Acrylic. The bulb geometry also greatly increases adhesion for each set of materials. PDMS adheres better to Delrin than Acrylic when no adhesion geometry is present, though it adheres equally well to both when the bulb is added. MRTV adheres much better to Delrin than Acrylic with either geometry.

2.1.2.2 Fatigue

Fatigue can be a large problem for compliant joints, as the material is continuously deforming during use. Some materials may be useful for mechanisms with small ranges of motion, but will fatigue quickly when subjected to large ranges of motion. Others may have lifetimes reasonable for prototyped mechanisms, but will eventually fail with prolonged use. Other materials seem to have near infinite lifetime and will not fail unless subjected to very high tensile loading. Preliminary fatigue testing has been performed on three different elastomeric materials–PDMS and MRTV, as well

as a UV curable elastomer, Loctite 3108.

To test fatigue, a simple four-bar crank-rocker mechanism was fabricated, where the rocker joint has been replaced by a compliant joint, and the crank is actuated using a 3-mm brushless gearmotor from Micromo Electronics, Inc. (Figure 2.6). The number of cycles per second was determined by counting the frames for one revolution in a high speed video. The samples were then left running for one hour (with the exception of one sample of Loctite 3108, which was left running for 6 hours), and recorded the number of cycles. Table 2.2 summarizes the results of these tests.

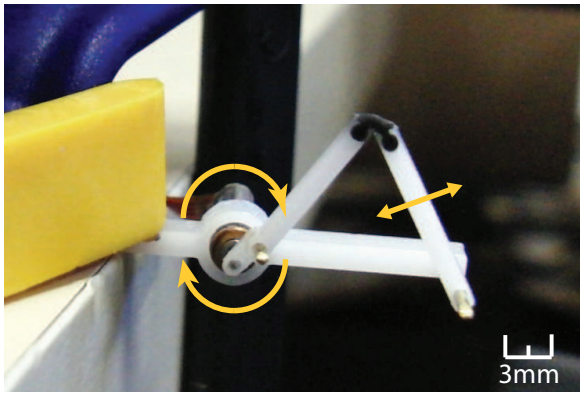

Figure 2.6: Fatigue test set up, with an MRTV joint sample.

While none of these devices failed over the course of the fatigue tests, additional testing in robot mechanisms has shown that the Loctite 3108 material fatigues more easily than others. Sylgard 184 PDMS mechanisms on the other hand, have lasted over 5 months with no sign of early fatigue. For a meso-scale walking robot with a step size of 1 cm per cycle, 30,000 cycles corresponds to 300 m of walking with no signs of failure, while 200,000 cycles corresponds to 2 km of walking without failure.

Table 2.2: Results of testing for fatigue during one hour. The 0.35-mm sample of Loctite 3108 was tested for 6 hours.

Elastomeric Material	Joint Width (mm)	# of cycles	Material Failure
Sylgard 184 PDMS	0.35	30,000	No
Sylgard 184 PDMS	0.40	30,000	No
MRTV	0.35	30,000	No
MRTV	0.40	30,000	No
Loctite 3108	0.35	200,000	No
Loctite 3108	0.40	30,000	No

2.1.2.3 Aspect Ratio

For this process it is necessary to know both the maximum trench aspect ratio–the depth of the material over minimum trench width–and the maximum line feature aspect ratio–the depth of the material over the minimum line feature width. These will determine the size of the mechanism that can be made, and will be, in part, determined by the choice of materials.

The width of the laser cut will define the maximum trench aspect ratio. For instance, when cutting Delrin using a VersaLASER VLS3.60 cutter with a 60 watt laser, the width of the cut line was found to be about 100 μm for a 1.6 mm-thick sheet, and about 200 μm for a 3.2 mm-thick sheet, resulting in a 16:1 aspect ratio.

Note that the refilled features based on these cut trenches also must take the refill material into account. For low modulus refill materials, a joint molded from a very high aspect ratio trench may be too compliant for typical use. A refill material

which is very viscous may also require a lower aspect ratio trench. Thus the practical refilled feature aspect ratio may be limited by the material rather than the base material's trench aspect ratio.

The minimum base material feature size will also be defined by the behavior of the laser cutter. It was found that for Delrin, the minimum line feature size is the same as the cut line width–about 100 μm for a 1.6 mm-thick sheet, and about 200 μm for a 3.2 mm-thick sheet. However, the strength of this material is not high enough for these features to function structurally. The practical minimum feature size is about 200 μm larger than the absolute minimum size for both material thicknesses, resulting in an aspect ratio of 8:1 or lower, for the material thicknesses used in this paper.

It is also worth noting here that when using low-modulus materials such as elastomers as compliant hinges, out of plane movement can be a significant concern. A high aspect ratio will limit the amount of out of plane motion that the mechanism will experience, relative to its in-plane motion, and keep mechanism performance in line with in-plane assumptions that may be made when modeling its behavior. This issue, along with each of the practical considerations and characterizations discussed here, should be kept in mind while designing mechanisms using this process.

2.1.3 Use as a prototyping process

The 2D nature of the LaCER process means that it is well suited for prototyping 2D MEMS mechanisms. Elastomeric MEMS mechanisms, such as those fabricated using the processes described in [23] and [19], in particular can be prototyped using this process, due to the possible integration of elastomeric materials into more rigid polymers, which approximates the rigidity of silicon in the MEMS process. Permanent magnets can also be embedded in the polymer links to prototype mechanisms designed for the process described in the following section.

2.2 Embedded Magnet Polymer MEMS

The majority of the material in this section has been taken from "Magnetic Actuation of Ultra-compliant Micro Robotic Mechanisms" [39] and "Magnetic actuation of thick film multi-material compliant mechanisms" [40].

The goal of this process is to allow the fabrication of actuated microrobotic mechanisms with a high degree of adaptability and robustness. To create these kinds of mechanisms, elastomeric materials are embedded within silicon through a micro molding process based on [23] and [19]. To actuate the mechanisms, commercially purchased permanent magnets are press-fit into the microfabricated mechanisms through a method described below. The approach to actuation of embedded magnetic components requires an externally provided magnetic field and is therefore applicable to

mobile microrobotics as a simple way of investigating motion and force requirements in a potential mechanism design without the need for other integrated actuators or onboard power sources. It is also suitable for applications such as the development of micro-surgical tools, micro pick-and-place manufacturing, or other applications where the mechanism stays relatively stationary and the power source cannot be or does not need to be on board.

2.2.1 Process

The process (seen graphically in Figure 2.7) starts with a 300 μm thick double-side-polished (DSP) silicon device wafer with an 8 μm backside oxide layer. A 15 μm layer of SPR 220-7 photoresist is spun on the front side, baked for 15 min at 90 °C, and allowed to re-hydrate overnight. The wafer is then photo-patterned with a 35 s exposure, developed for 1.5 min in MF-CD-26 developer, and hard baked for 60 s at 90 °C. The device wafer is then bonded to a 500 μm thick silicon handle wafer by spinning a thick layer of SPR 220-7 onto the handle wafer, placing the device wafer in contact, and baking the bonded wafers at 90 °C for 2 hours (Figure 2.7 a).

A deep reactive ion etch (DRIE) is then performed through the thickness of the device wafer to form molds for the elastomer features, including the compliant joints and sleeve features for embedding the small magnets in the mechanisms (Figure 2.7 b). At this point, the device wafer is temporarily removed from the handle wafer via an acetone soak. This leaves the device wafer quite fragile, so care must be taken in

subsequent steps to avoid shattering. Uncured elastomeric material, in this case Dow Corning Sylgard 184 PDMS, is deposited over the full surface of the device wafer. The wafer is placed in a vacuum chamber at 1 Torr for 15 min to degas the uncured PDMS. The wafer is placed on a hotplate at 90 °C for 15 min to cure the polymer. Finally, a razor blade is used to slice away the PDMS remaining on the surface of the wafer, planarizing the material and leaving only the embedded PDMS features (Figure 2.7 c). This is followed by a brief 60 s soak in a solution of 3:1 TBAF-NMP to remove any remaining polymer particles.

A second lithography step is performed using a mask to define the silicon features and the handle wafer is reattached. A second DRIE through the thickness of the device wafer forms the structural mechanism features (Figure 2.7 d). Finally the handle wafer is removed with an acetone soak and the magnets are press-fit into elastomer sleeves (Figures 2.7 e,2.7 f). The magnets used were 500 μm x 500 μm x 200 μm powder-pressed N50 neodymium magnets, available from SuperMagnetMan (http://www.supermagnetman.com S0050). The task of assembling these micro magnets into the elastomer sleeves is discussed in more detail in the following section.

2.2.2 Assembly

Assembly of the magnetic portions of the mechanisms can be done entirely by hand with a pair of fine-tipped tweezers. However, because the devices and magnets are very small, manual orientation and assembly of each magnet is quite difficult,

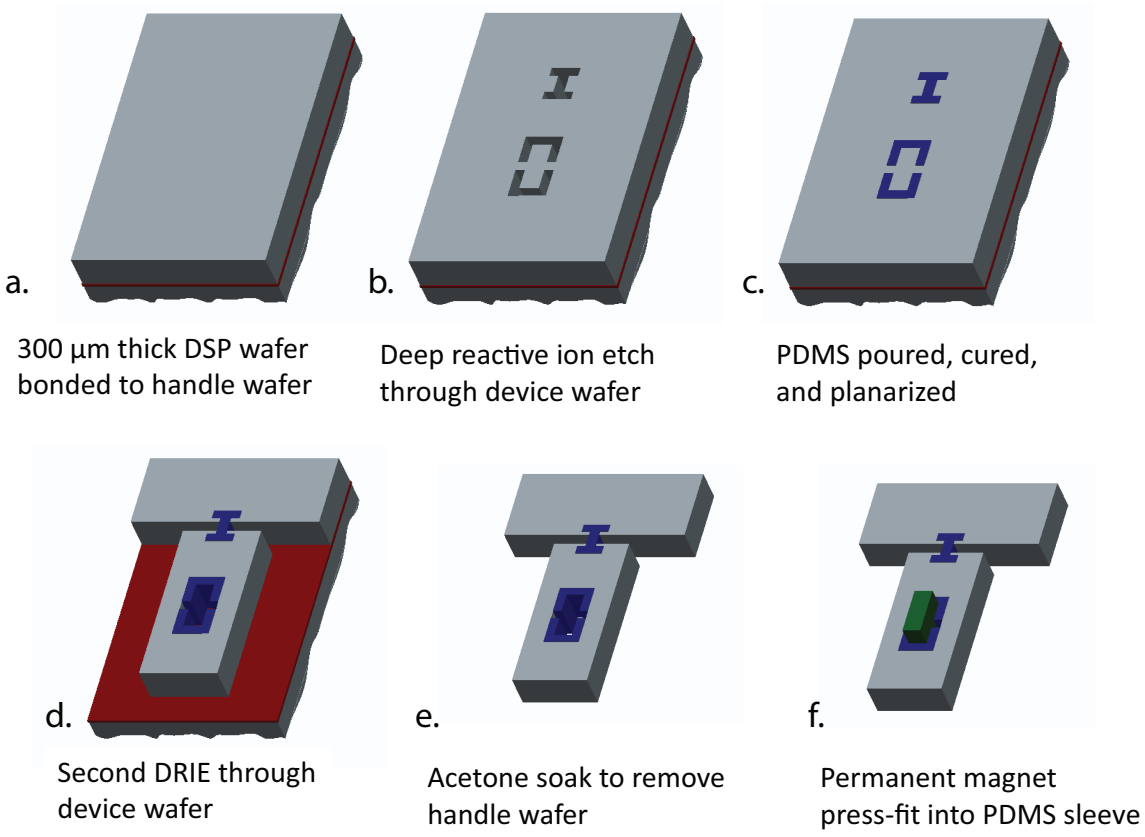

Figure 2.7: Embedded magnet elastomer MEMS fabrication process.

even with the aid of tweezers and a microscope. This difficulty is compounded by the symmetry of the magnets (because the poling direction is important for achieving the desired function from a mechanism, and this aspect of the magnets usually cannot be determined directly by sight). The magnets sometimes also "jump" away to other, already-assembled magnets nearby on the die if they are inadvertently released at any point during the process, and they can be difficult to remove without pulling out the already assembled magnet.

To assuage these difficulties, a solution was implemented in the form of a pre-

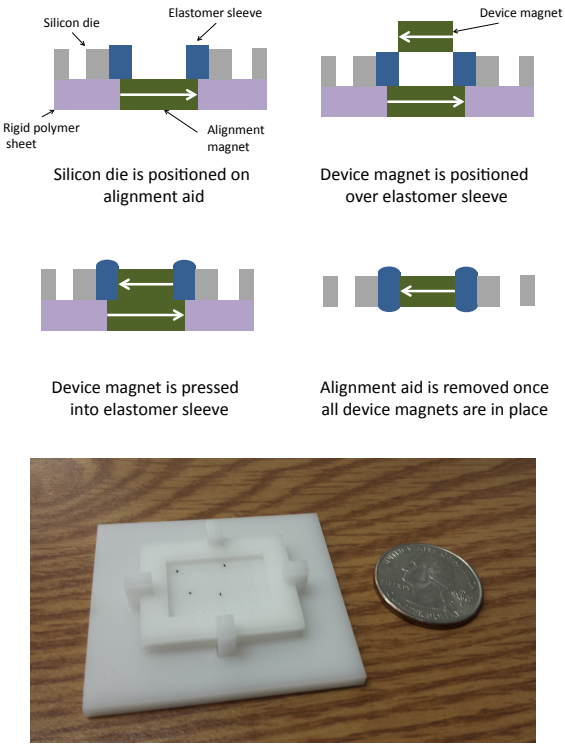

Figure 2.8: Device magnet assembly. Above: assembly process. Below: Assembly aid. Alignment magnets appear as small black dots.

assembled magnet alignment aid (Figure 2.8). This consists of a small strip of thin polymer sheeting, about the size of a single die of devices. The small sheet is laser patterned with trenches corresponding to the locations of the magnet sleeves on the unassembled die. The sheet is then populated with magnets in the proper orientation to encourage the final device-magnet desired orientations (see Figure 2.8). These magnets are then glued into place individually or a sheet of thin laminate can be applied over the surface to keep the entire assembly in place.

Once the assembly aid is completed, the die is aligned with the sleeves above the assembled magnets and placed on the surface. A thin frame can be used to keep

the die in place if it does not inhibit the assembly of the magnets. Otherwise a very small spot of double-sided scotch tape under one corner of the die was found to work fairly well. With the die kept in place above the pre-assembled magnets, device magnets can simply be placed above each of the sleeves and will automatically align and remain in position without requiring continuous gripping with tweezers, allowing for a single placement step for each magnet, and a simple push to press-fit it into the sleeve.

This method still requires a single assembly step where careful attention must be paid to the orientation of the magnets as they are put in place, but a single pre-assembled alignment aid can be used for any number of identical dice and greatly reduces the difficulty of assembly for each.

2.2.3 Characterization

Some initial testing and analysis has been done to characterize the fit of the embedded magnets. Because the magnets are not glued in place, but press-fit into elastomer sleeves, they can be pulled out by an external magnetic field of sufficient strength, oriented in the proper direction. Magnets were fit into sleeves of different dimensions, as described by Figure 2.9, with dimension A between 0 and 35 μm, and dimension B between 65 and 85 μm. The large external magnet was slowly moved toward the sleeve with the field oriented along the direction of the magnet's poling to attempt to pull the magnet out of the sleeve. The distance between the chip and the

external magnet at the point when the embedded magnet pulled out was recorded.

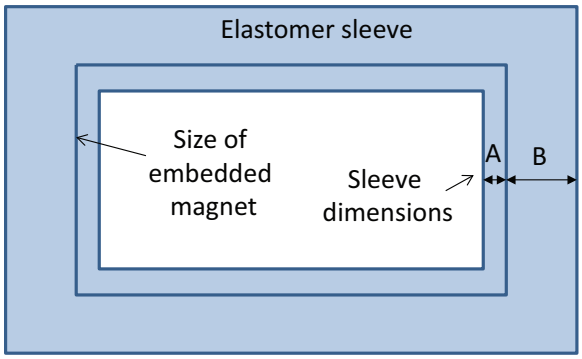

Figure 2.9: Varied elastomer sleeve dimensions. The dashed box is the size of the embedded magnet, 200 μm x 500 μm

The external magnet was within a centimeter of the chip at the point of pull-out for the seven sleeves tested. These are preliminary results, however, and an optimal sleeve size has not been determined. For the mechanisms fabricated, the sleeves used were varied between A = 0 μm, A = 12 μm, and A = 25 μm, with B = 75 μm in all cases. Additionally, because the magnetic field is not usually oriented to pull the magnet out, and the proximity of the large magnet is not usually so close, the embedded magnets have not been observed pulling out of the mechanisms during normal use.

Chapter 3

Elastomeric Hinge Modeling

The majority of the text in the following chapter is taken from "Characterization and Modeling of Elastomeric Joints in Miniature Compliant Mechanisms" [41].

Both of the fabrication processes described in the previous chapter will result in multi-material mechanisms with small elastomeric hinges. Much previous investigation has been done in the area of multi-material mechanism design and modeling, such as those fabricated using multi-material molding (MMM) [42], where flexible and rigid materials are molded together to produce mechanisms with rigid links connected by compliant joints. This work builds upon this previous investigation, however the hinges presented here, fabricated using LaCER and the Si-elastomer microfabrication process, are capable of exhibiting large deflections and can also include significant axial stretching during actuation of the mechanisms, for instance during the gait cycle of a robot with compliant legs, particularly if the robot is carrying a heavy payload. Compliant mechanism modeling is important for predictable behavior and for accurate investigation into the design of compliant legs . Modeling of miniature compliant mechanisms is currently done using methods such as the PRB method, which replaces the compliant hinge with a pin joint and torsion spring [25]. This approach works well for small angular deflections and when axial lengthening is not significant. More

complex versions include using several pin joint/torsion springs along the length of the beam for large-tip-deflection [43], and using two torsion springs and an axial spring for modeling carbon nanotubes as well as tensural pivots in micro scale multistable mechanisms [44, 45]. Further modeling methods include FEA, which has been used to model and design single-material compliant mechanisms [24]. FEA tends to be highly accurate, but time-consuming and computationally expensive compared to the PRB method.

This chapter presents the development of a a 3-spring PRB analytical model for small compliant hinges. First, section 3.1 describes Finite Element Modeling of experimental characterization data taken on miniature compliant hinges. Second, section 3.2 describes the 3-spring PRB model. This model includes both bending and axial deformation possible in elastomeric hinges and compensates for anchoring geometry required in multi-material compliant mechanisms and some other geometries as well. The model is verified against the FEA model developed in section 3.1. Finally, in section 3.3 this 3-spring model is evaluated against PRB models with various numbers of springs from 1 to 19, and the 3-spring model is found to be a good combination of accuracy and simplicity for elastomeric joints.

3.1 Finite Element Analysis for Characterization of Compliant Hinges

In the development of a simplified model for this prototyping process, the first step was to take experimental data regarding the behavior of the elastomeric hinges

Table 3.1: Summary of the hinge geometry of each sample type

Type #	Angle (°)	Hinge Shape	Centerline length (mm)
1	180	–	1.0
2	90	Arc	1.6
3	90	Trapezoid	1.4
4	135	Arc	1.9
5	135	Trapezoid	1.8

in bending and in tension. The data collected during this step serves as a baseline for verification of the accuracy of the FEA models for these hinges. Once the FEA models are determined to be accurate, they can in turn be used as a baseline for verification of the accuracy of the PRB models.

3.1.1 Experimental Setup

First, samples of five different hinge geometries were fabricated using the LaCER prototyping process, as described in Chapter 2, Section 2.1. These samples consisted of two rigid Delrin links (9 mm x 2 mm x 1.6 mm), with one Sylgard 184 PDMS hinge, 1.6 mm thick and 0.6 mm wide, shaped differently for each hinge type. Figure 3.1 shows a schematic and photograph of each geometry type, and the hinge geometries are summarized in Table 3.1.

The hinge shape referred to in Table 3.1 differentiates the curved or straight line paths between links for joint types with initial angles $< 180°$. The curved or straight line paths form an arced or trapezoidal front-face geometry, respectively (See the

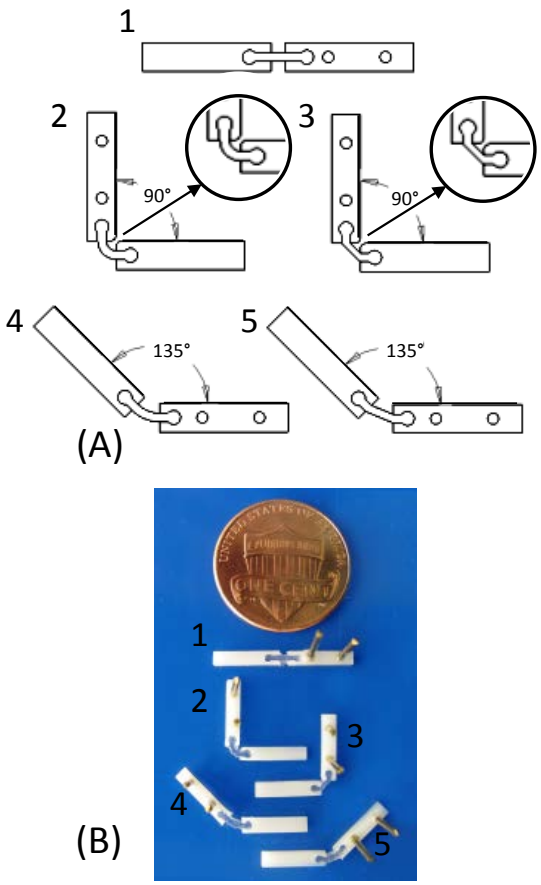

Figure 3.1: Schematic and photograph of five different hinge geometries. Geometry type 1 is 180°, type 2 is 90° with an arced hinge shape, type 3 is 90° with a trapezoidal hinge shape, type 4 is 135° with a arced hinge shape, and type 5 is 135° with a trapezoidal hinge shape.

insets in Figure 3.1). Samples of each were fabricated to investigate the behavioral differences between the two choices. The three different inner angles of the five geometries were chosen as being representative of the range of initial angles likely to be used in a miniature robotic mechanism. Any arbitrary hinge shape possible could additionally be investigated using the same procedure detailed in this paper for its characterization and modeling. Only one combination of materials was chosen for

these samples (Delrin and PDMS), but many other combinations are also possible [46].

3.1.1.1 Bending

To test the bending behavior of the fabricated samples, a test setup was laser cut out of Delrin, with an acrylic stand for positioning and photographing (Figure 3.2). The test setup consisted of a base on which to attach the sample and a lever arm with which to apply a force to the sample. The base was cut with an array of holes which allowed the samples to be attached at various orientations, and allowed the lever arm to be moved into position for use with different geometry types. The lever arm was designed to have weights suspended from one end, while the other, circular end pushes up on the sample to bend it. This type of circular head allows for a nearly pure bending regime for the first set of tests.

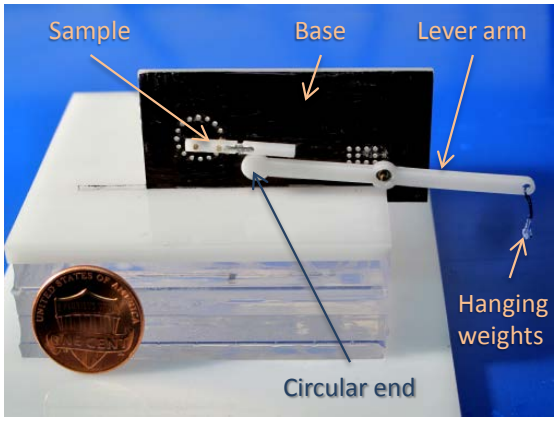

Figure 3.2: Bending test setup

The force on the sample is dependent on both the applied weight on the lever

arm and the current angle of the sample arm. Because the angle of the sample arm is dependent on the angle of the lever arm, a kinematic relationship between the two arms was determined. The first step was to define the parameters to be used in this relationship (Figure 3.3).

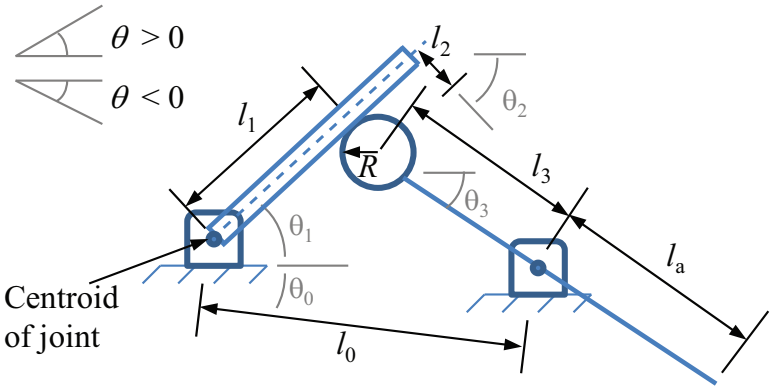

Figure 3.3: Test setup mechanism schematic

In Figure 3.3, the distance from the centroid of the compliant joint to the pivot point of the lever arm is denoted by l_0. The variable distance from the joint centroid to the point on the sample arm where the force is applied is denoted by l_1. The normal distance from the line originating at the joint centroid and extending along sample arm, to the center of the lever arm's circular end is denoted by l_2. The distance from the center of the lever arm's circular end to its pivot point is denoted by l_3. Considering each of these lengths as rigid-body links, θ_0 through θ_3 are the angles of these links with respect to horizontal. θ_2 can additionally be defined as equal to $90° - \theta_1$, as link 2 is always normal to link 1. Angles below the horizontal are measured as negative angles. Given θ_0, θ_1, l_0, l_2, and l_3 as known inputs, the outputs – θ_3 and l_1 – can be determined using the following equations:

$$l_1 = \frac{-A - \sqrt{A^2 - 4B}}{2} \tag{3.1}$$

$$A = -2l_0 \cos(\theta_0 - \theta_1) \tag{3.2}$$

$$B = l_0^2 + l_2^2 - l_3^2 - 2l_0 l_2 \sin(\theta_0 - \theta_1) \tag{3.3}$$

$$\theta_3 = \arctan\left(\frac{l_0 \sin\theta_0 - l_1 \sin\theta_1 - l_2 \sin\theta_2}{l_0 \cos\theta_0 - l_1 \cos\theta_1 - l_2 \cos\theta_2}\right) \tag{3.4}$$

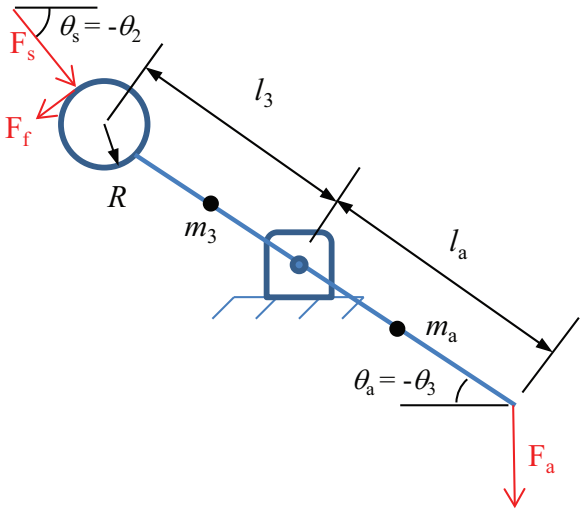

Figure 3.4: Free body diagram of test setup lever arm

After deriving a kinematic relationship between the sample and lever arms, θ_2 and θ_3 were used as inputs to a free body diagram of the lever arm, to calculate the force acting on the sample arm at each applied load (Figure 3.4). Here, the input angles have been defined as $\theta_s = -\theta_2$ and $\theta_a = -\theta_3$.

The forces acting on the lever arm from the sample are determined using the following equations:

$$F_s = \frac{F_a l_a \cos\theta_a + g\cos\theta_a(m_a l_{ma} - m_3 l_{m3})}{l_3 \sin(\theta_s - \theta_a) + \mu(l_3 \cos(\theta_s - \theta_a) + R)} \tag{3.5}$$

$$F_f = \mu F_s \tag{3.6}$$

F_a is the force applied to the end of the lever arm, l_a is the distance from the central pivot to the end of the lever arm where F_a is applied, g is gravity, m_3 and m_a are the masses of each side of the lever arm, l_{m3} and l_{ma} are the distances from the central pivot to the centers of mass on each side of the lever arm, and R is the radius of the circular end of the lever arm. The coefficient of friction between the lever arm and the sample arm is designated as μ. This has been estimated to be $\mu = 0.6$ for this material and fabrication process, based on a best fit between Ansys^{TM} results and experimental results. The somewhat high coefficient of friction for Delrin on Delrin can be explained by ridging on the edges of the pieces due to the pulsing of the laser during cutting.

F_a was increased incrementally, using small magnetic weights (approximately 0.35 mg each), from 0 mN to a point where the combined reaction forces, F_s and F_f, can no longer overcome the moment induced by F_a, and the lever arm slips from the sample. This maximum load is not the same for each geometry type. For types 1, 2, and 3, the maximum applied force before slipping was 5.45 mN. For types 4 and 5, the maximum was 3.0 mN. The difference in these results is in part due to the initial angle (θ_3) of the lever arm, which was different for each joint geometry because of the

configuration of the test setup. Therefore, the magnitude and position of the force applied to the sample varies, despite the same force being applied to the other end of the lever arm.

3.1.1.2 Tension

The second set of tests investigated the pure tension behavior of samples of geometry type 1. The same test setup shown in Figure 3.2 was used. Samples of geometry type 1 were oriented vertically by mounting the sample's two pins in the appropriate holes along the circular array (on the left, in the figure), with the free link oriented downward. A single magnet was glued to the end of the free link, and further magnets were added to the first, resulting in applied forces from 0 (before the glued magnet) to 420 mN.

3.1.1.3 Analysis

During each test, the position of the sample was photographed using a Casio EX-F1 camera, with a resolution of 2304 x 1728, leading to a resolvable displacement of about 50 μm, based on calibration measurements made using Tucsen's TSView software. For the bending tests, TSView was used to analyze the photographs and find the inner angle of a sample with each incremental change in the applied weight. For each sample, the range of steadily-decreasing inner angles was recorded until the lever arm slipped. This was done for a representative sample of each geometry

type, as well as ten samples of type 1. The smallest change in inner angle of the representative samples occurred in the sample for geometry type 1, with a change in the inner angle, $\Delta\theta$, of 15°, while the largest change in angle occurred in type 2, with a $\Delta\theta$ of 38°. However, the $\Delta\theta$ should not be compared across joint types because of the differing manner in which each was mounted on the test setup. These tests are for verification of the FEA model, rather than comparison between geometries. For the tension tests, the length of the elastomeric joint was measured using TSview. The maximum change in length of the representative sample was 0.78 mm equating to a joint strain of 68.4%.

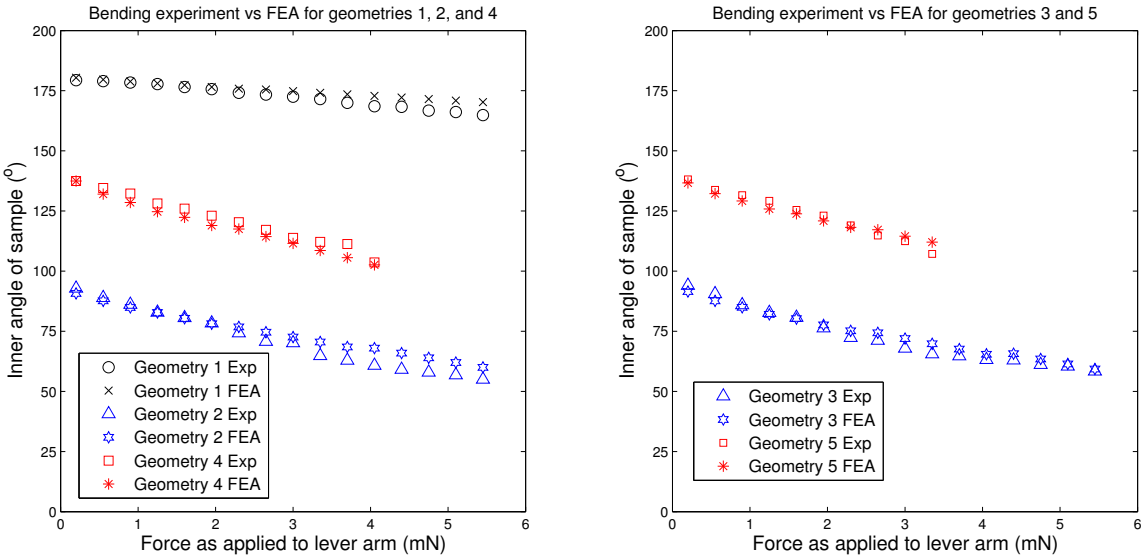

Figure 3.5: A comparison of experimental and FEA results under pure bending load for geometries 1, 2, and 4 (left), and geometries 3 and 5 (right)

The LaCER process is a prototyping process that can result in differences between individual samples due to variable PDMS modulus (mixing and curing), extra PDMS leftover after the curing step in Figure 2.3 c, and variable dimensions from

laser cutting. To characterize these variations, ten samples of joint type 1 – each fabricated using the same CAD file – were compared against one another using the same testing procedure described above. There was significant–up to about 200%– variation in deflection across the ten samples. However, this does not invalidate the models discussed in this paper. It simply means that when modeling hinges made using LaCER, the hinges must be carefully inspected and measured, rather than relying on the intended dimensions and material properties. This may lead to lower accuracy when fabricating mechanisms based on the models discussed here, though careful preparation of materials will improve the results. Additionally, more repeatable prototyping methods such as SCM and SDM, and future, more automated, iterations of the LaCER prototyping process will produce much more predictable results in the fabricated mechanisms.

3.1.2 Finite Element Modeling

Ansys^{TM} was used to perform finite element simulations of the different geometry types. Dimensions for the FEA model were determined by taking measurements from a sample of each geometry type. While experimental results were collected for multiple samples of each geometry type, the slight geometric differences between each fabricated joint would require a separate FEA model of each joint for a fair comparison. So, only a single experimental result is compared to the FEA results for each geometry type. The material models used were a linear elastic model for the Delrin

links and a nonlinear Arruda-Boyce curve-fit model for the PDMS hinges [47]. The Young's modulus used for Delrin was 1.5 GPa, with a Poisson's ratio of 0.4. A TA Instruments Q800 Dynamic Mechanical Analyzer (DMA) was used to obtain stress-strain data in samples from the same batch of the Sylgard 184 PDMS used for the joints, which was then fit to the model using the Ansys^{TM} 13.0 curve fit function. The material constants – initial shear modulus, μ_0, and limiting network stretch, N – were determined to be $\mu_0 = 260.66\ mN/mm^2$ and $N = 1.27$. It is important to prepare the elastomer using the same mixture ratio, curing time, and curing temperature to ensure that these properties will be valid for future mechanisms fabricated after modeling.

Ansys^{TM} 3D SOLID185 brick elements were used for both the links and hinges, due to their ability to handle hyperelastic materials. 2D SURF184 elements were fixed to the surface of some elements on the links at the force application point. These elements allow the force to be applied both normally and tangentially, as required for this application.

The surface-to-surface contact forces between the sample and the lever arm were explicitly defined, rather than using Ansys's surface contact model between models of the two. A single normal force and a single tangential frictional force were ultimately used, derived using Eqns. 3.1 - 3.6.

The load calculated using these equations was applied to the sample arm in Ansys^{TM}, length l_1 (Eqn. 3.1) away from the joint centroid. F_s (Eqn. 3.5) was

oriented orthogonal to the surface and F_f (Eqn. 3.6) parallel to the surface. The starting setup defines the initial value of $\theta_1 = 0$. Each incremental simulation produces a new θ_1 as an output, which is then used to find the force to be applied on the following simulation. This method introduces some error in the model, as it uses the previous step's final angle to determine the current step's applied load. This error was found to be insignificant, but it could be further reduced by breaking each step of the simulation into smaller substeps, with new applied loads calculated between each substep.

Figure 3.5 shows the results of the FEA simulations and the experimental data for the five joint geometries in Figure 3.1. The experimental results match up with Ansys^{TM} results fairly well, within an error of 9%, for all of the comparisons performed. The primary source of this error is likely due to non-uniform cross sections in the joint due to laser cutting or excess PDMS flashing after the joint is fabricated, as discussed in Section 3.1.1.3. The maximum 9% error was seen in joint type 2, which also went through the largest deflection ($\Delta\theta = 38°$). The error between experimental and Ansys^{TM} simulations tends to increase over higher bending angles, but the error is within 5% up to a $\Delta\theta$ of 15° for all geometry types, and up to 35° for types 3, 4, and 5. If larger bending angles are anticipated in a mechanism design, larger errors in the final fabricated mechanism can be expected.

Tension testing was also modeled in Ansys^{TM}, with a single force applied to one end of the first hinge type, along the axial direction, with gravity oriented in the

same direction. This simulation was carried out assuming that the elastomer joint will delaminate up until the point of the circular geometry embedded in the link, so these areas are not mechanically connected in the model. This is in agreement with the apparent behavior of the hinge in high-tension applications, determined by examining photographs taken during experimental testing. This effect is not important in pure bending, because the effective length of the elastomeric joint is still determined by the ends of the rigid links, and delamination is not typically seen under bending loads. The simulation results for the tension tests are accurate to within 4% error (Figure 3.6).

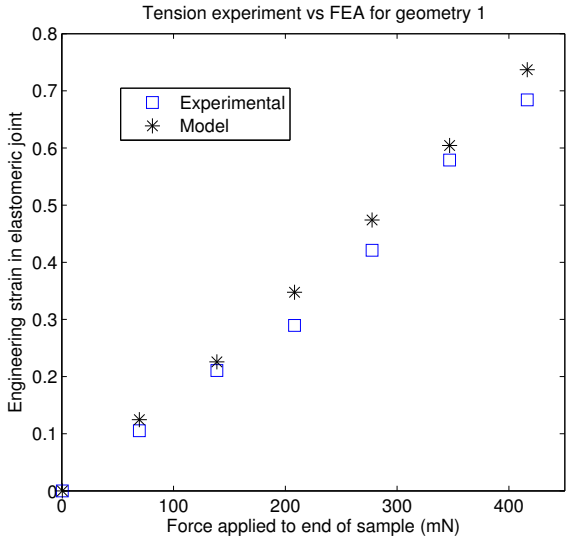

Figure 3.6: A comparison of experimental and FEA results under pure tension load

3.2 Pseudo Rigid Body Modeling of Miniature Compliant Joints in Bending and Tension

The FEA and experimental results above showed that FEA can be used to accurately model elastomeric joints fabricated using LaCER. The next step was to develop a less computationally expensive modeling method to evaluate single joints and eventually entire mechanisms. This model has been developed in the form of a 3-spring PRB model.

The pseudo-rigid body method is usually carried out using a single torsional spring, here called the 1-spring PRB model. This is intended to model a short compliant joint – where the length of the joint, l, is much less than the length of the rigid link, L, and there is insignificant stretching of the joint – as a pin joint with a superimposed torsional spring of spring constant $k_{\theta 1spr}$,

$$k_{\theta 1spr} = \frac{EI}{l} \tag{3.7}$$

where E is the elastic modulus of the joint material, and I is the cross-sectional moment of inertia of the joint [25]. Using this method, it is simple to quickly estimate how the torsional stiffness of joints with different dimensions and/or materials compare.

This PRB model, while a good approximation for the pure-bending case, does not account for stretch in the joint, or some of the more complicated behavior observed

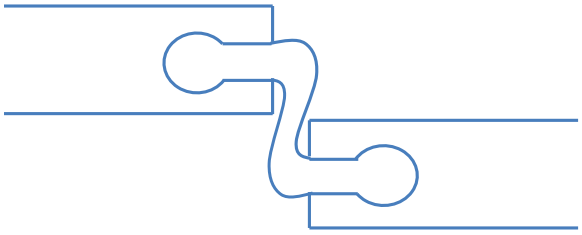

Figure 3.7: One type of observed hinge behavior that cannot be modeled using the single spring pseudo-rigid body model. This behavior can be captured by the 3-spring PRB model with a bend in each torsion spring and (optionally) a stretch in the axial spring.

Figure 3.8: Configuration of a 3-spring pseudo-rigid body model

in mechanisms fabricated in processes including LaCER. An example of this behavior can be seen in Figure 3.7. Though this behavior may not be desirable for some mechanisms, it is still desirable to capture it in the modeling of an initial design so that it can be eliminated. To more accurately capture these types of behaviors, a pseudo-rigid body model has been developed consisting of two torsional springs and a single axial spring, arranged as shown in Figure 3.8. The spring constants for this model have been determined using geometric and material parameters, according to the following equations:

$$k_{\theta 3spr} = \frac{2EI}{l_{eff}} \tag{3.8}$$

$$k_{l3spr} = \frac{CAE}{l_{eff}} \tag{3.9}$$

where $k_{\theta 3spr}$ is the torsional spring constant, E is the elastic modulus of the joint

material, I is the cross-sectional moment of inertia of the joint, l_{eff} is an effective hinge length, k_{l3spr} is the axial spring constant, C is a correction factor, and A is the cross-sectional area of the joint.

In these equations, $k_{\theta 3spr}$ is similar to the single spring PRB $k_{\theta 1spr}$, distributed across two torsion springs, with the exception that length l is replaced with l_{eff}, an effective hinge length described in Section 3.2.1. The linear spring constant k_{l3spr} depends on the cross-sectional area of the hinge and uses the equation for axial beam stiffness, again using l_{eff}. The correction factor, C, can also be included to account for reduced stiffness due to adhesion geometry. This will be discussed in more detail in Section 3.2.2. The cross-sectional area of the hinge is assumed to be constant and all geometry is based on the initial joint dimensions.

Because the actual joint is assumed to be symmetrical, the pseudo rigid joints should also be symmetrical, so the two torsional spring constants are equal (although their behavior is not necessarily symmetrical, as in Figure 3.7). Because the two springs are arranged in series, the required stiffness of each is twice the stiffness required for a single torsion spring.

Delamination of the adhesion geometry has not been considered in this model, although it is present experimentally in LaCER fabricated mechanisms. To simplify the process, it is assumed here that the mechanisms modeled are not significantly affected by delamination.

3.2.1 Compensating for Initially Bent Joints

The geometries of the initially bent joints (geometries 2-5) required special considerations for an accurate model. While the lengths of the hinges in geometries 1, 3, and 5 are 1 mm when measured down the center, geometries 2 and 4 have slightly longer hinges, due to the curve in the elastomeric joint (Figure 3.1). For the 3-spring PRB model, the axial spring is placed in a straight line between the two connected ends of the rigid links, so the PRB model looks the same for geometries 2 and 3, and for geometries 4 and 5. However, for geometries 2 and 4, the hinge length, l_{eff} used in Eqns. 3.8 and 3.9, is longer than the length of the spring due to the curve.

Additionally, geometries 3 and 5 deviate significantly from the behavior expected from the assumed rectangular beams in Eqns. 3.8 and 3.9, with geometry 3 being particularly affected due to an extreme deviation from the ideal. To preserve the simplicity of the PRB model, a simple rule was formulated to account for the effective reduction in hinge length due to the trapezoidal shape of the front face of the compliant hinge. A characteristic trapezoidal angle can be found for these hinges by taking the angle between the sloped wall of the hinge's front face and the normal to the length of the hinge (Figure 3.9). The effective length for the hinges was determined first by obtaining FEA results over normal loads from 0 to 20 mN applied 4 mm from the end of a 9 mm rigid link, for six different trapezoidal angles from 0 to 45° and two different centerline lengths. The hinge width used was 0.8 mm and the thickness was 1.6 mm. The 3-spring PRB model was then used to model these

same geometries at several effective lengths for each. The best matches (those with results that produced the lowest error when compared to the FEA results) of these were then used to find a predictive model for the effective length of a joint at a given trapezoidal angle. This effective length was found to be described well by a simple linear model:

$$l_{eff} = l_c + s\theta_{trap} \tag{3.10}$$

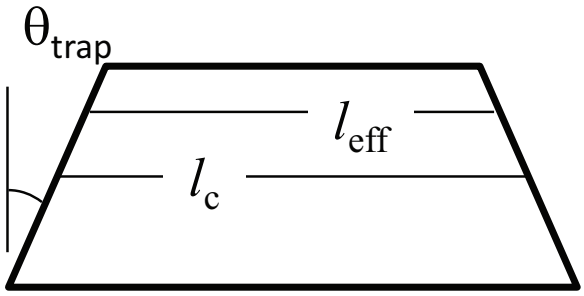

Figure 3.9: A schematic of the front face of a trapezoidal hinge, with the centerline and effective lengths shown, as well as θ_{trap}

In this equation, l_{eff} is the effective length of the hinge in mm, l_c is the centerline length of the hinge in mm, θ_{trap} is the trapezoidal angle in degrees, and s is the slope of the fit line, found equal to -0.01 mm/deg (Figure 3.10). This compensation for the corner effects in hinges with a trapezoidal front face was found to describe hinges over lengths from 1 to 2 mm with trapezoidal angles from 0° to 45°. The best match effective lengths are shown along with the lines described by Eqn. 3.10 over these ranges in Figure 3.10. It should be noted that while Eqn. 3.10 does not describe the line of best fit to match l_{eff} values with θ_{trap} values, it is a simple rule of thumb and

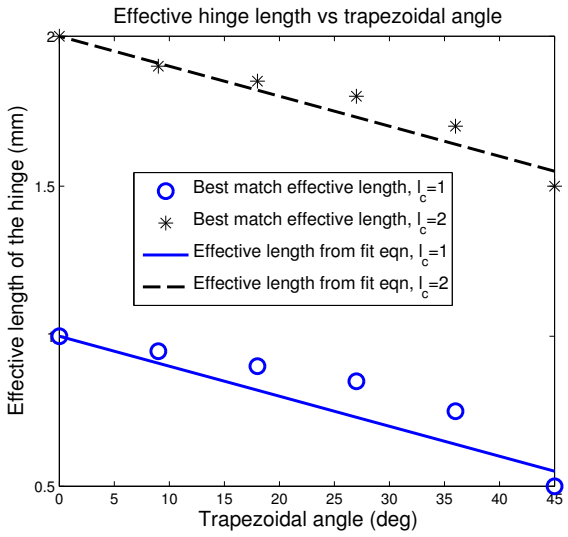

Figure 3.10: Comparison of the effective length of a rectangular compliant hinge to a trapezoidal hinge with angle θ_{trap}

a good fit over these ranges. This equation also reduces to $l_{eff} = l_c$ at $\theta_{trap} = 0$, which is realistic, as there are no corner effects in a rectangular joint to require a length correction. This also matches $l_{eff} = l_c$ used for the initially curved joints in geometries 2 and 4.

3.2.2 Compensating for Adhesion Geometry

Although delamination of the adhesion geometry is not considered in this analysis, the effect of the adhesion geometry can be considered, especially for large tensile forces. The extra material embedded into the rigid links at the ends of a compliant hinge contributes to the change in length of the hinge in tension. Additionally, if the adhesion goemetry is small and the connection between the materials is rigid, the free end-condition assumptions made in the equation for axial beam stiffness – used for

determining k_{l3spr} – are violated, and the hinge will be more rigid than predicted by the 3-spring PRB model. In order to account for these changes in behavior, several versions of joint type 1 were modeled in Ansys^{TM} with different lengths of adhesion geometry, length l_g from 0 to 0.6 mm, extending into the rigid link (Figure 3.11). The dimesions used were $l_h = 1$, $w_h = 0.8$, and $t = 1.6mm$. Each version was extended to 20 to 30% strain, using an applied force of $F = 400mN$ for each. An effective k_{FEA} was determined at this point by dividing applied force by the change in length of the hinge. A correction factor, C, was determined by dividing this k_{FEA} by the k_{PRB} determined by the beam extension equation (i.e. Eqn. 3.9, without the correction factor). C is applied only to the linear spring equation, and not the torsion spring equations. The value of C varies with the length of this adhesion geometry, with a value greater than 1 for short or no adhesion geometries, and approaches a value of about 0.8 for long adhesion geometries (Figure 3.12). These values may be different for other types of adhesion geometry or different strain ranges, in which case a similar process can be used to determine C for this new geometry.

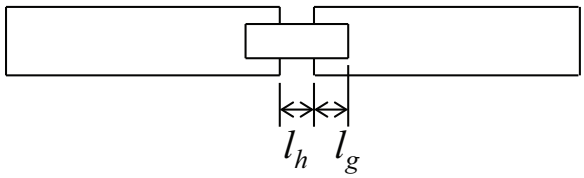

Figure 3.11: A schematic of a hinge with adhesion geometry extending into the rigid links a distance l_g. This adhesion geometry affects the stiffness of the hinge in tension.

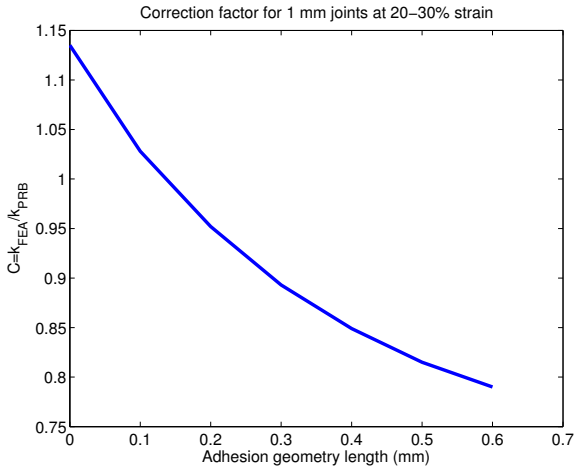

Figure 3.12: Correction factors for k_{l3spr} for a 1 mm long hinge over a range of 0 to 0.6 mm adhesion geometry. These values were taken over a strain range of 20-30%.

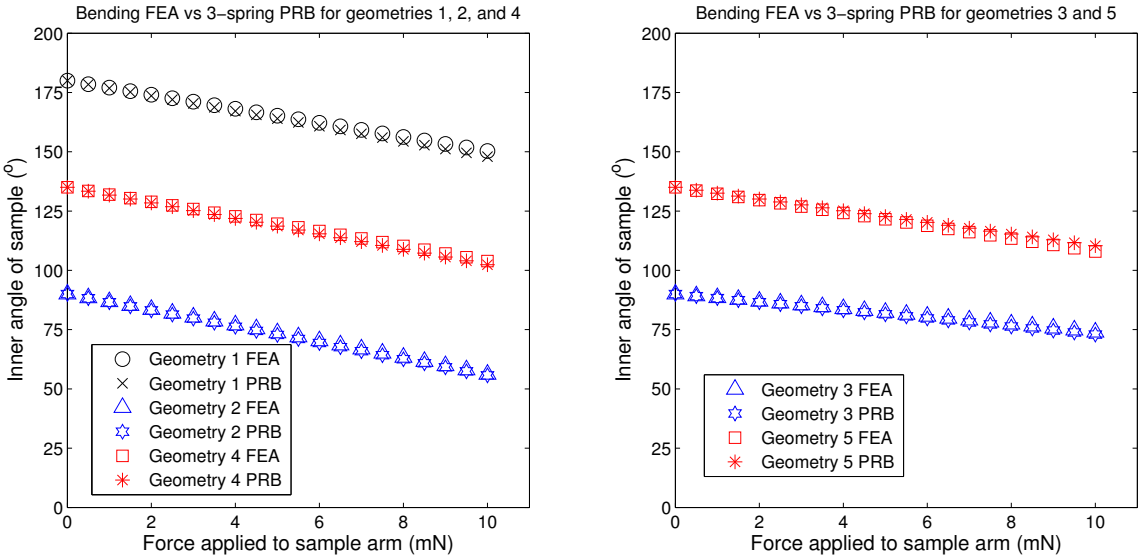

Figure 3.13: A comparison of FEA and 3-spring PRB results under pure bending load for geometries 1, 2, and 4 (left), and geometries 3 and 5 (right). The 1-spring PRB results are similar to the 3-spring model.

3.2.3 Pseudo Rigid Body Modeling Compared with FEA

To determine the accuracy of the 3-spring PRB model, five joints of the same geometry types shown in Figure 3.1 were modeled using the 1-spring and 3-spring

PRB models. These were then modeled using FEA, and the behavior of the joints in each model was compared. For these models, the geometry and loading conditions have been simplified relative to the models described in Section 3.1. Here, each rigid link is 9 mm, with the force applied 4 mm from the free end of one link, and the other link is fixed. The distance between the centers of the connected ends of the rigid links is 1 mm. A hinge width of 0.8 mm, and a material thickness of 1.6 mm were used. For bending, the forces were applied normal to the link, with no tangential component. Force was applied from 0 to 10 mN. For the tensile case, the force was applied at the free end of one rigid link, along the axial direction, with no normal component. Force was applied from 0 to 800 mN. No gravity component was applied for these cases. This is somewhat different from the previous cases because a comparison of the PRB models to experimental data is not needed here, and these conditions are simpler to analyze.

In Ansys^{TM}, the same material models were used as described in Section 3.2 – Arruda-Boyce for the PDMS, and linear elastic for the Delrin, SOLID185 brick elements were used, with element sizes of 0.1 mm in the joint and 0.4 mm in the rigid links. Because all forces in these simulations were applied normal to a plane, the surface elements previously used were not necessary.

The PRB model analyses were carried out using Matlab, with Equation 3.7 used for the 1-spring PRB model, and Eqns. 3.8 and 3.9 used for the 3-spring PRB model. The axial spring was constrained to move only in the line between the two rigid links'

ends and was given an initial length equal to the distance between the rigid links (not neccesarily equal to l_{eff}, as discussed in Sec. 3.2.1). One rigid link was constrained while force was applied to the other in increments of 0.5 mN, with the direction of the force changing after each step in bending to keep the force normal to the angle of the moving link. The position of the moveable rigid link was determined at each step through the kinematic relationship between the springs and links, and by the forces applied to the springs at each increment. At each step, the reaction torques on the torsional springs and the reaction force on the axial spring were found for the initial position. The changes in angle and length of the springs were then found based on the spring constants, and the positions and angles of the springs and moveable rigid link were changed according to these values. Decreasing the size of the increment in which the force was applied did not significantly change the results of these simulations.

Using the above geometries, loading conditions, and geometry compensations, the 1-spring PRB model, 3-spring PRB model, and FEA results were all compared for bending and tension simulations. Only the results of the 3-spring PRB model are shown in Figs. 3.13 and 3.14 because the 1-spring model results are visually indistinguishable from the 3-spring model results in the pure bending case (though the numerical results are slightly different), and 1-spring PRB model results do not exist in the tensile case. The 3-spring PRB model matches the FEA characterized samples within 3% error for pure bending up to angular deflections of $\Delta\theta = 60°$ (Figure 3.13). Similarly, the 1-spring PRB model represents the FEA behavior within 4% error up

to the same $\Delta\theta$. Without using the shape factor for the trapezoidal shaped joints, maximum error increased to 20% over angular deflections of only 16° for geometry type 2. The tensile load tests for the 3-spring PRB model were accurate to within 7% error of the FEA results (Figure 3.14) over a 55% strain. Without the correction for the adhesion geometry, this error increases to 25% over the same strain.

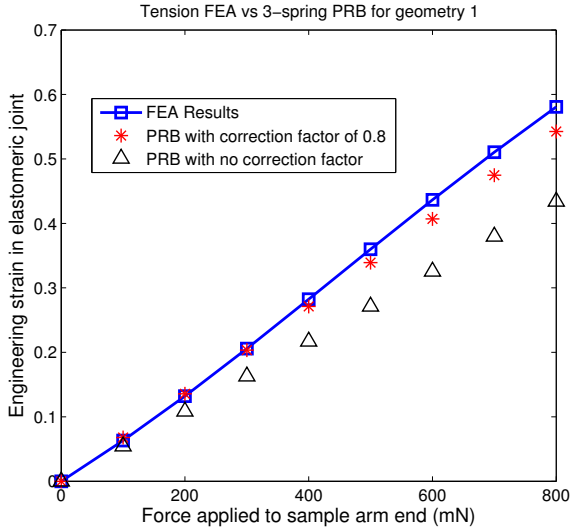

Figure 3.14: A comparison of FEA and 3-spring PRB results under a pure tension load

3.3 Evaluation of the 3-Spring PRB Model

While three springs have been incorporated into the new joint model up to this point (two torsion springs and one axial spring), it is important to determine how adding more springs would further improve the model accuracy with respect to FEA. To design mechanisms that utilize these joints, there must be a balance between model simplicity and accuracy. Therefore, the results of ten different PRB models

were compared under different loading conditions that combined bending and tension loads. The models used from 1 spring to 19 springs, with odd-numbered spring counts only, due to the arrangements of springs – n torsion springs alternating with $n-1$ axial springs. The accuracy of these models is determined by comparing the results of each to equivalent FEA simulation results. Only geometry type 1 was used, with a hinge of 1 mm length, 0.8 mm width, and 1.6 mm thickness.

The four simulations each consisted of a fixed arm and a free arm with an applied load. The directions of the applied forces for each test are pictured in Figure 3.15. For each simulation, one rigid link was constrained while a force of up to 20 mN was applied 4 mm away from the free end of the other 9 mm long rigid link. Case A applied the load perpendicular to the free arm to provide a pure bending load. Case B applied a pure tensile load. The two remaining loading cases are a mix of normally and tangentially applied loads. Case C and D are applied 45° to the instantaneous position of the free arm. In case C, the tangential component is tensile, while in case D the tangential component is compressive.

The FEA simulations were carried out using the same method described in Section 3.2. The PRB model simulations were carried out analytically in Matlab. In this simulation, the axial spring was constrained to move only in the line between the ends of two adjacent torsion springs, and the sum of the initial axial spring lengths equaled the initial distance between the ends of the rigid links in the Ansys^{TM} model. The spring constants for each model for two or more torsion springs were determined

using the following equations:

$$k_{\theta nspr} = \frac{nEI}{l_{eff}} \tag{3.11}$$

$$k_{lnspr} = \frac{(n-1)CAE}{l_{eff}} \tag{3.12}$$

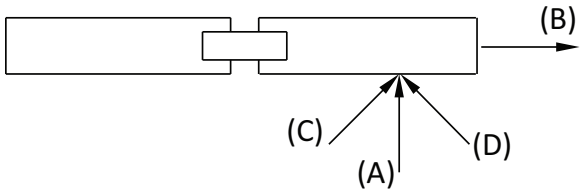

Figure 3.15: Forces as applied to the ten different PRB models with different spring counts

Each torsion spring within a model was assigned the same $k_{\theta nspr}$, and each axial spring within a model was assigned the same k_{lnspr}. The angle between the two arms was measured for each case, except the pure tensile case, where the extension of the elastomer hinge was measured.

The inner angles measured for 10 different PRB model configurations were found at the maximum 20 mN load for the first three loading conditions, and at 14 mN for the bending/compressive condition. Figure 3.16 shows these results compared to the corresponding FEA model for each condition, shown as a line across the plot for easy comparison. For each of the cases with a bending component, the performance of each model is not significantly different – the results are all within 1°. For the pure bending case, the 1-spring PRB model performs slightly better than the multi-spring PRB models, while for the bending/tension and bending/compression cases, the 1-

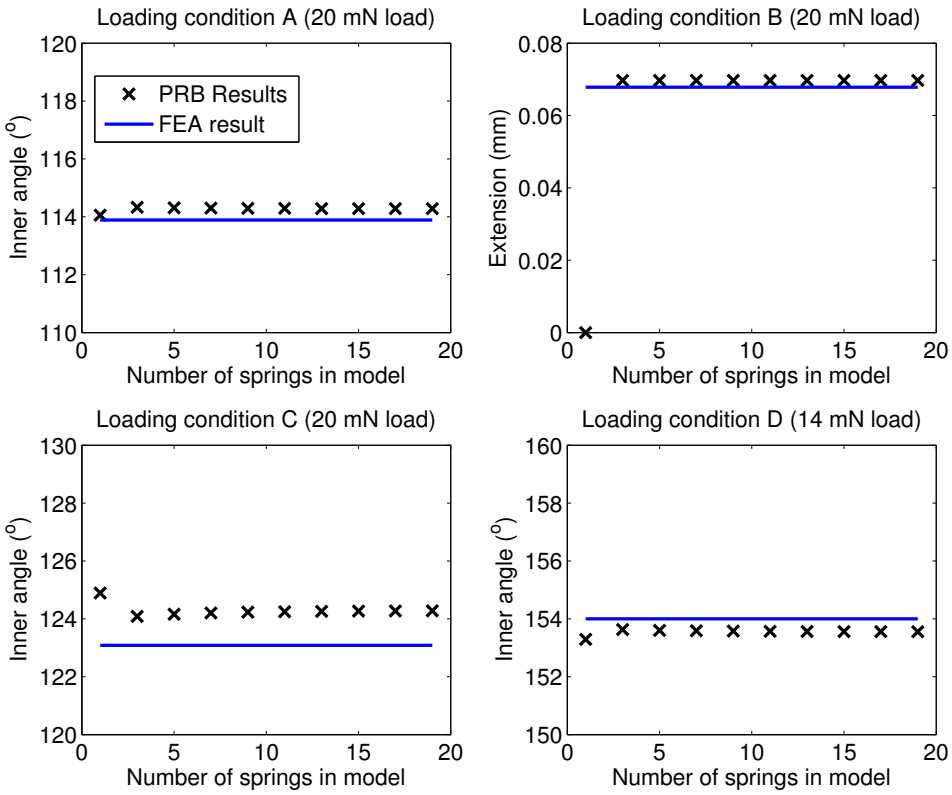

Figure 3.16: The inner angle results for FEA simulations and ten different PRB models with different numbers of springs. Angles were taken for a load of 20 mN applied in (A) pure bending, (B) pure tension, and (C) bending/tension, and at a load of 14 mN for (D) bending/compressive.

spring PRB model performs slightly worse than the multi-spring PRB models. This is logical, because pure bending and tension/compression are the behaviors intended to be captured by the 1-spring and multi-spring PRB models, respectively.

Additionally, the model under- or over-predicts the deflection of the hinge depending on the loading condition. Similarly, the measured angle increases or decreases with more springs added depending on the loading condition. However, these behaviors may be only artifacts of the discretization of the hinge material into individual

springs.

In general, however, for each of the bending conditions, the results are similar across the ten models, and quite accurate compared to the FEA result. This is not the case for the pure tension condition, (B). In this condition, the 1-spring PRB model cannot provide a result, while the multi-spring PRB models provide identical results, which are also quite accurate when compared to FEA. Taking each of these loading conditions and their results into consideration, it appears that the 1-spring PRB does not capture desired behavior. Furthermore, the small difference in results caused by adding more springs beyond the 3-spring PRB model does not justify the additional complexity of adding them, for these loading conditions. Based on these results, the 3-spring PRB model appears to be the best combination of performance and simplicity, and will be used for further mechanism modeling.

Chapter 4

Mechanisms

Several mechanisms have been designed for fabrication using the methods in Chapter 2, and have been modeled using the methods described in Chapter 3. This chapter discusses the design and modeling of some of those mechanisms, as well as testing of their fabricated realizations.

This chapter discusses meso-scale mechanisms. Section 4.1 discusses a meso-scale hexapedal walker that uses six identical leg mechanisms designed for fabrication using the LaCER process (described in Chapter 2, Section 2.1). The leg mechanism has been modeled using FEA, as well as the 1 and 3-spring PRB methods (described in Chapter 3, Section 3.2). Section 4.2 discusses leg mechanisms which have been designed for use on a running micro robot. These designs have been prototyped using LaCER and tested on a 2-D testing platform. Section 4.3 discusses similar leg designs on a 3-D meso scale hexapedal walker actuated using embedded magnets. The leg design was optimized for speed by Ryan St. Pierre and fabricated using the LaCER process.

4.1 Mobile Millirobot

The majority of the text in the following sections is taken from "Multi-Material Compliant Mechanisms for Mobile Millirobots" [38].

A hexapedal millirobot was created using the design and modeling methods described in the previous sections, and is pictured in Figure 4.1. The six legs are driven by a single crankshaft, which is in turn driven by a motor fixed to a frame. The crank rotates along the centerline of the frame, and each leg pivots about one of the side bars of the frame. As seen in Figure 4.2, the hexapod moves side-to-side. Arrows show the instantaneous direction of movement for each visible foot. The feet all move in continuous, out of phase semi-elliptical paths (clockwise in Figure 4.2), so that three legs are moving forward as the remaining three support the robot's weight. The current prototype can walk forward and backward, and is not yet steerable.

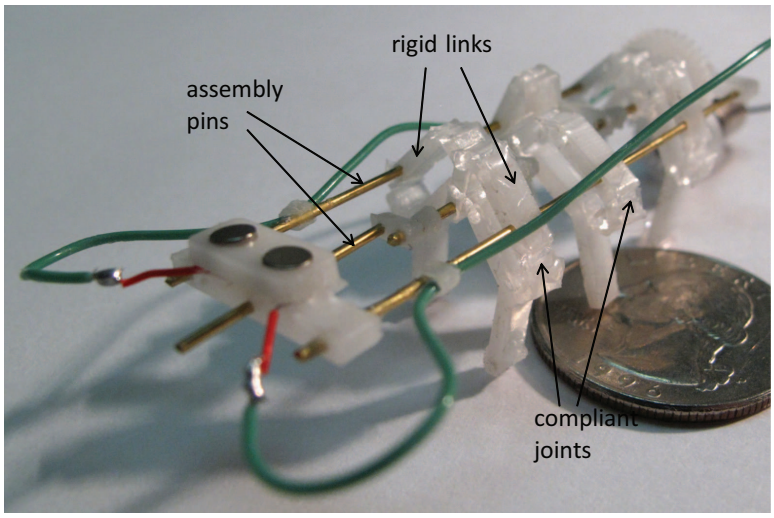

Figure 4.1: Hexapedal robot fabricated using LaCER and manual assembly onto a frame.

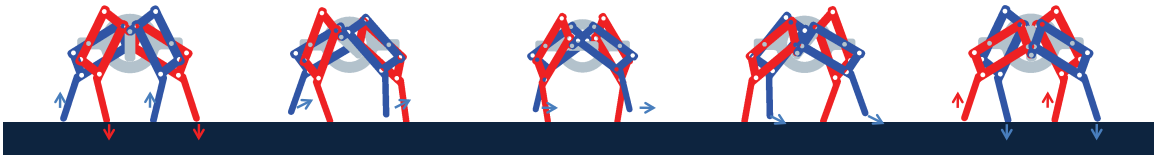

Figure 4.2: The red legs support the robot's weight as the blue legs are transferred from left to right, the process repeats with the blue legs supporting. Both sets of legs act as a tripod; one red leg is hidden on the left side, and one blue leg is hidden on the right.

So far, all prototypes have been constructed from Delrin rigid links and PDMS compliant joints. Delrin was chosen because it is very simple to laser cut. PDMS was chosen because it has a low enough Young's modulus that we can create many joints to be actuated in parallel by a small motor. PDMS also results in joint dimensions compatible with the minimum feature sizes of this proccess. The motor is a 5 mm gearmotor from Solarbotics, Inc., and the battery is a 3.7 V, 30 mAh lithium polymer cell from Plantraco Ltd. Including cutting, curing, assembly and basic electrical connection times, one hexapod can be fabricated in a total of about 6 hours.

4.1.1 Leg Design

The goal of the leg design was to create a compliant mechanism which would, when affixed in some way to a rigid frame, produce a repeating semi elliptical path at the end of the leg. Using this type of foot path, and three sets of two legs fixed oppositely from one another, three of the six legs will be on the ground at all times, resulting in a stable gait. The solution we provided for this problem is essentially an extension of a fourbar crank-rocker, with two additional links to achieve an ellip-

tical foot path not achievable by a crank-rocker alone. Figure 4.3 shows the basic mechanism.

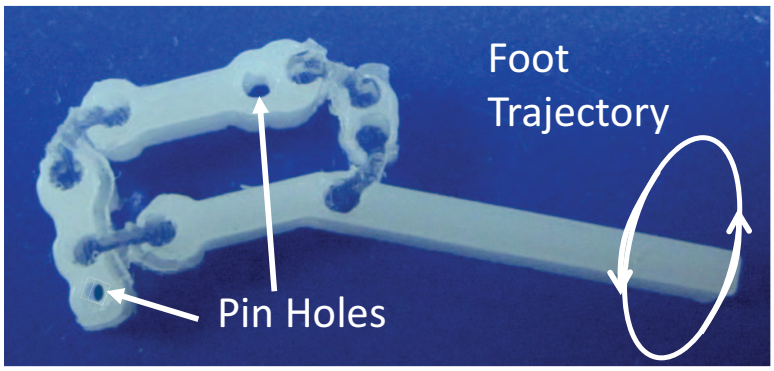

Figure 4.3: Closeup of one compliant leg mechanism.

The legs can be somewhat modified from their basic form for different purposes, such as optimizing for speed, for a smooth ride on the frame, for a lower center of gravity, or to accommodate a motor placed off-center for gearing down.

4.1.2 Results

The assembled robot measures 2.5 cm x 2.5 cm x 7.5 cm, with a mass of approximately 6 g (without a controller board or sensing payload). Geared down, it has been demonstrated to run at approximately 6 cm/s. This was determined by examining high speed video, with a known increment of time between frames, of the robot running over graph paper of known grid size. Based on step size and maximum step speed, we estimate that it could run at up to 17 cm/s if instability problems are resolved.

4.1.3 Leg Modeling

The majority of the text in the following sections was taken from "Characterization and Modeling of Elastomeric Joints in Miniature Compliant Mechanisms" [41].

The hexapedal leg mechanism has not been optimized for the demonstrations discussed above. This was mainly due to a lack of appropriate modeling methods, as discussed in Chapter 3. The following sections discuss modeling methods which could potentially be used to optimize the leg for speed if applied to a walking simulation of the full robot, though this analysis has not yet been satisfactorily completed. (However, an initial attempt at using the 3-spring PRB model for optimization can be found in "Modeling and Optimization of a Miniature Elastomeric Compliant Mechanism Using a 3-Spring Pseudo Rigid Body Model" [48]).

4.1.3.1 Setup

An FEA simulation of a single leg was carried out under the same material and element conditions described in Chapter 3, Section 3.1.2. An equivalent leg was modeled in a dynamics simulator, MSC Adams, using the 1-spring and 3-spring PRB models. Finally, a leg with equivalent geometric parameters was fabricated using the LaCER prototyping process to verify these models. As the FEA and prototyping processes have already been discussed, the setup for the two PRB models will be

discussed in more detail here.

The use of a dynamics simulator was chosen for convenience. There are many more degrees of freedom present in the leg modeled with the 3-spring PRB method versus the 1-spring PRB method. Furthermore, the forces applied to each spring of each joint must be calculated at each step to determine the positions of the links, rather than using simple kinematic relationships to determine the positions. These calculations are built into the dynamics engine in MSC Adams, resulting in a simple method for mechanism design iterations.

Additionally, a sub-class of mechanisms will not experience significant tension in some of the joints, and design can be simplified end sped up by using a 1-spring PRB model for these joints. To determine if this is the case, designers can start with a 1-spring PRB model, observing tension in the joints during the simulation. For elastomeric joints in which tension is not significant, they can safely remain modeled as 1- spring PRB hinges, while the others are converted to 3-spring PRB hinges. These joints should be monitored on successive runs to ensure that this method remains valid. The joints in the following simulations experience significant tensile and compressive loading over the different runs, and so have been all modeled as 3-spring PRB hinges. To model a 1-spring PRB joint in MSC Adams, a rotational joint and a torsional spring connect the links at the replaced hinge's center of rotation. To model a 3-spring PRB joint, a pin is placed wherever a replaced hinge meets with a rigid link. A rotational joint and a torsional spring connect the pin to the link. A

translational joint and an extension spring connect the two pins on either side of the replaced hinge. To ensure the accuracy of this method, a single hinge was modeled in both MSC Adams and MATLAB using the 3-spring PRB model. The error in these results was less than 0.5% for the four loading conditions described in Chapter 3, Section 3.3.

Equation 3.7 was used for the 1-spring PRB model, while Equations 3.8 and 3.9 were used for the 3-spring PRB model. The geometric parameters and spring constants used for the leg model in MSC Adams are given in Table 4.1, based on the geometry shown in Figure 4.4–the same geometry used for the fabricated version of the leg. Here, E is the Young's modulus, w_l and w_h are the widths of the links and hinges, respectively, l_{nm} is the first or second ($m = 1$ or $m = 2$) length on link n, l_{hn} and l_{effn} are the length and effective length of hinge n, and k_{hn} and k_{ln} are the spring constants of the torsional and axial springs in hinge n for the 3-spring PRB model. For the 1-spring PRB model, $k_{\theta 1spr} = (1/2)k_{\theta 3spr}$. Note that because hinges 1 and 2 are curved, $l_{eff1,2} > l_{h1,2}$. Because hinges 3 and 4 are trapezoidal, $l_{eff3,4} < l_{h3,4}$, as discussed in Chapter 3, Section 3.2.1. Additionally, a compensation factor, $C = 0.79$, was used due to the adhesion geometry length of $l_g = 0.6$ mm, as discussed in Chapter 3, Section 3.2.2.

The two PRB leg models, the FEA leg model, and the fabricated leg were subjected to the same sets of loading conditions, and the position of the foot was monitored in each case. The first condition simulates the robot standing stationary

Table 4.1: Leg Geometry parameters and spring constants

$E = 1.4$ MPa, $w_h = 0.8$ mm, $w_l = 2.0$ mm, $t = 1.6$ mm				
Link/hinge #	1	2	3	4
l_{nm} (mm)	1.4/2.7	4.2/6.4	10	2.6/6.2
l_{hn} (mm)	0.92	0.87	0.92	0.84
l_{effn} (mm)	1.06	1.07	0.79	0.78
k_{ln} (mN/mm)	1390	1370	1880	1900
$k_{\theta n}$ (mN/rad)	185	183	250	254

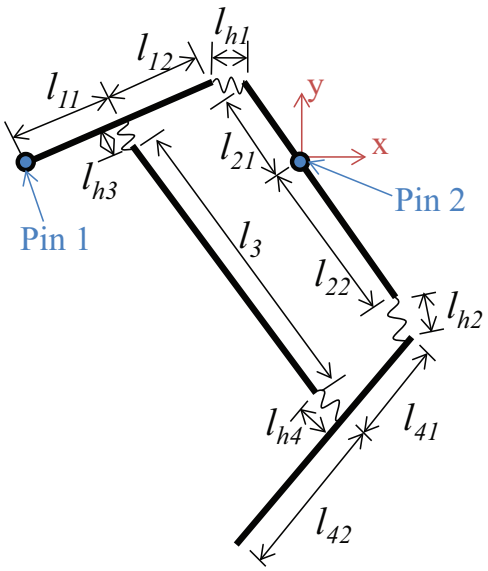

Figure 4.4: Leg geometry and parameters.

in one of its alternating tripod positions. Thus, 20 mN, simulating 1/3 of the total mass of the robot (total mass–6 g) was applied as a vertical reaction force on the foot, while the two pin joints were held fixed in x and y, with rotation allowed about the pins' z-axes (Figure 4.5, Condition 1). Similarly, a load of 73.3 mN was applied to the foot to simulate the robot standing with a 16 g payload, and 100 mN to simulate the robot standing with a 24 g payload. For these cases, the position of the foot is assumed to be relative to a fixed coordinate frame attached to the pins, as labeled in

Figure 4.4. The positions are measured relative to the unloaded initial position. The surface is also assumed to be frictionless, so there are no reaction forces or constraints in the x-direction. This loading condition was simulated using the 3-spring PRB and FEA models. The 1-spring PRB model was not able to model this condition. When the two pins are held stationary, the kinematics of the leg as currently designed require lengthening of the joints for the foot to move, which is not allowed with the 1-spring PRB model. For the fabricated leg, the loading condition was carried out by slowly lowering the leg, mounted on two stationary pins, onto a scale to measure the reaction force. A sheet of greased Teflon was positioned under the leg as the contact surface, to reduce friction. At each load level described above, photographs were taken of the leg, and these photographs were calibrated and inspected using TSView to determine the position of the foot at each point.

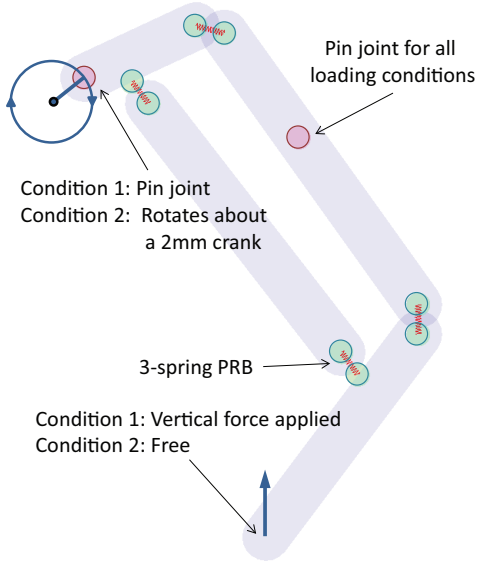

Figure 4.5: The leg modeled in MSC Adams, and the two different loading conditions.

The second loading condition simulates the leg's free displacement during a single rotation of the driving crank. Pin 2 was held stationary in x and y with allowed rotation about the pin's z-axis, while the pin 1 joint was prescribed a fixed displacement corresponding to a rotation of the driving crank around its central axis (Figure 4.5, Condition 2). The position of the foot was measured relative to its initial position, at a crank rotation of 0 rad, as measured from the $+x$ axis labeled in Figure 4.4. This loading condition was simulated using the 1-spring PRB, 3-spring PRB, and FEA models. For the fabricated leg, the loading condition was carried out by mounting the leg on a frame with pin 2 allowed to rotate, and pin 1 attached to a 2 mm crank driven by a 6 mm gear motor identical to those used to drive the hexapedal robot. The motor was used to drive the leg around several crank cycles, while high speed video captured the leg's behavior. TSView was again used on screen shots from the resulting video to determine the crank angle and foot position over the course of a full crank cycle.

4.1.3.2 Modeling Results: PRB vs. FEA

The results of the ground reaction force conditions suggest that the 3-spring model is quite accurate for this mechanism, when compared to the FEA results. The maximum displacement of the foot occurred under a load of 100 mN, resulting in an x displacement of 0.84 mm in ANSYS and 0.86 mm in Adams and a y displacement of 1.30 mm in ANSYS and 1.42 mm in Adams. This corresponds to a maximum error

of 7.3% in the direct path of the foot for these conditions. The x and y positions of the foot under each condition using FEA and the 3-spring PRB model are plotted in Figure 4.6, left.

The free displacement condition shows similarly accurate results in the 3-spring PRB model, when compared to FEA results. The maximum error in the y position of the foot was 12% at a crank angle of $\theta_c = \pi$ rad, and the maximum error in the x position of the foot was 8% at a crank angle of $\theta_c = 0.9$ rad–the point where the x-displacement is highest in the positive direction. The 1-spring PRB model does a good job modeling the free displacement of the foot over most of the crank cycle. However, for one portion of the cycle, the crank is not able to reach the prescribed position due to inadequate length in the links to allow the leg to reach these positions. The x and y positions of the foot over one rotation of the central crank are plotted in Figure 4.6, right. In this figure, the FEA results are not smooth, due to incrementally moving the model into position along the crank cycle. Additionally, the divergent areas in the 1-spring PRB model demonstrate that the model is physically constrained from moving along the expected path. These divergent areas could be avoided by using a slightly different, kinematically feasible leg geometry, but this behavior demonstrates that the 1-spring PRB eliminates a subset of valid design choices when elastomeric joints are used, putting artificial limits on the design space.

These results indicate that the 3-spring PRB model can accurately match an FEA model of a multihinged mechanism with elastomeric joints. The PRB model also

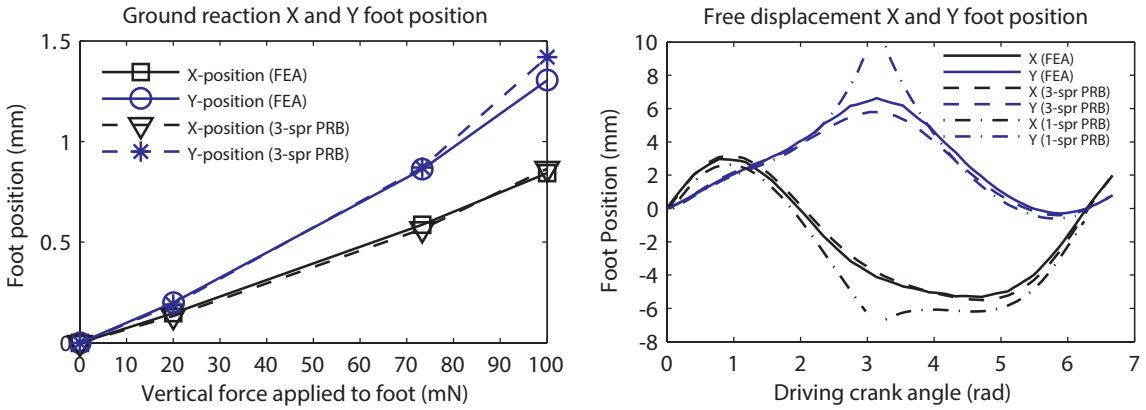

Figure 4.6: The x and y positions of the robot foot, relative to the initial position: under three different ground reaction force loadings (Left); and over a full crank rotation (Right). Obtained from FEA, 1-spring PRB, and 3-spring PRB models.

provides considerable time savings due to its high computational efficiency. A multistep simulation of movement in a complicated mechanism, such as this mechanism in the free displacement loading condition, can take hours to solve using traditional FEA. The behavior of the mechanism under the same loading conditions can be determined accurately using this 3-spring PRB method in less than 1 min.

4.1.3.3 Modeling Results: PRB vs. Experimental

The results of the first loading condition modeled with the 3-spring PRB model are plotted, along with the experimental results in Figure 4.7, left. The 3-spring PRB model results match the experimental data within 9% in x and y when the elastic modulus of the joint material used is reduced by 40% in the PRB model. This

reduction in joint modulus resulted from a reduction in the curing time during the leg fabrication, though the exact times were not recorded. This change in modulus is consistent with previous work showing that the elastic modulus of PDMS can vary by at least 37% due to changes in the curing procedure [49]. These results illustrate the value of careful material preparation and characterization in fabricated mechanisms.

The free displacement condition, on the other hand, shows a good match between the experimental results and the 3-spring PRB model results using both the original modulus and the decreased modulus. The path taken by the foot during the crank cycle is nearly identical for both moduli (Figure 4.7, right), due to the low forces that the joints experience in this condition. The path of the foot in this case is mainly determined by the kinematic relationships between the links. The 3-spring PRB models match the experimental data within 20% in x and within 22% in y.

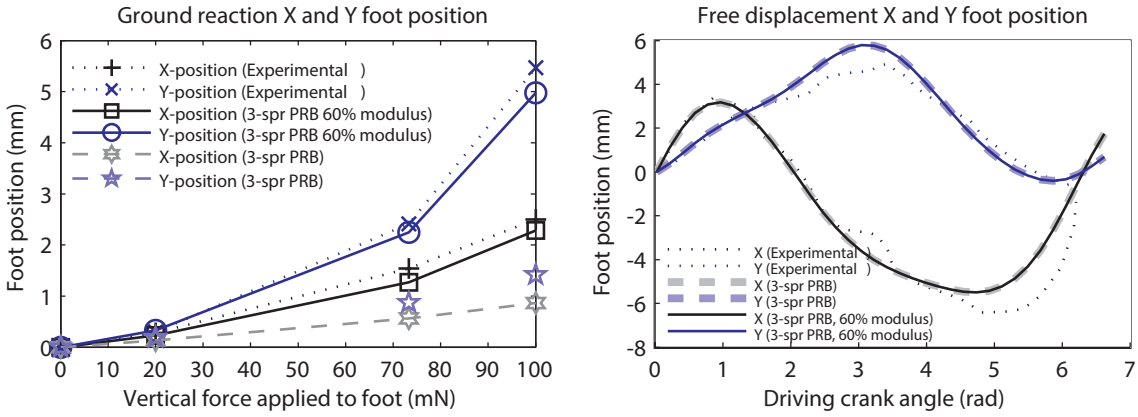

Figure 4.7: The x and y positions of the robot foot, relative to the initial position: under three different ground reaction force loadings (Left); and over a full crank rotation (Right). Obtained from Experimental data, 3-spring PRB modeling with previously used modulus, and 3-spring PRB modeling with 60% modulus.

The design discussed here proved an effective tool for locomotion at the meso

scale, as well as for exploration of modeling and optimization techniques. However, as micro-scale legs are the ultimate goal, simpler leg designs without the need for fully rotational actuation are explored in the following sections.

4.2 Prototyped Asymmetric Underactuated Microrobot Legs

The majority of the text in this section is taken from "Progress Toward Mobility in Microfabricated Millirobots" [50].

4.2.1 Design

Asymmetric compliant legs were designed for planar fabrication and underactuated linear and rotary gaits. Significant variation is possible, but three basic designs were chosen–two for rotary actuation and one for linear actuation. Two versions of each of the three designs were investigated–with and without a gripping foot on one side of the end of the leg–for a total of six designs.

The geometry and timing of the legs' actuation profiles can also have a large effect on the performance of the legs. Two gait types were investigated–rotary and linear. It is possible to vary both these gait types over a variety of parameters, leading to many possible gaits. A few parameters have been selected for investigation in the current work.

4.2.1.1 Leg Design

Two legs types were designed for rotary actuation. The first consists of two links with a single passive hinge between them that can compress and rotate. This leg serves as the baseline for the rest of the rotary leg designs, as it is simple and symmetric. Some asymmetry was added by the addition of a gripping foot on one side of the leg, which will increase friction between the leg and the ground more on one side of the leg than the other (Figure 4.8-1).

The second leg designed for rotary actuation is similar to the first, but includes a kneecap, a small piece of rigid material present on one side of the passive hinge. This prevents the hinge from bending in the direction of the kneecap, and allows the leg to apply greater force to the ground in one direction than in the other. A gripping foot can also be added to this design on the opposite side of the leg from the kneecap (Figure 4.8-2).

A single type of leg was designed for linear actuation. This design is essentially identical to the first type of rotary actuated leg, but is intended to be driven linearly along its axis. Only one side of the leg contacts the ground, making this leg design inherently asymmetric. This design is more similar to the legs in the Sprawl family of robots. In this case the gripping foot only increases friction between the leg and the ground, but does not increase the asymmetry of the leg(Figure 4.8-3).

For each of the three leg designs, the length and width of the links can be varied, as well as the size and stiffness of the joint. The size and placement of the foot can

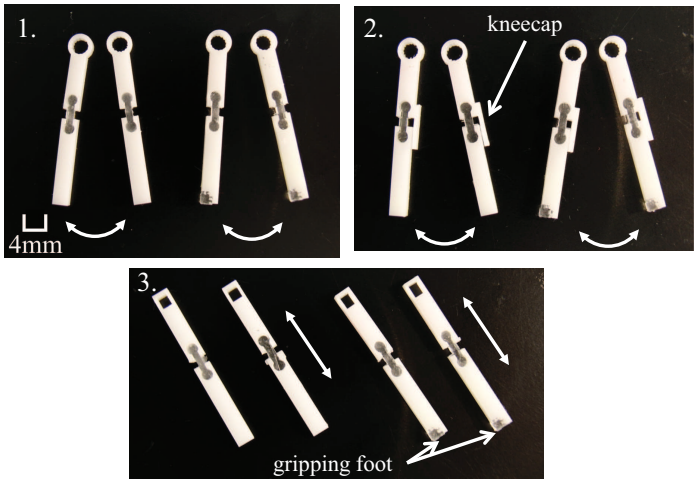

Figure 4.8: All three leg types. 1. Leg type 1, 2. Leg type 2, 3. Leg type 3. For each: left:no gripping foot, right: gripping foot.

also be varied. However, variation of the leg geometry has not been explored here.

4.2.1.2 Gaits

The rotary gait is applied by starting both legs (or sets of legs) at an angle of θ_1 to the ground normal (Figure 4.9, left). One leg, leg A, is oriented to the left of center, in its position 1. The other, leg B, is oriented to the right of center in its position 1. Leg A then swings through an angle of θ_r to the right to its position 2, while leg B simultaneously swings through θ_r to the left to its position 2. Both legs then alternate between their positions 1 and 2. The rotary gait can be modified by changing θ_1 or θ_r, as well as by varying the speed at which the legs swing through θ_r, and the phase difference between the two actuation cycles.

The linear gait is applied by orienting both legs (or sets of legs) at an angle of

θ_l to the ground normal (Figure 4.9, right). The first leg, leg A, starts in contact with the ground in its position 1. The other, leg B, starts above the ground at a distance l_g in its position 1. Leg A is then pulled up out of contact with the ground to its position 2, while leg B is simultaneously pushed down into contact with the ground to its position 2. The linear gait can be modified by changing θ_l or l_g, as well as by varying the speed at which the legs are pushed and pulled through l_g, and the phase difference between the two actuation cycles.

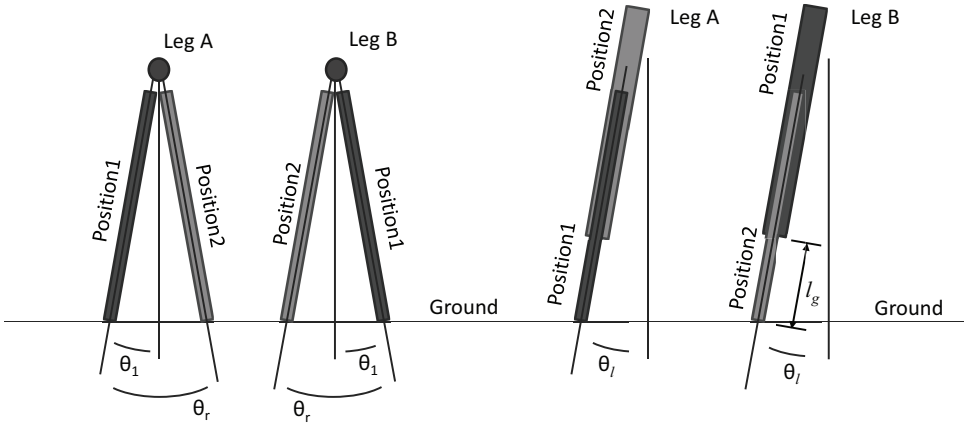

Figure 4.9: Left: General rotary gait. Right: General linear gait.

4.2.2 Fabrication of Prototyped Legs

As mentioned previously, the ultimate goal of this work is to microfabricate millimeter-scale legs using the process described in Chapter 2, Section 2.2. However, to test the validity of the models discussed in the previous chapters, a centimeter-scale verison of the test setup has been fabricated first. The larger scale prototypes of the legs were fabricated using the prototyping process described in Chapter 2, Section

2.2.

The rigid portions of the test legs were fabricated from Delrin and cut using a desktop laser cutter, a 60 W VersaLaser VLS3.50. The elastomeric hinges were fabricated from a pourable two-part elastomer, Dow Corning Sylgard 184 PDMS. The dimensions of each of the legs are: 2.4 mm in thickness; 15 mm x 4 mm for the first link, from the actuator to the hinge; 20 mm x 4 mm for the second link; and 2 mm x 1.3 mm for the elastomeric hinge.

4.2.3 Testing

4.2.3.1 Setup

The test setup was fabricated from Delrin using the same desktop laser cutter used to fabricate the legs. A modular base-top was fabricated along with legs to elevate it (Figure 4.10). Also fabricated were a flexure part to provide simulated weight to the legs and a treadmill surface for the legs to contact. Two linear or two rotary servos were used to drive two legs, and were programmed for different gaits using an Arduino Uno.

4.2.3.2 Results

Testing was done for each of the three leg types, each with and without a gripping foot, for a total of six pairs of legs tested. For each of the rotary tests, a θ_1 was chosen of 30°, with a θ_r of 60°, for a symmetrical gait. For the linear gaits, a θ_l

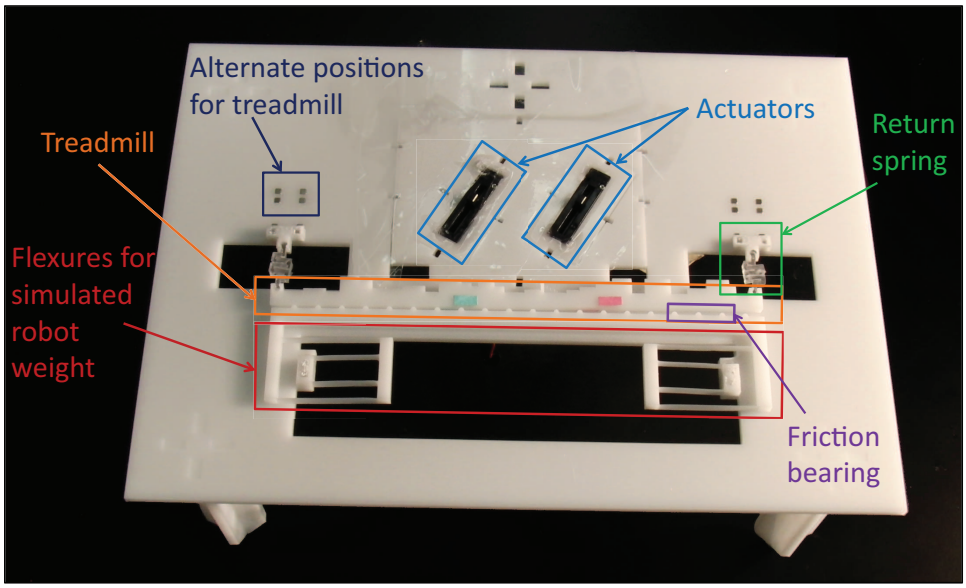

Figure 4.10: The test setup with a flexure part, a randomized-terrain treadmill, and linear actuators.

of 30° was chosen, and a l_g of 10 mm. All tests were driven at 1 Hz, or 500 ms per step. The linear actuators took the full 500 ms to travel the distance l_g, while the rotary actuators took only about 100 ms to travel θ_r. Ultimately, the servos used in this test setup will be replaced with faster models to test the legs at faster speeds as well. No vertical preload was applied to the legs, but a spring load of about 35.11 mN/mm was applied by the flexures (pictured in Figure 4.10) while the legs were in contact with the treadmill.

For each test, several steps were taken in order to advance the treadmill, and the setup was recorded at 1200 fps using a Casio EX-F1 camera with high speed video capability. A marker was placed at the center of a long, flat-terrain treadmill without return springs, and the position of the marker was monitored in x and y, though

only the x direction has been included in this document. The marker was monitored up to a maximum displacement of about 150 mm in the x direction, as this is the length of the friction bearing that supports the treadmill in the y-direction. If this distance was not reached, the experiments were stopped around 40-60 s, or 10-20 s if no movement was detected. The x displacement of the treadmill for six different leg pairs are shown in Figure 4.11.

Note that the time scales of these plots vary due to the testing time and the distance traveled during that time. Each of the legs which caused significant x-displacement in the treadmill generated a stairstep-type profile x-displacement plot. This is most visible for leg type 2 with foot, due to the short time scale and high displacements, but the same behavior is present for leg types 1 and 3 with foot, and leg type 2 without foot as well.

From these results it can be seen that the gripping foot improves the performance of all three leg designs, as types 1 and 3 do not move at all without the gripping foot, and type 2 moves much farther in a much shorter time with the foot.

Of the leg types tested with the gripping foot, type 2 performs the best, with an x-direction treadmill velocity of 55.6 mm/s. Type 3 performs second best, with a treadmill velocity of 26.0 mm/s. Finally type 1 performs worst, with a treadmill velocity of up to 1.08 mm/s. Leg type 2 with no gripping foot is similar in performance to leg type 1 with a gripping foot, with a treadmill velocity of up to 3.13 mm/s.

Based on these results, both the kneecap and the gripping foot appear to greatly

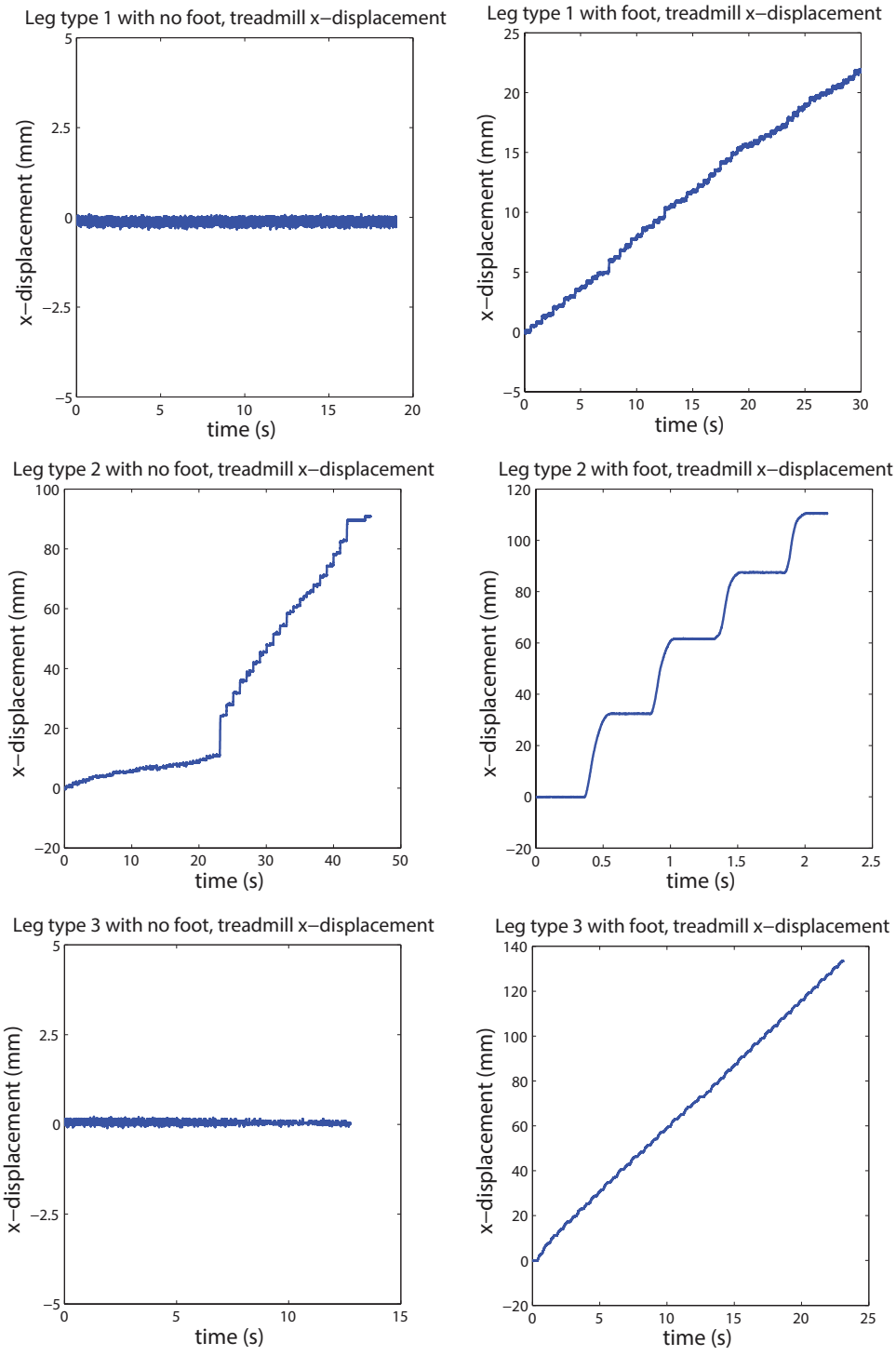

Figure 4.11: Experimental x displacement of treadmill over all leg types.

improve the performance over equivalent legs without these features.

4.2.4 Dynamic Model

4.2.4.1 Setup

A simplified version of each of the leg designs was modeled using MSC Adams (Figure 4.12). A leg with a linear and rotary actuator and a single 3-spring PRB model joint–as described in Chapter 3, Section 3.2–was modeled with different actuation schemes and different constraints on the PRB joint to imitate each of the designed leg types.

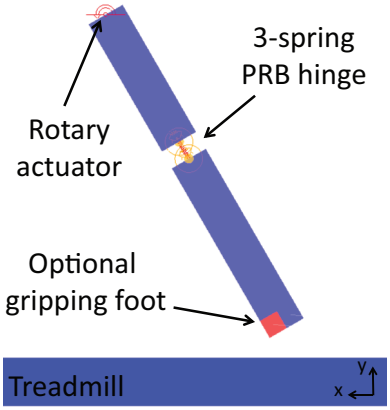

Figure 4.12: MSC Adams dynamic model of a type 1 leg, including a rotational actuator and an unconstrained 3-spring PRB hinge model.

For the first leg type, a rotary actuation scheme was used along with an unconstrained PRB joint. For the second type, a rotary actuation scheme was used, and the PRB joint was constrained from moving past 180° in one direction. For the third type, a linear actuation scheme was used, and the PRB joint was left unconstrained.

Table 4.2: Leg geometry and model parameters

Geometry (mm)		Material/Spring Constants	
t	2.4	E_{PDMS}	1.60 MPa
l_{link1}	15.0	ζ_{PDMS}	0.15
l_{link2}	20.0	$k_{treadmill-y}$	35.11 mN/mm
w_{link1}	4.0	k_l	2688 mN/mm
w_{link2}	4.0	k_θ	878.1 $mN-mm/rad$
l_{hinge}	2.0	c_l	0.491 $mN-s/mm$
w_{hinge}	1.4	c_θ	2.811 $mN-mm-s/rad$

Friction coefficients			
μ_s Delrin-Delrin	0.05	μ_s PDMS-Delrin	0.5
μ_d Delrin-Delrin	0.03	μ_d PDMS-Delrin	0.3

A moving treadmill was set up below the legs, and was pushed forward by the feet during each of the tests. A frictional resistance was defined for the treadmill's motion to simulate the sliding of the treadmill on the horizontal plane as well as along the friction bearings that are present in the fabricated treadmill (as discussed in the Prototypes section). A vertical spring force was also defined between the ground and the treadmill to provide vertical resistance to the feet as they move through the gaits (representing gravitational force). Additionally, a separate contact between foot and treadmill was defined for the left and right side of each foot. This allowed for simulation of the gripping foot, if two different coefficients of friction were defined, or no gripping foot, if the same coefficient was defined for both sides. Parameters for these models are given in Table 4.2.

4.2.4.2 Model vs. Experimental

The modeled leg was compared with the experimental results for leg type 1 with a gripping foot. The results of this comparison are shown in Fig. 4.13.

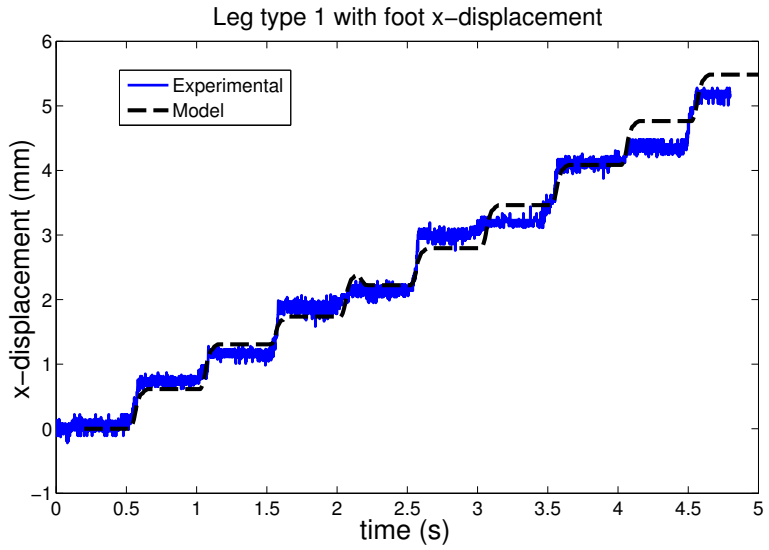

Figure 4.13: Experimental and model treadmill x-displacement over 5 seconds. Leg type 1, with foot.

This result shows that the model is capable of closely matching the behavior of an experimental leg. The average step size of the modeled type 1 leg with foot is 0.61 mm over the 5 seconds shown here. The average step size of the experimental type 1 leg with foot is 0.54 mm over 35 seconds, resulting in a model error of about 13%.

4.2.5 Scaling down prototyped designs

In order to use the designs prototyped in this section as scaled-down micro robot legs, alternative actuation methods must be explored. Ultimate possibilities for ac-

tuation on the micro scale include thermal or electrostatic actuators, or electrostatic inchworm drives for large linear displacements. However, as discussed in Chapter 2, Section 2.2, the step of actuator selection and integration can be circumvented through the use of embedded magnets, and the designs can be fabricated on the micro scale using the process described in the same section. First, 3D magnetically-actuated hexapods using these leg designs were prototyped using LaCER with embedded magnets.

4.3 Magnetically Actuated Hexapod

The majority of the text in this section is taken from "Model-Based Insights on the Design of a Hexapod Magnetic Walker" [51].

Legged robots on the millimeter scale present challenges in design, actuation, and fabrication. A 1 cm^3 magnetically actuated hexapedal walking robot, Figure 4.14, was fabricated using LaCER (as described in Chapter 2, Section 2.1). The fabricated optimized walker is capable of speeds up to 10.6 body lengths per second.

4.3.1 Design of leg/walker

The legs were chosen as the best performers from the previous section, leg type 2 with a gripping foot (Figure 4.8). They are simple, underactuated legs, having only two degrees of freedom: an active rotational hip joint and a passive rotational knee joint. The active hip joint is actuated by an applied torque from an embedded

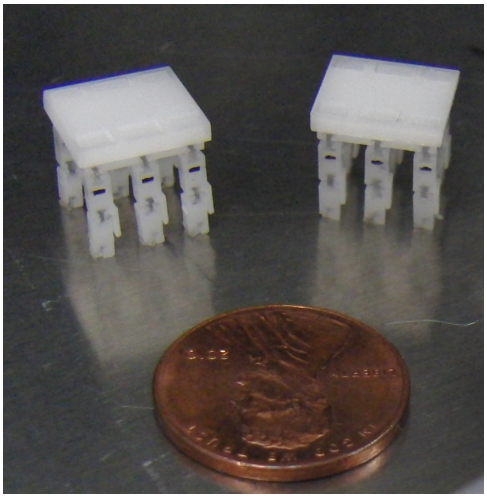

Figure 4.14: Photograph of two 1 cm^3 magnetically actuated hexapedal walking robots.

permanent magnet subjected to an external magnetic field, rather than using a servo motor as in the previous section.

Six of these legs are arranged 90° to the flat walking surface, with three on either side of a central body. The legs are then driven from the active hip with alternating positive and negative applied torques. The sign of the applied torque is opposite on opposing tripods, resulting in an alternating tripod gait. The robot was modeled and optimized for speed by Ryan St. Pierre. Details of this modeling and optimization can be found in [51].

4.3.2 Fabrication

The legs were fabricated using a prototyping process, Laser Cut Elastomer Refill, (LaCER), as described in Chapter 2, Section 2.1.

Table 4.3: Dimensions of fabricated walkers. All dimensions in mm.

Build	L_1	L_2	W_{leg}	$W_{flexure}$	L_{body}
O	4.5 ± 0.1	2.5 ± 0.1	1.8 ± 0.1	0.3 ± 0.1	10
E	3.5 ± 0.1	3.5 ± 0.1	1.8 ± 0.1	0.3 ± 0.1	10
R	2.5 ± 0.1	4.5 ± 0.1	1.8 ± 0.1	0.3 ± 0.1	10
S	2.5 ± 0.1	2.5 ± 0.1	1.8 ± 0.1	0.3 ± 0.1	14

Small magnets, 1 mm length 0.75 mm diameter cylindrical N50 neodymium magnets with a parylene coating were embedded in each of the legs to provide the alternating actuation torque under influence of a rotating external magnetic field. To embed the magnets, the legs were oriented over a large magnet so that the small magnets placed on the surface of the leg were automatically oriented and held in place in the external magnetic field. The oriented small magnets were then pushed down with tweezers into a space cut into the legs intended to hold the embedded magnets. They are held in place by a surrounding thin ring of PDMS deposited during the fabrication of the hinges, as well as a dot of glue for added security.

4.3.3 Fabricated walkers

Four magnetic walkers were fabricated with different dimensions for their legs. The dimensions of the four walkers are summarized in Table 4.3.

Build O has dimensions that were identified by Ryan St. Pierre as optimal for leg link lengths. Build E has even link lengths. Build R has link lengths reversed from the optimized geometry. Build S has shorter, even link lengths, and a longer body length as identified. An additional build P was also created with "peg-legs"–without

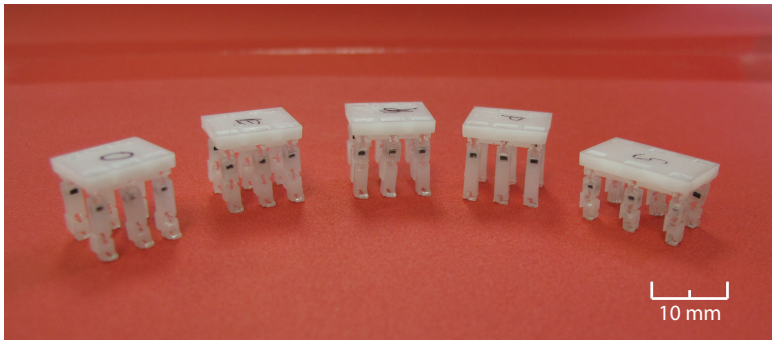

Figure 4.15: Five walker builds. From left: Optimized, Even, Reversed, Peg-leg, and Short.

a knee joint (Figure 4.15).

4.3.4 Experimental set up

Each walker is actuated by an external magnetic field rotating at 5 Hz. In a separate experiment, frequency was varied. The rotating magnetic field is provided by mounting a 1 $inch^3$ N55 neodymium magnet on carbon fiber rods mounted on ball bearings to support the weight of the magnet. One end of the mounted magnet assembly is attached to a 30 mm diameter DC motor which was driven at 3.5 V to produce rotation at 5 Hz, and up to 12V to produce rotation up to 26.7 Hz. The mounted magnet setup is shown in Figure 4.16.

A thin sheet of transparent acrylic was supported just above the rotating magnet setup. Cardstock guides were mounted to the acrylic sheet to direct the path of the walkers. Because the distance at which the rotating magnet can actuate embedded magnets in the walkers is only a few centimeters, the acrylic sheet was moved over

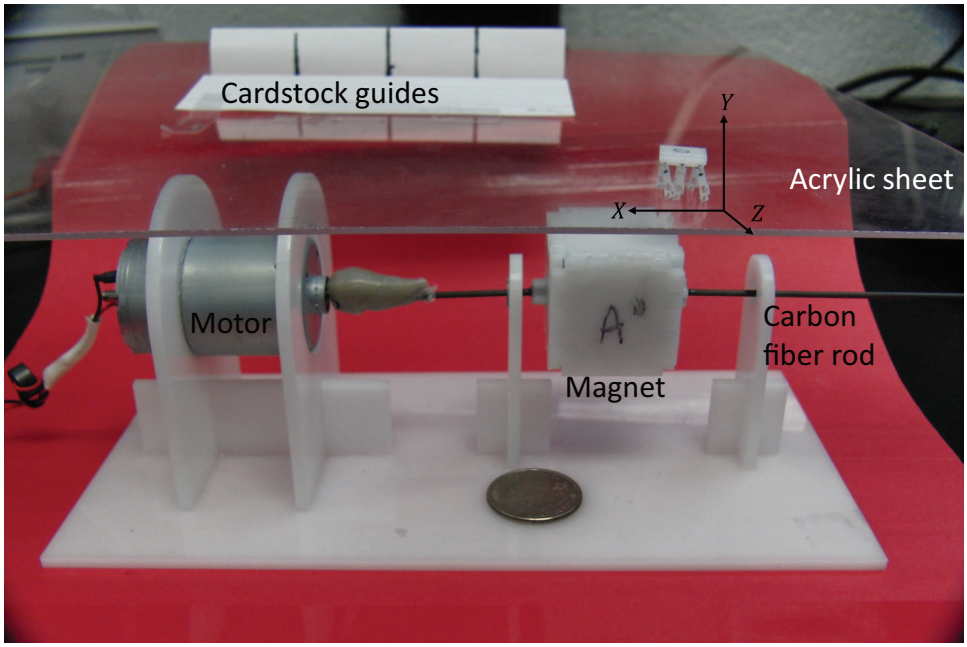

Figure 4.16: Experimental setup showing the magnetic mounted and attached to a DC motor.

the setup to keep the walker's current position centered over the rotating magnet during testing. When the walkers are placed on the acrylic sheeting, the magnets embedded in the legs are positioned 25-27 mm (depending on the build) from the surface of the rotating magnet. An AD22151 sensing chip from Analog Devices was used to measure a field intensity, B, of approximately 60 mT at this distance. The direction of the magnetic field vector at this location, $\overrightarrow{B}$, varies with the rotation of the mounted magnet, and the y-direction projection of this vector was collected over several cycles at roughly 5 Hz (Figure 4.17).

A sample of each build was tested walking in this rotating magnetic field over a distance of 60 mm during several trials. Distance markers were drawn on the cardstock guides to determine the distance and the time was recorded using video of

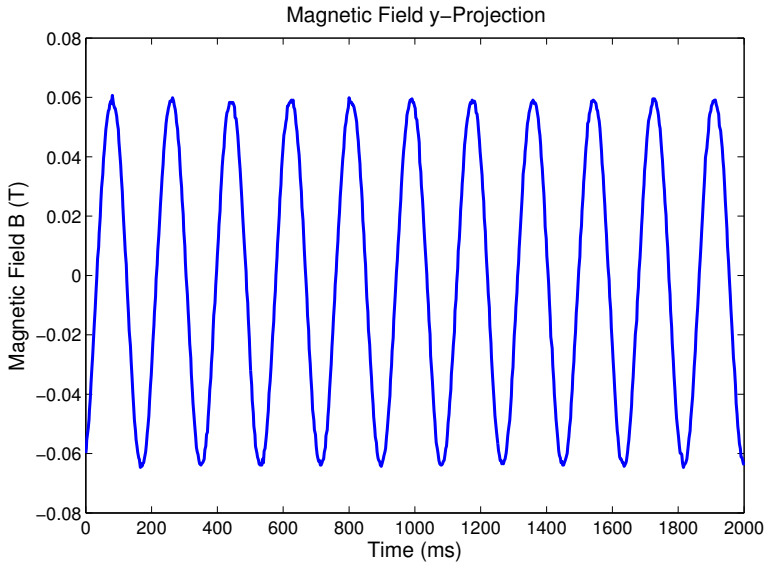

Figure 4.17: The y-component of the magnetic field vector applied to the hexapod legs over several cycles at about 5 Hz.

the trials.

4.3.5 Results

The different builds were tested as described in section 4.3.4 over at least 7 trials each. The walkers were recorded during their motion. The distance traveled and travel time was evaluated from the videos. The experimental data and simulated average velocities are shown in Table 4.4. The peg-leg walker's performance was not simulated and is not reported in the table. However, it was tested and walked at an average velocity of 1.4 mm/s.

The optimized build (build O) was additionally tested at multiple driving frequencies up to 26.7 Hz, and displayed a maximum speed over a single trial of 106

Table 4.4: Experimental and simulated average velocities.

Build	Experimental(mm/s)	Simulated(mm/s)
O	9.7 ± 1.4	9.1
E	8.3 ± 1.0	8.3
R	4.2 ± 0.6	3.9
S	9.4 ± 1.2	7.9

mm/s, or 10.6 body lengths per second. This was the fastest speed (in body lengths per second) observed in any of the magnetic walkers thus far.

These robots present a step toward legged micro robots, but this 1 cm^3 size represents the limits of the LaCER prototyping process. In order to achieve smaller sizes for testing of micro robotic leg designs, microfabrication was explored. The performance of microfabricated magnetically actuated mechanisms, are discussed in the remaining chapters.

Chapter 5

Magnetic actuation of a microfabricated hinge mechanism

The majority of the material in this chapter is taken from "Magnetic actuation of thick film multi-material compliant mechanisms" [40].

This chapter presents work done to characterize the magnetic actuation of a microfabricated, ultra-compliant hinge mechanism. The first section describes the hinge and the principle under which it is actuated using embedded magnetic material. The second section discusses experimental characterization of the compliant hinge, independent of the actuation method, including both static and dynamic properties of the hinge material. The third section characterizes the hinge undergoing both static and dynamic magnetic actuation. Finally, at the end of the chapter, a more complex 14-link, 11-hinge gripper is presented to further demonstrate the capabilities of the fabrication process and actuation method.

This chapter is intended to introduce and explore in-depth the behavior of a simple magnetically actuated mechanism, as well as present the more complex capabilities of the fabrication process, in order to lay the groundwork for further exploration of other magnetically actuated mechanisms.

5.1 A simple magnetically actuated micro mechanism

The single-link, magnetically actuated micro mechanism was chosen as a simple tool for investigation of magnetic actuation of micro fabricated silicon-elastomer mechanisms. This section introduces the hinge mechanism itself as well as the principle behind its actuation using embedded magnetic materials.

5.1.1 A single-link mechanism

The single-link mechanism (Figure 5.1) consists of a single rigid silicon link connected to a ground link via a straight-line elastomer hinge with a rectangular cross section. The moving silicon link includes a sleeve with a single embedded micro magnet. The mechanism was fabricated using the process described in Chapter 2, section 2.2. Hinge dimensions of 189 μm x 113 μm x 300 μm were used. These dimensions were chosen to retain the same aspect ratio as the 1 mm x 0.6 mm x 1.6 mm hinges investigated in Chapter 3, constrained to the 300 μm thickness of the silicon wafer.

A micro magnet (500 μm x 500 μm x 200 μm powder pressed N50 neodymium) was embedded such that the distance from the top edge of moving link to the center of mass of the magnet, l_m in figure 5.1, is equal to 638 μm. This distance was determined by the size of the hinge's anchor geometry, the size of the magnet, and manufacturing constraints. The distance $l_m + l_h/2$ is effectively the moment arm of the local x-

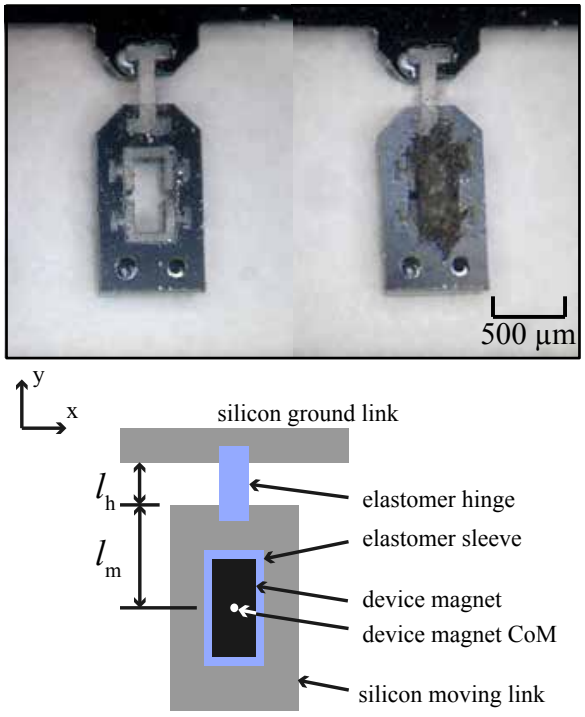

Figure 5.1: Single-hinge micro mechanism. Left: without embedded magnet. Right: with embedded magnet. Below: A schematic of the mechanism.

component of the forces on the embedded magnet. These forces are determined by the actuation principle.

5.1.2 Actuation principle

The principle behind the magnetic actuation of the single link hinge is in the interaction between two magnets, a strong, external "actator magnet," and a weaker "device magnet" embedded in the mechanism itself. Note that there can be multiple device magnets in one mechanism driven by a single actuator magnet, but each should be paired with the actuator magnet separately—the interactions between device magnets are not considered here. The actuator magnet generates a field which induces a torque and a force on the device magnet, which is then transferred to the mechanism.

A general model for determining the forces and torques on the device magnet for a given actuator magnet configuration was developed by Mahoney et. al. [52]. This model (Figure 5.2) uses the point-dipole model, which treats both magnets as a single point in 3D space, located at the center of mass of each magnet respectively. Located at these points are the associated magnetic dipole vectors, $\vec{m}_a$ for the actuator magnet and $\vec{m}_d$ for the device magnet. The magnitude of the dipole vector is dependent on the magnet material, manufacturing, and magnet volume, and can be estimated using material properties or determined experimentally. The dipole vector direction is dependent on the magnet's poling direction and current orientation. The distance

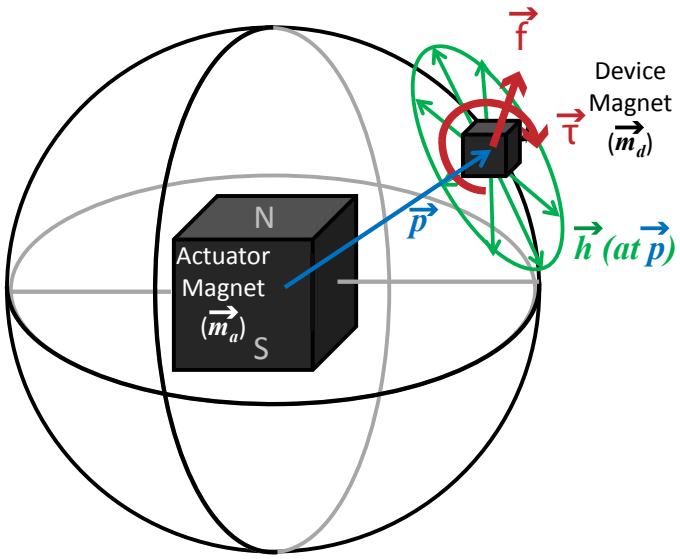

Figure 5.2: General form of the model for magnetic actuation.

vector from the actuator magnet to the to the device magnet is denoted as $\vec{p}$.

For a given configuration of these three parameters — $\vec{m_a}$, $\vec{m_d}$, and $\vec{p}$ — a torque vector, $\vec{\tau}$, and force vector, $\vec{f}$ will be generated at the center of mass of the device magnet. These vectors, derived by Mahoney et. al. in [52], are given by:

$$\vec{\tau} = \mu_0 \vec{m_d} \times \vec{h} \tag{5.1}$$

$$\vec{f} = \frac{3\mu_0}{4\pi ||\vec{p}||^4} (\hat{p}\vec{m_d}^{\mathsf{T}} + \vec{m_d}\hat{p}^{\mathsf{T}} + (\vec{m_d}^{\mathsf{T}}\hat{p})\mathbf{Z})\vec{m_a} \tag{5.2}$$

The matrix $\mathbf{Z} = \mathbf{I} - 5\hat{p}\hat{p}^{\mathsf{T}}$. The magnetic permeability of free space is $\mu_0 = 4\pi \times 10^{-7}$ N-A^{-2}. The magnetic field vector, $\vec{h}$, at the device magnet is:

$$\vec{h} = \frac{1}{4\pi ||\vec{p}||^3} \mathbf{H}\vec{m_a} \tag{5.3}$$

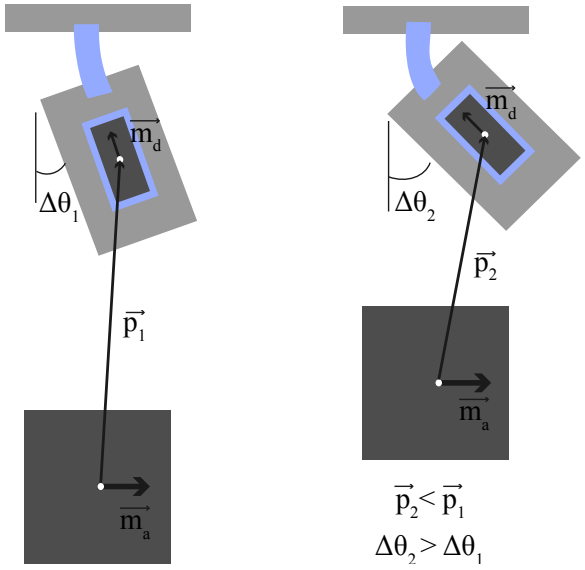

Figure 5.3: Actuation principle of the micro mechanism.

The matrix $\mathbf{H} = 3\hat{p}\hat{p}^{\mathsf{T}} - \mathbf{I}$. This general model provides the forces and torques on the device magnet in 3D space for any configuration of device and actuator magnet. For the investigation of a single link mechanism, only in-plane actuation has been considered, applied by an actuator magnet with no offset in the z-direction (out of plane). Thus, only the x and y components of force are considered, and only the z-component of torque is considered.

A view of this simplified in-plane motion used for the single-link mechanism is pictured in Figure 5.3, illustrating the deflection of the elastomer hinge with increasing force and torque as the magnitude of $\vec{p}$ decreases.

This actuation principle can be used to statically move the single link mechanism to a desired angular deflection or to dynamically excite the mechanism at a wide range of frequencies below the so-called step-out frequency. The step-out frequency is the

theoretical frequency where, due to the damping properties of the actuated system, the device magnet is no longer able to keep up with the actuating frequency of the actuator magnet. This frequency, ω_{s-o}, is defined by [52]:

$$\omega_{s-o} = \frac{\tau_{max}}{C} \tag{5.4}$$

Here, τ_{max} is the torque on the device magnet generated by the actuator magnet at an orientation offset of 90°. C is the damping coefficient of the actuated system. This number will change with the distance $\vec{p}$, and with the properties of the mechanism being actuated.

Before the actuated mechanism can be characterized, however, properties of the hinge itself must be identified.

5.2 Experimental characterization of elastomeric micro-hinges

The properties of Sylgard 184 PDMS have been investigated as part of microfabricated structures previously, and were found to be highly dependent on the processing steps taken [49]. This previous work determined stress-strain curves for PDMS samples fabricated in an SOI-wafer process. The processing steps taken in the current work are different given that they are fabricated in a through-wafer process on a silicon wafer. Hinges and mechanisms from the same wafer were used to both investigate the static and dynamic properties of the fabricated hinge as well as investigate the magnetic actuation principle described above. This was done to ensure

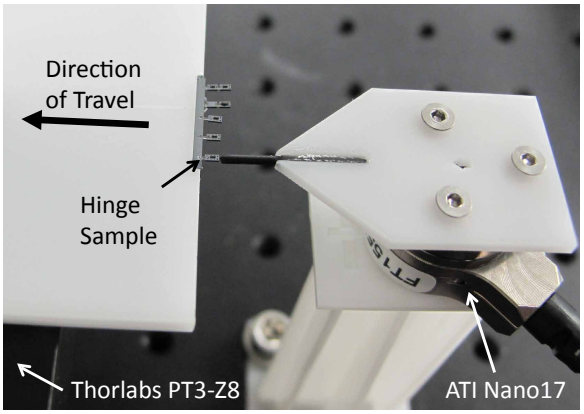

Figure 5.4: Experimental setup for material stress-strain measurements.

that accurate material properties were used during the modeling of the mechanism.

5.2.1 Material stress-strain characterization

Two samples were used to characterize the stress-strain response of the elastomeric hinge material. The samples measured 300 μm x 150 μm x 300 μm and 400 μm x 100 μm x 300 μm respectively. The samples were affixed on one end to a Thorlabs PT3-Z8 3-axis motorized translational stage and on the other end to a beam rigidly attached to an ATI Nano17 six-axis force/torque sensor (Figure 5.4).

The stage was then moved in increments of 0.01 mm along the long axis of the sample such that the sample is put in a state of increasing tension. After a distance of 300 μm (sample 1) or 400 μm (sample 2) was reached, the direction of travel was reversed and the displacement was brought back to 0. Based on previous experience modeling elastomeric hinges in tension, as well as visual inspection of the hinges during testing showing delamination of the anchor geometry, the length of

the anchor geometry was included in the strain calculations. This length adds an additional 200 μm, resulting in an effective length of 500 μm for sample 1 and 600 μm for sample 2. These displacements result in a maximum engineering strain of 60 and 66% respectively for each sample.

At each point, the axial force was recorded using the ATI sensor, and converted to engineering stress by dividing the measured force by the unstressed cross section. Eleven trials were taken for sample 1, and 3 trials for sample 2, though the first trial for each sample was not included here due to excessive hysteresis present in the initial cycle compared to further tests.

Two material models were fit to this collected stress-strain data (Figure 5.5). The first is a simple linear elastic model of the form

$$\sigma = E\epsilon \tag{5.5}$$

The engineering stress, σ is linearly related to the strain, ϵ, by a modulus E.

The second material model is a second order Ogden model of the form

$$\sigma = \mu_1(\lambda^{(\alpha_1-1)} - \lambda^{(-\frac{1}{2}\alpha_1-1)}) + \mu_2(\lambda^{(\alpha_2-1)} - \lambda^{(-\frac{1}{2}\alpha_2-1)}) \tag{5.6}$$

In this model, the engineering stress, σ is related to the stretch ratio, $\lambda = 1 + \epsilon$, by four parameters, μ_1, α_1, μ_2, and α_2 [53]. This model was chosen for comparison because it was the best material model fit in the previous work by Gerratt [49]; it

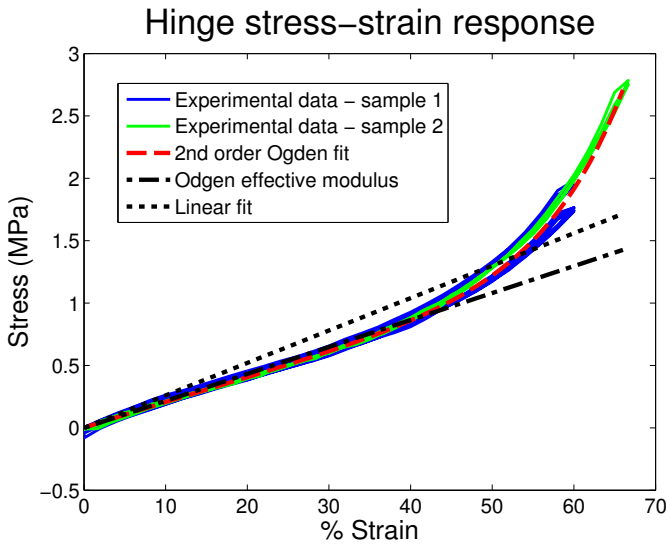

Figure 5.5: Experimental characterization of stress strain response with Ogden and linear models.

allows for increased stress at large strains as seen in the experimental data. Although these parameters were fit to the stretch ratio, for convenience the curve is plotted against strain along with the rest of the data.

The curve-fit parameters for both material models are reported in Table 5.1. An equivalent Young's modulus can be determined from the nonlinear Ogden model as defined in [53] and below.

$$E_{Ogden} = (1 + \nu) \sum_{i=1}^{2} \mu_i \alpha_i \tag{5.7}$$

Assuming a Poisson's ratio $\nu = 0.5$, $E_{Ogden} = 2.16MPa$; this is comparable to the modulus from the linear Hooke model. The somewhat high elastic modulus is likely due to the material experiencing relatively high temperatures (150 °C) during

Table 5.1: Fit parameters for material models

Linear elastic model	2nd order Ogden model				
E_{Hooke} (MPa)	μ_1 (MPa)	α_1 (MPa)	μ_2	α_2	E_{Ogden} (MPa)
2.6	1.05×10^{-4}	19.6	0.397	3.62	2.16

the second oxide deposition step of the fabrication process, and is consistent with the reported modulus of Sylgard 184 PDMS cured at this temperature [54].

5.2.2 Material dynamic properties

To ensure that the normal-use frequency range for dynamic actuation of the microfabricated mechanisms is below the expected step-out frequency for a given configuration, the damping characteristics of the fabricated PDMS hinges were investigated.

A single hinge mechanism of the dimensions described in Section 5.1 was taken to an an angle of deflection at the hinge's physical limits using tweezer tips. It was then allowed to ring down to its resting state, and the angle was tracked over this ring down period using AB Motion Systems TEMA motion tracking software. The hinge was modeled as a rotational harmonic oscillator with an equation of motion of the form:

$$\tau(t) = I_r \frac{d^2\theta}{dt^2} + C\frac{d\theta}{dt} + \kappa\theta \tag{5.8}$$

Here, I_r is the rotational moment of inertia of the system, C is the damping

coefficient, and κ is the stiffness of the rotational spring. $I_r = mr^2$ where m is the mass of the system and r is the distance from the hinge center of rotation to the center of mass of the link. This assumes a point-mass model which is an approximation in this case since the mass is more distributed throughout the mechanism structure. Similarly to the psuedo rigid-body model, $\kappa = EI/l$, where E is the linear modulus of the hinge material, l is the length of the hinge, and $I = \frac{1}{12}bh^3$ is the cross-sectional moment of inertia, where b and h are the thickness and width of the hinge's rectangular cross section, respectively.

The solution for a rotational harmonic oscillator subject to a step input was fit to the resulting time-angle data in the form of

$$\theta(t) = \theta_0 e^{-\omega_n \zeta t} cos(\omega_d t) \tag{5.9}$$

where

$$\omega_n = \sqrt{\frac{\kappa}{2I_r}} \tag{5.10}$$

$$\omega_d = \omega_n \sqrt{1 - \zeta^2} \tag{5.11}$$

$$\zeta = \frac{C}{C_c} \tag{5.12}$$

$$C_c = 2\sqrt{\kappa I_r} \tag{5.13}$$

The parameter θ_0 is the magnitude of the initial step (here set to the height of first peak in the ring-down behavior to mitigate any complications resulting from the manually applied initial loading state, such as stretch in the joint). ω_n is the natural freqency of the system. ζ is the damping ratio. C_c is the critical damping factor.

Each of the above parameters except for C was measured (E_{Hooke} was used for the Young's modulus) or derived from measurements and design parameters. For example, the designed width, b, was 300 μm and mass, m, was calculated from the designed geometry and densities. The damping coefficient C was used as the single parameter to be determined by the fit of the curve described by Equation 5.9 to the experimental data. The parameters input to this model, the resulting damping coefficient, and each of the parameters derived from the known and fit parameters, are given in Table 5.2. The data from two step-input trials and the resulting curve fit are shown in Figure 5.6.

The determination of the damping coefficient C for this mechanism can be used to predict the step-out frequency for this configuration only. This will be discussed further in a later section. However, the damping coefficient for this mechanism was also used to calculate the damping ratio ζ for the hinge material as fabricated. This parameter can be used for determining the dynamic characteristics of any other hinges made with the same material, regardless of the hinge geometry.

Table 5.2: Known, fit, and derived parameters for a hinge step response

Known Parameters		Fit Parameter		Derived Parameters	
E (Pa)	2.60×10^{6}			κ (N-m)	4.58×10^{-7}
m (kg)	1.0×10^{-6}			I_r (kg-m^2)	5.70×10^{-13}
b (m)	300×10^{-6}	C (N-m-s)	1.45×10^{-10}	C_c (N-m-s)	1.02×10^{-9}
h (m)	113×10^{-6}			ζ	0.142
l (m)	189×10^{-6}			ω_n (rad/s)	898
θ_0 (rad)	0.615			ω_d (rad/s)	880

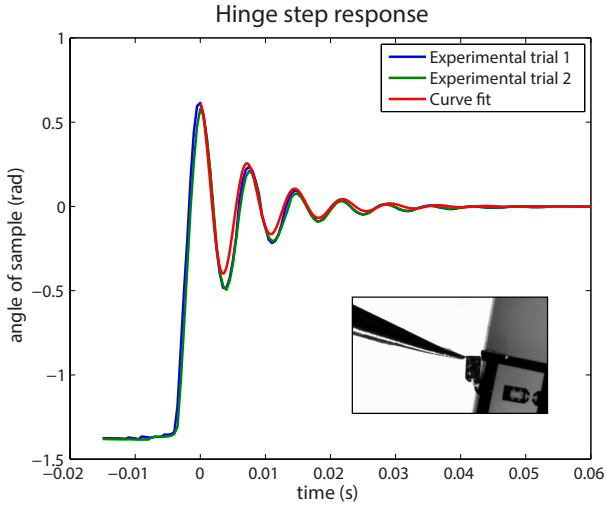

Figure 5.6: Step experimental response in a micro hinge, experimental and curve fit model. Inset: the hinge held by the tweezer, just before release.

5.3 Magnetic actuation of the micro mechanism

Once a the hinge's static and dynamic properties are known, the principle of the magnetic actuation as described above can be applied to aid in understanding the behavior of the physical mechanism. This section describes the characterization of the magnetic dipoles of the magnets used, and describes the experimental methods used for characterization of the static and dynamic actuation of the mechanism.

5.3.1 Dipole characterization

The two magnets used in this work are the actuator magnet—a 1 in^3 N52 neodymium magnet—and the device magnet—a 500 μm x 500 μm x 200 μm powder-pressed N50 neodymium magnet—both purchased from www.supermagnetman.com. In order to use these magnets in the force/torque model described in Section 5.1, the magnitude and direction of the dipole of both magnets must be known.

The poling direction can be found by aligning the magnets in a magnetic field of a known direction. The dipoles are assumed to be square to the geometry of the magnets in this work.

The dipole magnitude can be estimated using the residual flux density of the magnetic material multiplied by the volume of the magnet. The residual flux density for N50 and N52 strength neodymium is reported at 1.12-1.15$\times 10^6$ A/m and 1.15-1.18$\times 10^6$ A/m respectively [55]. Based on these numbers, the estimated dipole magni-

tudes are expected to be $|\vec{m_a}| = 20.2-20.7A-m^2$ and $|\vec{m_d}| = 56.0-57.5\times10^{-6}A-m^2$.

One approach to experimentally determine the magnet dipole was provided in [52]. However, this approach was found to be insufficient to measure the dipole of the device magnet given its small magnetic field. Instead, to verify these estimates, the dipoles of both magnets were experimentally measured by placing the magnet at a 90°-offset orientation in a known field at the end of a known spring and measuring the resulting torque (Figure 5.7). The resulting dipole magnitude will be given by $|\vec{m}| = \tau/|\vec{B}|$. For both cases, the known field was applied via a Helmholtz coil setup (R= 60 mm, N = 50 turns of 22 gage enameled magnetic wire), built in-house by Ryan St. Pierre and characterized using a using an AD22151 magnetic field sensor chip. For the actuator magnet, the ATI Nano17 sensor was used to measure the resulting torque. However, the device magnet dipole is too small to produce a torque measurable by this sensor, so the deflection of a tungsten wire of known properties was used to measure the resulting torque for the device magnet.

For the experimental characterization of the actuator magnet, a field of 1.1 mT was applied, and a resulting torque of $\tau = 20.4 \times 10^{-3}$ N-m. was measured directly from the ATI sensor. The actuator magnet was rigidly attached to this sensor using a 3D printed fixture. The resulting dipole magnitude was calculated to be $|\vec{m_a}| = 18.6A - m^2$.

For the experimental characterization of the device magnet, a field of 3.75 mT was applied. The magnet was affixed to the end of a 26.4 mm long, circular cross-

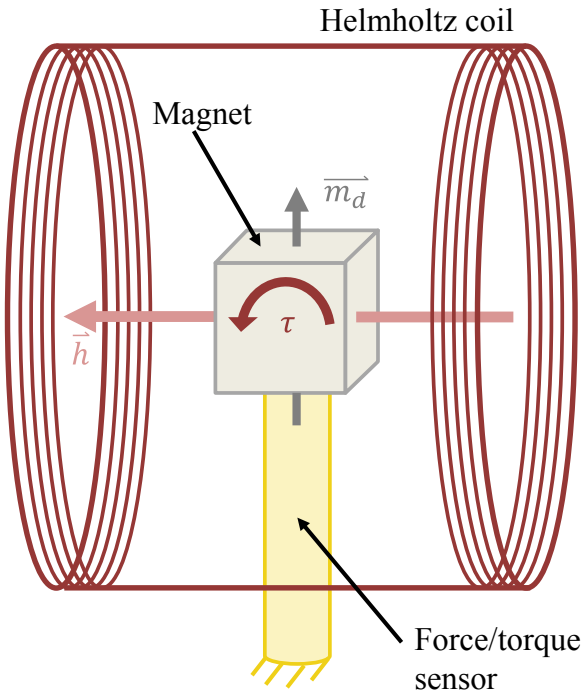

Figure 5.7: Dipole characterization sketch.

section (r = 16.6 μm) tungsten wire (E=411 GPa). The resulting torque was determined using a simple beam-bending equation, $\tau = 2EI\delta/l^2$, where E is the elastic modulus, l is the length of the wire, δ is the deflection, and I = $\frac{\pi}{4}r^4$ is the cross-sectional moment of inertia, where r is the radius of the wire. The deflection δ was measured using TEMA, at $\delta = 1.89$ mm. Because $\delta < l/10$, the rotation of the magnet sample is assumed to be negligible, and the 90° orientation offset remains valid over the full deflection of the beam—meaning the final torque is not significantly reduced from the initial torque, and a single number can be extracted from the test. This resulting torque was found to be $\tau = 1.30 \times 10^{-7}$ N-m. The dipole magnitude for the device magnet was then calculated to be $|\vec{m}_d| = 34.6 \times 10^{-6} A - m^2$.

The experimental values for the dipoles of both magnets are lower than the estimated values by about 10% for the actuator magnet and by up to 40% for the device magnets. The difference may be due to imperfect poling of the material, manufacturing inconsistencies, etc. In particular, the micro magnets used for the device magnets were observed to vary in size by up to about 10 μm in any direction, resulting in a variance in volume of 10-20%. This makes precise modeling challenging, but useful design insights can still be derived from these models if these tolerances are kept in mind.

For the characterization and modeling in the reminder of this work, the experimentally determined dipole magnitudes of $|\vec{m}_a| = 18.6\ A-m^2$ and $|\vec{m}_d| = 34.6 \times 10^{-6}\ A-m^2$ will be used .

5.3.2 Setup for characterization testing

For the characterization of static actuation of the single-link mechanism, the actuator magnet was mounted on a Newport M-RS40 rotation stage, which is then mounted to a Zaber A-LSQ450D-E01 motorized linear stage. The mechanism with the embedded device magnet is mounted to a stationary platform, with the mechanism centered with respect to the x-axis (Figure 5.8). The linear stage can then be moved to vary distance between the magnet centers of mass, $\vec{p}$, in the y-direction direction only, while keeping the x- and z-offsets at 0. Alternatively, the y-offset can be kept stationary, and the angular orientation of the actuator magnet dipole, $\vec{m}_a$ can

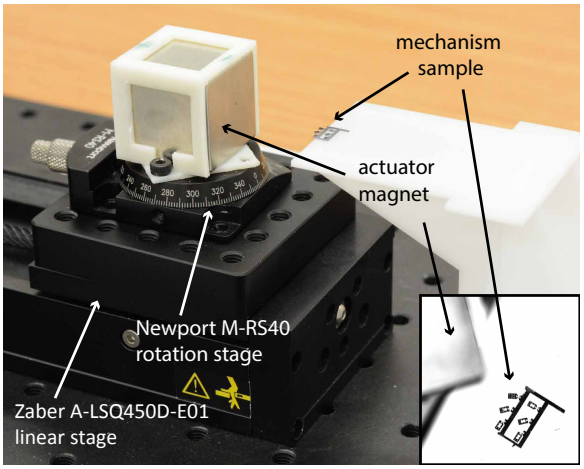

Figure 5.8: Experimental test setup for characterization of the micro mechanism using magnetic actuation. Inset: close-up of the mechanism sample with a rotated actuator magnet.

be varied in the x-y plane, while keeping the z-component at 0. Because the mechanisms were not observed undergoing significant out-of-plane motion during testing, the assumption of a negligible z-component is supported.

To characterize the magnetic actuation of a single-link hinge, the angle of deflection was varied by keeping $\vec{m_a}$ at a constant 90° offset from the orientation of the undeformed orientation of the device magnet, and varying $\vec{p}$ from 22-122 mm through the movement of the linear stage in increments of 5 mm. A second test was also performed, keeping the actuator magnet at a constant distance $\vec{p} = 22$ mm and varying the angle of $\vec{m_a}$ between 0 and 95◦ relative to the angle of $\vec{m_a}$ as it is oriented in the undeformed hinge. The deformed hinge is then captured photographically using a Nikon D7100 Camera equipped with a Zeiss Makro-Planar T* 2/100 mm ZF.2 Macro Lens, and the angle of deflection, $\Delta\theta$ is measured using TEMA.

For the characterization of the dynamic actuation of a single-link mechanism, a different setup was used. This setup, pictured in Figure 5.9, consists of an actuator magnet mounted to a Maxon EC22 100W #386677 brushless sensorless motor. The single-link mechanism is mounted to a stationary platform so that the mechanism is in line with the axis of rotation of the actuator magnet. The distance $|\vec{p}|$ for this test setup is fixed at 62 mm. As the actuator magnet rotates, the single-link mechanism will actuate at the frequency of the actuator magnet rotation, provided that frequency is under the step-out frequency of the system. The amplitude of the deflection will vary with the frequency of actuation. Experimentally, the frequency was varied from 100-1570 rad/s, and the "envelope" of the maximum and minimum deflection angle at the frequency sweep was continuously captured using the Nikon camera and macro lens setup, filming in real time. TEMA was used to capture the envelope by measuring the exterior angles of the motion blur.

5.4 Modeling and Analysis

The data taken from the test setups described in the previous section is presented here, along with initial modeling and analysis.

5.4.1 Bending testing

In addition to the experimental deflection data described in the previous section, a simple 1-spring pseudo rigid-body model is proposed to predict the motion of

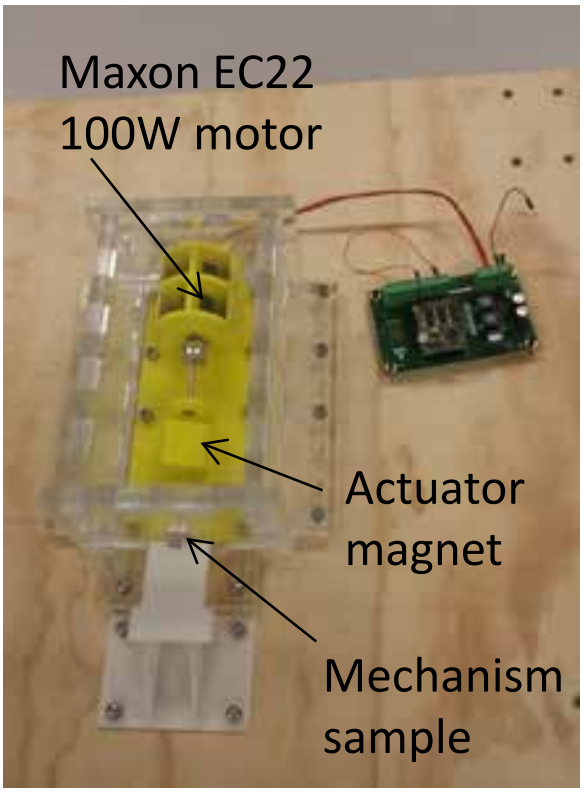

Figure 5.9: Experimental setup for high speed testing of the micro mechanism.

the single-link hinge undergoing in-plane bending displacements due to magnetic actuation. This model was chosen due to the relatively high stiffness the hinges display in tension, and the comparatively low force components under the included loading conditions.

The spring constant for the elastomer hinge is determined using equation 3.7, as outlined in Chapter 3. The parameters for this model are the hinge dimensions given in section 5.1. Equations 5.1 and 5.2 determine the torque and force on the device magnet for a given relative position vector $\vec{p}$ and orientation of $\vec{m_a}$ relative to the undeformed orientation of $\vec{m_d}$, θ_a. (Note that $\vec{p}$ changes with increased deflection, but for convenience later in this chapter, values have been plotted against a value of $\vec{p}$ rounded to the nearest mm. Also note that θ_a is not used in any calculations, but is a convenience for denoting the current angle of the actuator magnet without considering the instantaneous angle of the device magnet).

The force and torque are applied at the location of the device magnet center of mass, and the resulting deflected distance, $\Delta\theta$, is recorded for each step (Figure 5.10). However, due to the nature of the load condition applied by a magnetic field, there were some differences in the method used to find the resulting $\Delta\theta$, when compared to a direct application of a load condition. An algorithm for finding this value is discussed in the following paragraphs.

For simplification of this discussion, we will assume a pure, single-axis torque, though the concept applies to the generated forces as well. For a fixed actuator

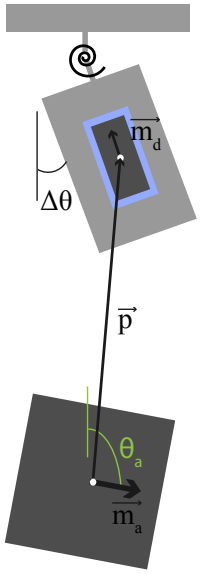

Figure 5.10: Schematic defining $\Delta\theta$ for the mechanism using the pseudo rigid-body model for a given distance between magnets, $\vec{p}$, actuator magnet dipole, $\vec{m_a}$, and device magnet dipole, $\vec{m_d}$.

magnet position and dipole vector $\vec{m_a}$, the torque on the device magnet, τ, varies with $\vec{m_d}$ and the change in $\vec{p}$ as the hinge deflects. As the magnitude of $\vec{m_d}$ is also fixed, τ is dependent on the instantaneous position and angle of the device magnet. I.e. the location and orientation of $\vec{m_d}$. Because the device magnet is embedded in the moving link, this instantaneous angle and position of $\vec{m_d}$ changes along with the instantaneous angle of the moving link, $\Delta\theta_{inst}$. In the physical system, this results in a torque being maintained in equilibrium at the end of the actuation step, (τ_f), that is lower than the torque was initially applied, (τ_i), for a constant actuator magnet position and orientation. Thus, if the initial τ_i were applied for a given actuator magnet location, and the deflection were found for this torque and accepted as $\Delta\theta$, the model would greatly overpredict the actual deflection at each actuator magnet

position or orientation.

One way to handle this is to introduce time steps to the model and incrementally reevaluate τ at each step until some equilibrium is reached. However, this is not practical for some modeling methods where the load is difficult to change during the course of the simulation, so a different approach was taken here to find a working algorithm that is robust to different modeling platforms.

The restoring torque of the hinge spring at a given $\Delta\theta$ should be equal to the torque calculated from Equation 5.1 when $\vec{m}_d$ is rotated that same $\Delta\theta$. This torque is defined as the final torque, τ_f. However, this torque is difficult to find analytically due to the nonlinear relationships with $\Delta\theta$. Initial investigation of an algorithm to find τ_f found that overshooting the value (e.g. by applying τ_i directly and attempting to "bounce down" to τ_f) can cause the model to get stuck "bouncing" between two values without ever converging. So, an algorithm was developed to find τ_f without overshooting it (Figure 5.11). The algorithm is as follows.

Set a parameter $\Delta\theta_{sum}$ initially equal to zero (Figure 5.11-A). This parameter will be incrementally increased at each step until it reaches an equilibrium point, which will be the final $\Delta\theta$.

For step n,

1. Calculate the torque on the device magnet, τ_n, at a deflection angle of $\Delta\theta_{sum}$ ($\Delta\theta_{sum}$ is determined by the results of previous steps) (Figure 5.11-B1).

2. Calculate the deflection in the hinge, $\Delta\theta_n$, resulting from τ_n. (Figure 5.11-B2)

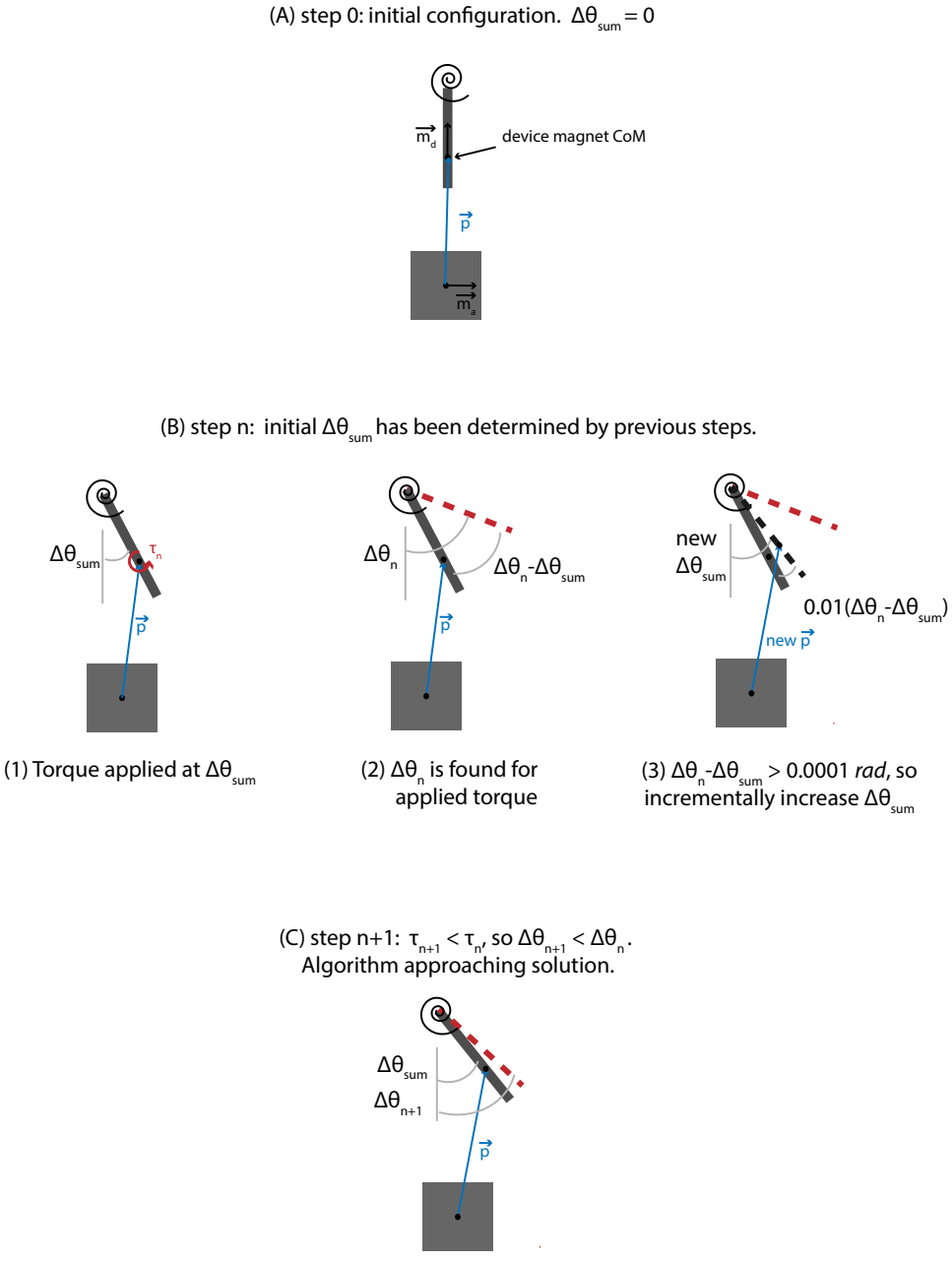

Figure 5.11: Schematic visualization of the algorithm to find $\Delta\theta$ for a given actuator position. (A) Step 0 initial configuration. (B) Step n. (C) Step n+1 final configuration. Some angles have been exaggerated for readability.

3. Is $\Delta\theta_n$ equal to $\Delta\theta_{sum}$? (Check $\Delta\theta_n$-$\Delta\theta_{sum} < 0.0001\ rad$) (Figure 5.11-C1)

4a. If yes, the the torques are balanced, stop. $\Delta\theta_n = \Delta\theta$

4b. If no, add 1% of ($\Delta\theta_n$ - $\Delta\theta_{sum}$) to $\Delta\theta_{sum}$. (Figure 5.11-C1) Repeat from 1 for step n+1 (Figure 5.11-D).

The total deflection, $\Delta\theta_{sum}$, increases incrementally with each step, while $\Delta\theta_n$ decreases with each step due to the changing position and orientation of $\vec{m}_d$. These angles will eventually converge without ever overshooting one another. At the point where these two values are equal, the final equilibrium torque, τ_f has been reached, and the final $\Delta\theta$ has been determined. The check value (0.0001 rad) and the percentage (1%) of ($\Delta\theta_n$ - $\Delta\theta_{sum}$) added to $\Delta\theta_{sum}$ with each step can be adjusted for higher accuracy or lower computation time.

A Matlab script was written to carry out this algorithm on the pseudo rigid-body model of the single-link mechanism. The experimental data for the constant-angle, variable-position test and the results of this model are displayed in Figure 5.12. The experimental data and model results for the constant-position, variable-angle test are displaying in Figure 5.13.

Two error metrics were used to look at the accuracy of the model across the two trials for both actuation methods. The models used were the mean percentage error (MPE) and root mean square error (RMSE). The MPE gives the average +/- percentage difference across every data point and is given in units of %, while the MPE gives the average absolute value of the difference across every data point and is

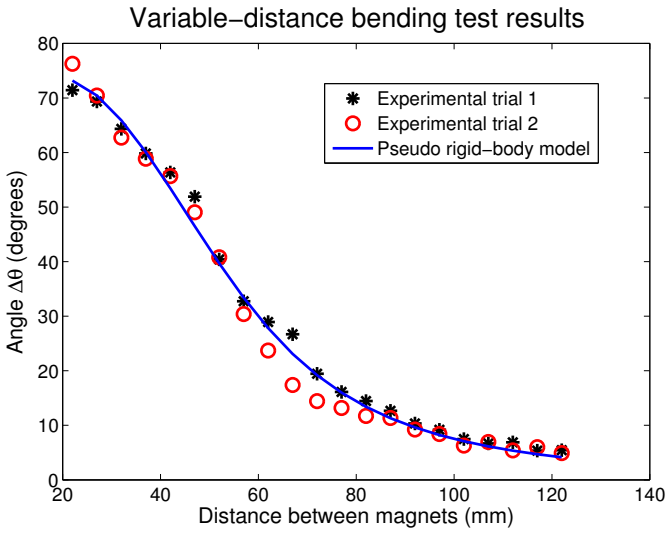

Figure 5.12: Experimental data and PRB model for change in angle, $\Delta\theta$, with distance between magnets, $|\vec{p}|$.

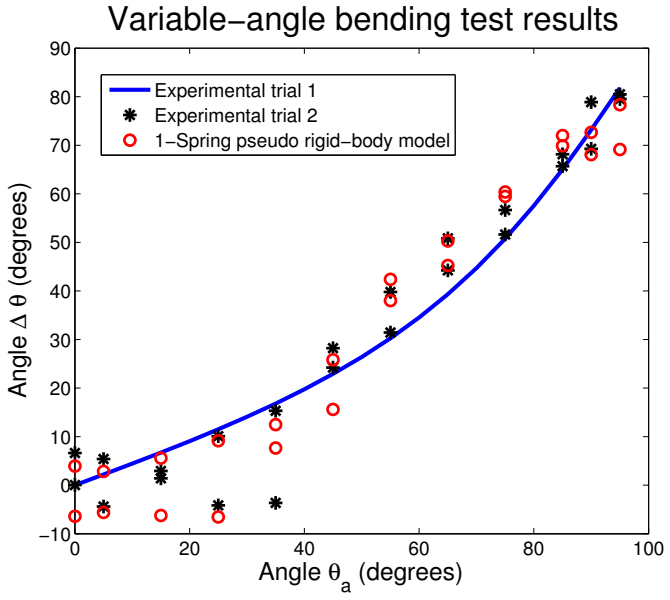

Figure 5.13: Experimental data and PRB model for change in angle, $\Delta\theta$, with actuator magnet angle relative to undeformed device magnet angle, θ_a.

given in units of degrees for these tests. These are defined as [56]:

$$E_{MP} = \frac{100}{N} \sum_{n=1}^{N} \frac{(Y_n - M_n)}{Y_n} \tag{5.14}$$

$$E_{RMS} = \sqrt{\frac{1}{N} \sum_{n=1}^{N} (Y_n - M_n)^2} \tag{5.15}$$

Here, N is the number of data points being compared, Y_n is the experimental value at a point n, and M_n is the corresponding value in the model.

For the constant-angle, variable-position test, the model shows a quite good fit to the data, with an MPE across both trials of 1.16% and an RMSE value of 2.2°. Additionally, it does not show any obvious problems that would indicate a poorly-performing algorithm, such as values of $\Delta\theta$ lower than 0° (the theoretical minimum, when $|\vec{p}|$ is very large), or higher than 90° (the theoretical maximum, when $|\vec{p}|$ is very small and $\theta_a = 90°$).

For the constant-position, variable angle test, the model is also a generally good fit to the general behavior of the hinge, although the MPE is somewhat higher at 33.7%, with an RMSE of 7.6 °. These higher errors are possibly in part due to a larger spread of experimental values. For this model, it is expected that the angle $\Delta\theta$ will be exactly 0° at $\theta_a = 0$, and that there is no asymptotically-approached maximum value at high θ_a. Instead, there will be a sharp cutoff point due to the mechanical limitations of the moving link running into the ground link. This mechanical stopping

point was not reached by the experimental data under these test conditions and was not included in the model. Qualitatively, the model performs as expected under both conditions.

These tests show that a single hinge can be moved over a wide range of angular deflections using both actuation methods. Even at a distance of several centimeters, angular deflections of 20-30 ° can be achieved. Because this single spring PRB model matches well under both variable-position and variable-angle conditions, it appears to be a good fit for the mechanism and could be used to predict its behavior under a wide variety of arbitrary in-plane actuator magnet configurations.

5.4.2 Dynamic testing

The setup for dynamic testing described in the previous section produced the results shown in Figure 5.14. To obtain this data, video of the hinge was processed to display the motion blur on a real-time video of the link with the background removed. Single points at lower frequencies (100 rad/s and 295 rad/s) were taken individually, and between 410-1570 rad/s continuous data was obtained using TEMA motion tracking software (Figure 5.15). Due to this method, the continuous data is particularly noisy. To more easily see the trends in the data, a 50-point moving average filter was applied and overlaid on this portion of the the raw data.

At low frequencies, it is expected that the deflection of the hinge in both directions will be close to the static deflection of the hinge under otherwise identical

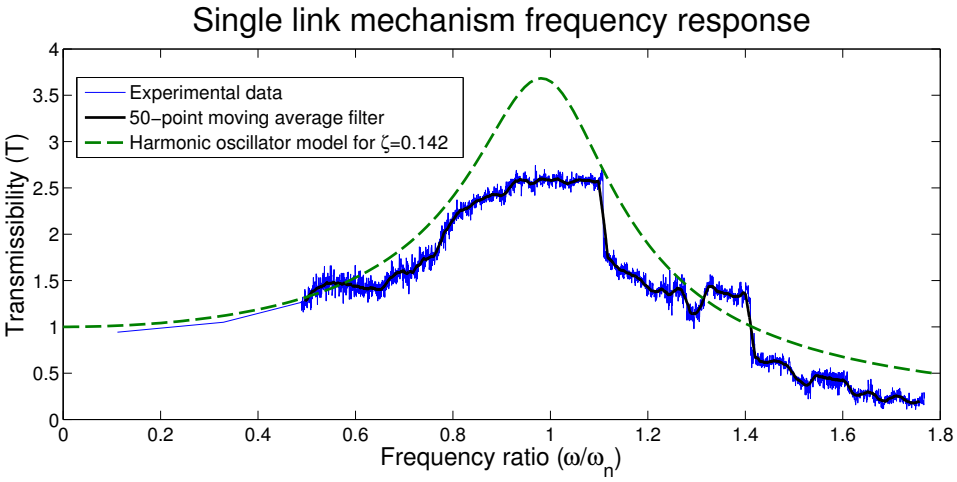

Figure 5.14: Frequency response in the single link hinge mechanism.

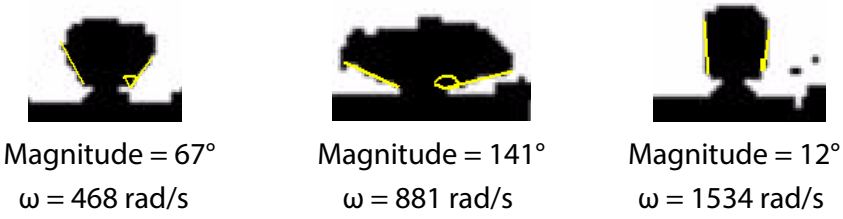

Figure 5.15: Three frames from processed video showing the hinge in three stages: low frequency, near the natural frequency, and well above the natural frequency. The yellow angle measurements were applied by the motion tracking software.

conditions. So the relatively flat, low-frequency portion of the response plot should be a value roughly twice the static deflection of the hinge at a distance $|\vec{p}| = 62$ mm. From the pseudo rigid-body model at this distance, the static deflection at this point is estimated to be 27°, which can be seen in Figure 5.12. The amplitude measured at the lowest frequency, 100 rad/s, was 51°, which is in good agreement with the expected 54°, with an error of 5.5%.

The natural frequency was estimated using the point-mass model in a previous section as $\omega_n = 898$ rad/s, and the damping ratio was determined to be $\zeta = 0.142$ (see Table 5.1). These properties were used to obtain the frequency response model shown in Figure 5.14, using the following equation [57]:

$$T = \sqrt{\frac{1 + (2\zeta\frac{\omega}{\omega_n})^2}{(1 - (\frac{\omega}{\omega_n})^2)^2 + (2\zeta\frac{\omega}{\omega_n})^2}} \tag{5.16}$$

To convert the experimental data to terms of transmissibility, the response data was normalized by the expected low-frequency response magnitude of 54°. Additionally, the frequency sweep was normalized by $\omega_n = 898$ rad/s.

The maximum value of the filtered amplitude data is 140°. This maximum value is found at a frequency of 879 rad/s. The expected peak value should be about 3.6 times the low-frequency value of 54°, or 194°. However, due to the mechanical limits of the system, this value is not possible. The theoretical cutoff point for this peak should be near 180°, but possibly due to the high-speed performance limits of the hinge or squeeze-film air damping at the mechanism limits, the actual value is

somewhat lower.

The location of the peak value should be found at $\omega_{peak} = \omega_0\sqrt{1-2\zeta^2}$, which is calculated to be 879 rad/s. The peak frequency in the filtered experimental data was found at this point, however it should be noted that the magnitude is essentially constant near this point.

The increase in amplitude from a frequency ratio of about 1.3-1.4 (1160-1260 rad/s) is most likely an artifact of the test setup. From inspection of the data collection video, this appears to be a resonant mode of the test setup itself, as the audible noise from the shaking of the setup is much higher during this time than at any other point, and the surrounding samples (unactuated, with no embedded device magnets) on the chip vibrate during this time while remaining unaffected for the rest of the frequency sweep.

This plot verifies the expected behavior of a peak in amplitude near the natural frequency and a fairly sharp decline to near zero beyond this point. However, the test may not be valid if the mechanism is not actuating at the expected frequencies. Device magnet actuation frequencies different from the applied actuator magnet frequencies are expected above the step-out frequency, so the this frequency must be determined for the setup.

The distance $|\vec{p}|$ for this test setup is 62 mm, which, using the dipoles found in the previous section and equation 5.1, corresponds to a maximum torque of 4.5×10^{-7} N-m. Using equation 5.4, and the damping coefficient determined in the previous sec-

tion (C=$1.45\times10^{-10}N-m-s$), the step-out frequency for this test setup is expected to be $\omega_{s-o} = 3.1\times10^3$ rad/s. This is well above the maximum frequency tested across this sweep (1570 rad/s), and safely above the natural frequency of the system (ω_n = 898 rad/s).

Theoretically, if the tests were repeated at a longer distance, the step-out frequency will be lowered. To obtain a step-out frequency near the natural frequency or below, where it would begin to be a problem for accurate actuation, the distance $|\vec{p}|$ must be increased to 100 mm (f_{s-o} = 885 rad/s) or higher, where (as shown in Figure 5.12 the angle of deflection is barely perceptible even at low frequencies or static actuation. The step-out frequency is well above the natural frequency for normal actuation of the single-link mechanism.

5.5 Gripper

The majority of the text in this section was taken from "Magnetic Actuation of Ultra-compliant Micro Robotic Mechanisms" [39].

To demonstrate the complexity of actuated mechanisms that can be designed for the microfabrication process, as well as the capabilities of the magnetic actuation principle to actuate more complex mechanisms with a single device magnet, an underactuated compliant gripper has been fabricated, and early pick and place capabilities are demonstrated. Previous work in underactuated compliant grippers has shown the benefits of this type of design toward grasping objects of arbitrary

geometry, flexibility, and fragility [58, 59].

5.5.1 Mechanism Concept

The gripper is intended to be actuated using a combination of forces and torques generated by the actuator magnet. A schematic sketch of this mechanism is shown in Figure 5.16, along with possible movement directions of the embedded magnet. To open or close the gripper, the actuator magnet dipole must be oriented at 0 or 180° respectively with the device magnet dipole, and the field gradient must be sufficiently high create a large enough force in the device magnet to actuate the gripper. Additionally, an angular offset between the actuator and device magnets can be used to induce a torque in the mechanism at the location of the device magnet. This causes a"rolling" the gripper tips, which can be used for tilting or rolling objects in the gripper along with the tips.

Overall, the dimensions of the gripper are 4.4 mm x 3.8 mm x 0.3 mm. The gripping tips are initially 150 μm apart and the dimensions of the hinges are 150 μm x 100 μm x 300 μm, resulting in a $k_{\theta 1spr}$ of 0.233 mN-mm/rad per hinge. Because the analysis of the gripper design is somewhat more complicated than the bending mechanisms, a single-spring pseudo rigid body model of the gripper, laid out as shown in Figure 6, was used for simulation in MSC Adams to determine the passive reaction force at the gripping tips for various sized objects. For an object 500 μm wide, the gripper was found to passively provide 1.1 mN of gripping force at each tip. For

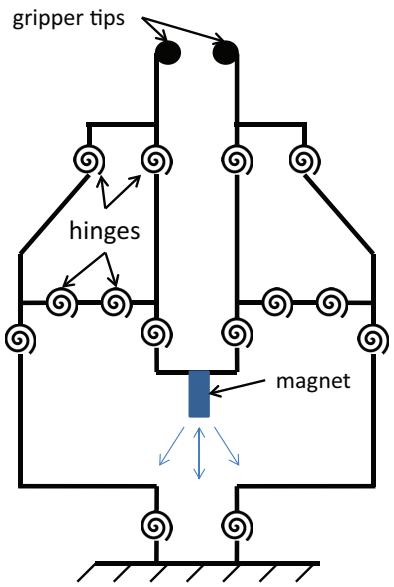

Figure 5.16: Pseudo rigid body model of the underactuated ultra-compliant micro-gripper.

an object 1000 μm wide, it passively provides 2.9 mN of gripping force on each tip. These forces can be decreased or increased by inducing a force on the device magnet using an actuator magnet in close proximity.

For comparison, an equivalent analysis was performed for a case for a gripper with silicon flexures of the same size as the PDMS flexures. The passive gripping force increases to 120 N for a 500 μm object, and 310 N for a 1000 μm object. Assuming the silicon hinges themselves do not fail, for a silicon object of dimensions 1000 μm x 500 μm x 500 μm gripped along the length, this kind of force would cause compressive stresses on the order of GPa–approaching the failure strength of silicon [60]. An identical PDMS object would buckle and likely tear.

For further comparison, a third analysis was performed for a gripper with silicon

flexures that match the stiffness of the PDMS hinges. These hinges would need to have a length of 16 m or a width of 21 nm, neither of which is realistically possible. These two examples illustrate the value of the highly flexible incorporated elastomer hinges.

5.5.2 Mechanism Performance

The gripper was able to open to up to 1.5 mm between the gripping tips and close to full contact between the gripping tips. These positions, along with the off-axis rolling behavior are shown in Figure 5.17. Using the pseudo rigid body model described above, the maximum calculated reaction force on the fully opened gripping tips was determined to be 4.9 mN on each tip.

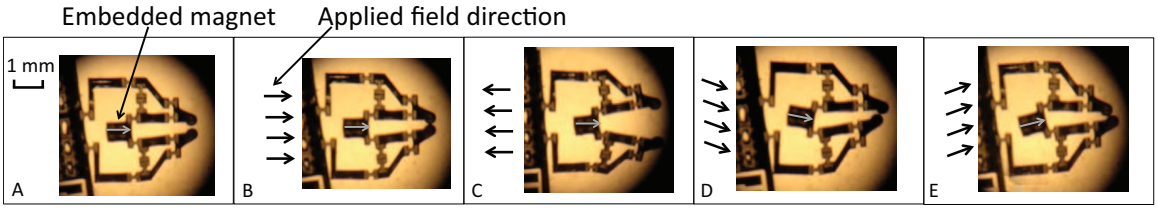

Figure 5.17: Gripper movement with different external field orientations

The gripper's highly flexible nature allows it to grip both rigid and flexible objects, as shown in Figure 5.18. The gripper first grips and moves a 1300 μm x 600 μm x 300 μm piece of silicon, then grips and stacks a 1400 μm x 700 μm x 500 μm piece of PDMS on top of it. Figure 5.19 shows the gripper gripping a 0402 package size (1.0 mm x 0.50 mm x 0.55 mm) surface mount capacitor. These capabilities demonstrate the gripper's potential utility for pick-and-place manufacturing applications.

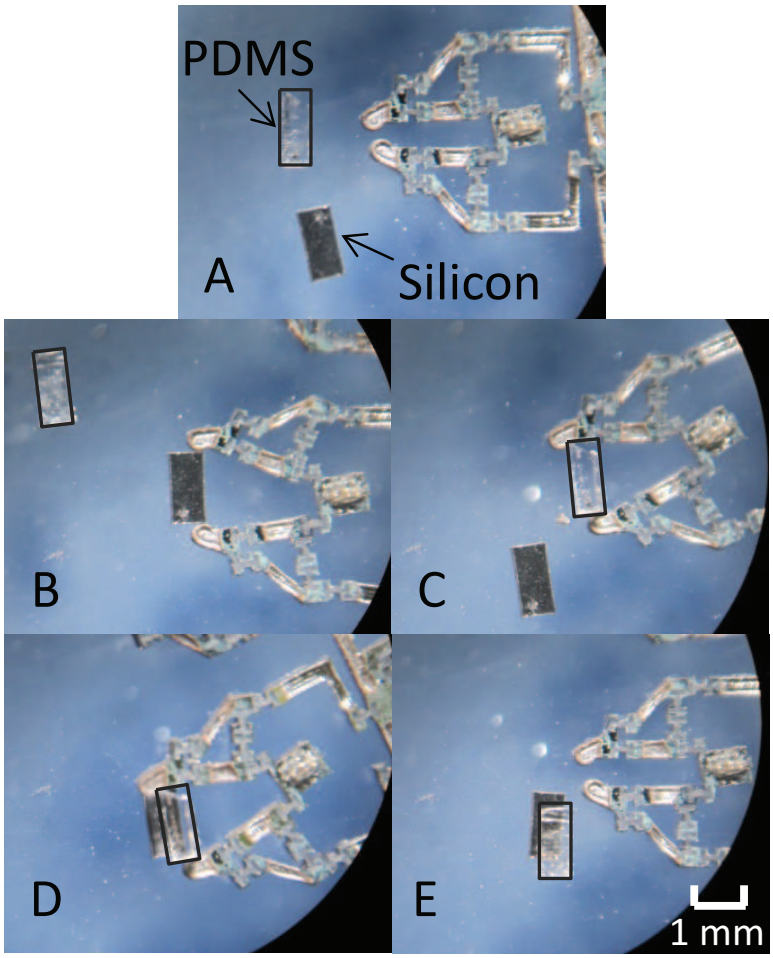

Figure 5.18: A: Gripper with PDMS and Silicon pieces. B: Gripper gripping Si piece. C: Gripper gripping PDMS piece. D: Gripper placing PDMS piece on top of Si piece. E: Gripper and Si/PDMS stack.

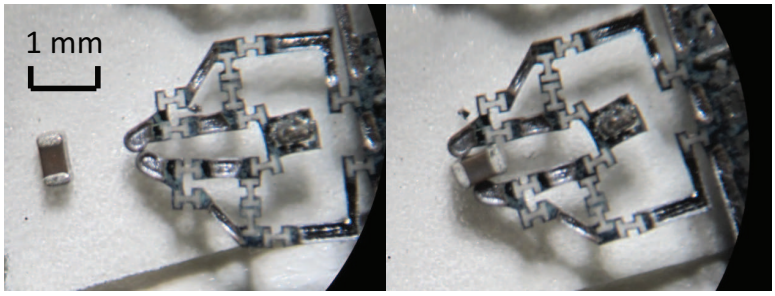

Figure 5.19: Gripper gripping surface mount capacitor.

The work in this chapter represents many steps taken toward understanding these micro-scale magnetically-actuated mechanisms. However, to achieve the desired goal of a leg design that will result in a fast, capable legged microrobot, more characterization and more complex models need to be applied. This is discussed in the following chapter.

Chapter 6

Hinge modeling for a hexapedal microrobot

The majority of the material in this section is taken from "Adaptation of a 3-spring PRB model for a magnetically actuated multi-material microrobot leg" [61].

This final chapter represents the applications of each of the previous sections directly toward the goal of microrobotic leg design. The analytical models developed in Chapter 3 are verified against physical mechanisms fabricated using the method developed in Chapter 2 and actuated using the method characterized in Chapter 5. Finally, leg mechanisms prototyped in Chapter 4 are fabricated and modeled using these techniques, and a walking hexapedal microrobot is demonstrated.

6.1 Magnetically actuated micro mechanisms

Several mechanisms are presented in this section, including 5 simple, single-link, single-hinge mechanisms of varying geometries, intended to reflect the work done on the meso-scale in Chapter 3. The remaining mechanism is a two-hinge, two-link robotic leg mechanism with one active degree of freedom, similar to the one presented in Chapter 4.

6.1.1 Single hinges

Five single-hinge, single-link mechanisms are presented here with geometry chosen to reflect a range of expected angle configurations and geometric decisions that might be made when constructing more complicated mechanisms. The five geometries include a 180° hinge, two 90 ° hinges, and two 135° hinges. The two 90° and 135° hinges are split up into curved and straight-beam geometries (Figure 6.1). The type numbers were assigned to stay consistent with the hinge samples presented in Chapter 3.

Each of the mechanisms has a single point of actuation near the center of the rigid link. The hinge geometries, as designed, are 189 μm x 113 μm x 300 μm for type 1, 295 μm x 160 μm x 300 μm for type 2, 257 μm x 113 μm x 300 μm for type 3, 359 μm x 122 μm x 300 μm for type 4, and 351 μm x 113 μm x 300 μm for type 5. For each geometry, the centerline distance is reported, and the width of the cross-section over the length of the hinge (i.e. not near the anchors). The normal distance from the top edge of the rigid link to the center of mass of the magnet is 638 μm for each geometry. This distance, l_m is shown in Figure 6.1 for geometries 1, 2, and 4. The definition is similar for geometries 3 and 5.

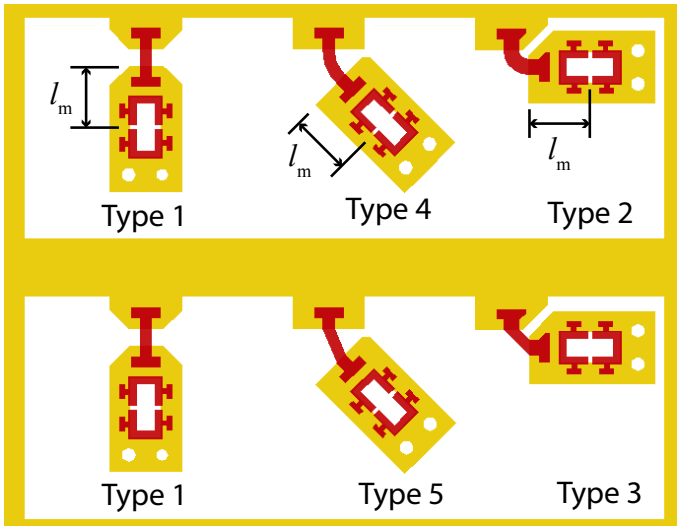

Figure 6.1: Schematic of the five geometries as fabricated. Yellow is rigid material, red is elastomeric material.

6.1.2 A microrobotic leg mechanism

The leg mechanism, pictured in Figure 6.2 consists of two links and two hinges, with a single point of actuation in the top link, resulting in a single active DOF in the hip joint and and a single passive DOF in the knee joint. Similarly to the leg already described in Chapter 4, this leg includes a "kneecap" feature and an elasomter "foot" for mechanical and frictional asymmetries to generate higher forces–and thus preferential movement in a full robot–during (real or simulated) travel in the direction of the kneecap.

The dimensions for both of the hinges are 200 μm x 100 μm x 300 μm. The dimensions of the top link are 1650 μm x 670 μm x 300 μm, and the dimensions of the bottom link are 1200 μm x 670 μm x 300 μm. The center of mass of the embedded

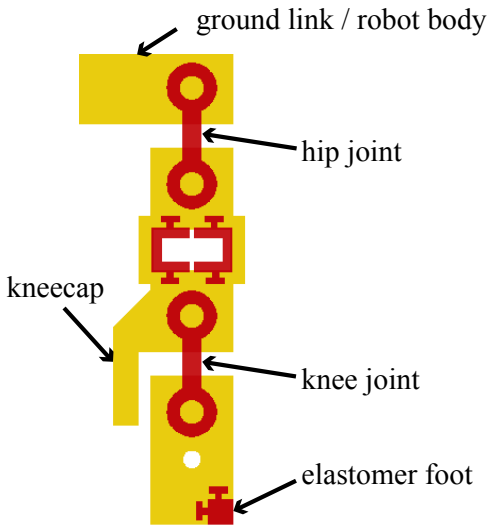

Figure 6.2: Schematic of the leg mechanism. Yellow is rigid material, red is elastomeric material.

device magnet is located halfway down link 1. The kneecap extends 600 μm from the bottom of the top length, with a resulting undeformed overlap of 400 μm between the kneecap and the lower link, with a gap of 100 μm separating the two. The foot feature measures 200 μm x 200 μm, and extends through the full 300 μm thickness of the leg.

The dimensions of this leg are not optimized, rather they were chosen to accommodate robust hinge anchor geometry, and to not push the limits of the fabrication process in order to ensure good yield. A high-yield, robust design was chosen over a high-performance design to ensure that all six legs of a full hexapod are most likely to survive, as well as to ensure adequate test samples to characterize the performance of these legs to inform design choices on future iterations of leg design.

6.2 Experimental characterization of magnetically actuated elastomeric micro-hinges

6.2.1 Bending testing

The test setup for bending tests for the five geometries was set up nearly identically to the bending test setup described in Chapter 5. The minor difference is that two geometries could be tested at the same time (sample types 2 and 3, and sample types 4 and 5), as they were fabricated in line with one another. This results in a slightly offset set of distances $|\vec{p}|$ for each sample. The step size between sampling points and total distances traveled also varied slightly.

6.2.2 Finite element hinge modeling

Finite Element Analysis (FEA) was carried out using Ansys on each of the 5 hinge geometries, with dimensions as reported in the previous section. The material models used for these analyses were a linear material model with a modulus of E=180 GPa for the silicon links, and a second-order Ogden hyperelastic model, using the values given for μ_1, μ_2, α_1, and α_2 in Chapter 5, table 5.1 for the elastomer hinges. Solid185 elements were used to mesh the geometry, with 20 μm elements used for the elastomer hinge and 40 μm elements used for the silicon features. 4000-5000 elements were used for the hinge feature depending on the mechanism type. Surf154 surface elements were applied over 4-8 elements on either side of the meshed mechanism link

to apply the torque load as a tangentially-applied force couple (applied as pressure normalized by the surface area of the surface elements) about the center of mass of the embedded device magnet.

For a more direct comparison to the performance of the other models, the same strategy for determining forces and torques resulting from magnetic actuation described in Chapter 5 was used to determine the loading conditions for the FEA models. Specifically, equations 5.1 and 5.2 were used to determine the torques and forces at the point of the center of mass of the embedded device magnet for each mechanism type for a given, decreasing distance $|\vec{p}|$.

Additionally, since it is not easy to change the loading conditions dynamically during an Ansys run, the algorithm developed to find an equilibrium position without overshooting, described in Chapter 5, Section 5.4, was used to determine the correct changes in angle for each position. This requires many loading conditions to be solved for each actuator magnet position, and so drastically increases the computation time compared to FEA done with only one loading condition, such as those carried out in Chapter 3. To save some computation time, the simulations were done in order of increasing $\Delta\theta$ and the final result from the previous actuator magnet position step was used as the initial $\Delta\theta_{sum}$ instead of starting from zero at each step. However, even with this time-saving measure, along with relaxed parameters as compared to those in the previous chapter (10% additive parameter and 0.01 rad check parameter as compared to the original 1% additive parameter and 0.0001 rad check parameter),

the time to run the simulations for one geometry type over the experimentally investigated ranges of $|\vec{p}|$ could take 2-3 full days depending on the number of steps required to converge at smaller values of $|\vec{p}|$. For FEA of more complicated magnetically actuated mechanisms, other strategies may need to be developed, or simplification of the geometry to an equivalent structure may be required to avoid prohibitive computation times.

Alternatively, simplified models with similar performance can be used, such as those presented in the following section.

6.3 Pseudo rigid body analytical hinge modeling

For each of the hinge geometries, a 1-spring and 3-spring pseudo rigid-body model was investigated.

The spring constant for each 1-spring PRB model was determined using equation 3.7 and the hinge geometries listed in the previous sections. The single spring was placed at the center of rotation of the equivalent hinge, and the torques and forces determined using equations 5.1 and 5.2 were applied at the center of mass of the embedded device magnet in the equivalent fabricated mechanism. Finally, the same algorithm described in Chapter 5, Section 5.4 was used to find an equilibrium value for $\Delta\theta$ for each step.

Each of the spring stiffnesses in the 3-spring models were determined using the equations 3.8 and 3.9 and the hinge geometries listed in the previous sections. The

equations are repeated here for convenience:

$$k_{\theta 3spr} = \frac{2EI}{l_{eff}} \tag{6.1}$$

$$k_{l3spr} = \frac{CAE}{l_{eff}} \tag{6.2}$$

where $k_{\theta 3spr}$ is the torsional spring constant, E is the elastic modulus of the joint material, I is the cross-sectional moment of inertia of the joint, l_{eff} is an effective hinge length, k_{l3spr} is the axial spring constant, C is a correction factor, and A is the cross-sectional area of the joint.

For the straight-beam type geometries, 3 and 5, the parameter l_{eff} was originally determined by equation 3.10, reproduced here for convenience: $l_{eff} = l_c + s\theta_{trap}$, where s was found to work well when defined as -0.01 mm/deg. Here, the characteristic lengths of the hinges being modeled have been reduced by an order of magnitude, from 1 mm to 100 μm. For this reason, the parameter s was scaled identically for these models, from -0.01 mm/deg to -1.0 μm/deg. The value of l_{eff} for mechanism types 2 and 4 is still defined as the centerline length of the curved hinge–distinguished from the undeformed length of the spring, l, which remains the length between the midpoints of two inwardly-facing faces of the two links (i.e. the same as the centerline lengths of the trapezoidal type hinge geometries).

The parameter C, a correction factor for the hinge anchoring geometry, was also previously defined in Chapter 3 in terms of mm. For this factor, since the multiplier

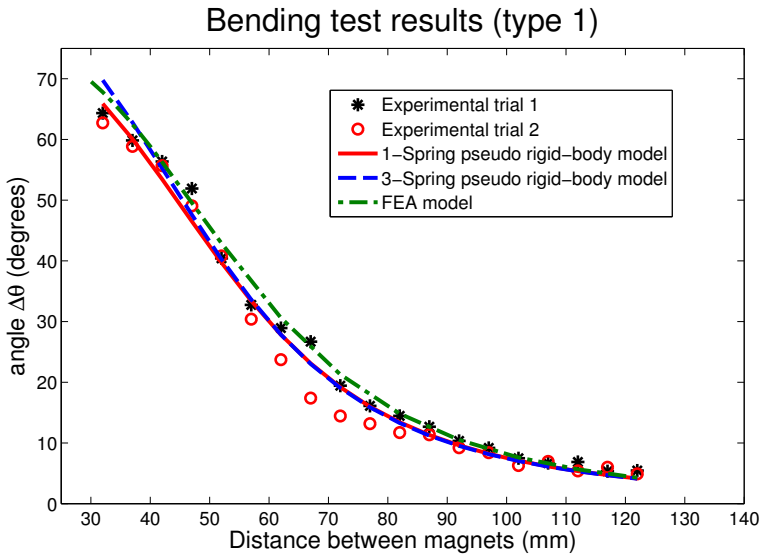

Figure 6.3: Experimental and modeling results for mechanism type 1

was originally determined for a hinge of length 1 mm, and the aspect ratios of the hinges were scaled down directly, the x-axis can be interpreted as a non-dimensional unit representing the ratio of the length of the adhesion geometry to the length of the hinge. For hinges without this scaled aspect ratio, a different curve for C may need to be found.

6.4 Single-hinge mechanism modeling results

Results for the experimental data, 1-spring PRB, 3-spring PRB, and FEA models are shown in Figures 6.3, 6.4, 6.5, 6.6, 6.7.

First, note that mechanism types 3 and 5 include two 1-spring PRB models. These represent the models with and without the corrected l_{eff}. This was done because the original 1-spring PRB model described in [25] does not include this factor.

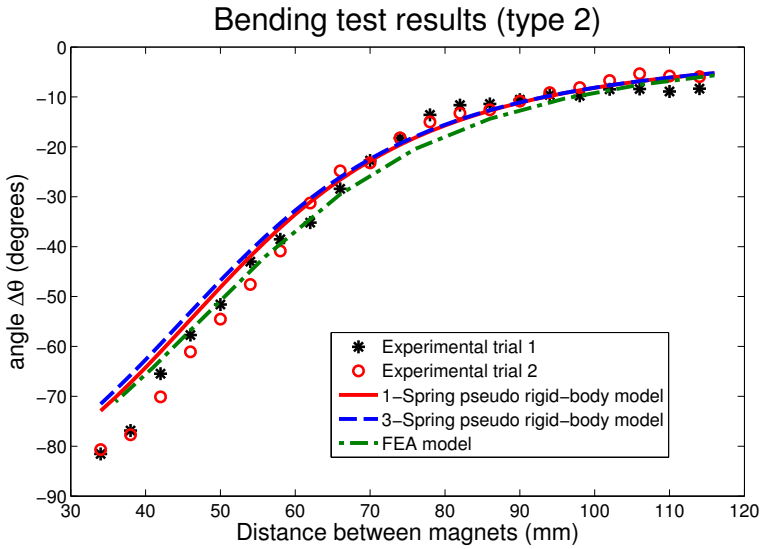

Figure 6.4: Experimental and modeling results for mechanism type 2

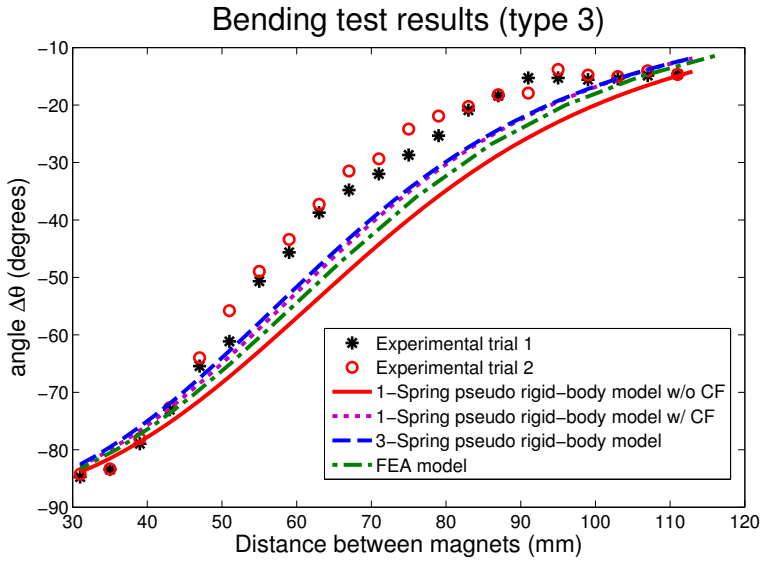

Figure 6.5: Experimental and modeling results for mechanism type 3

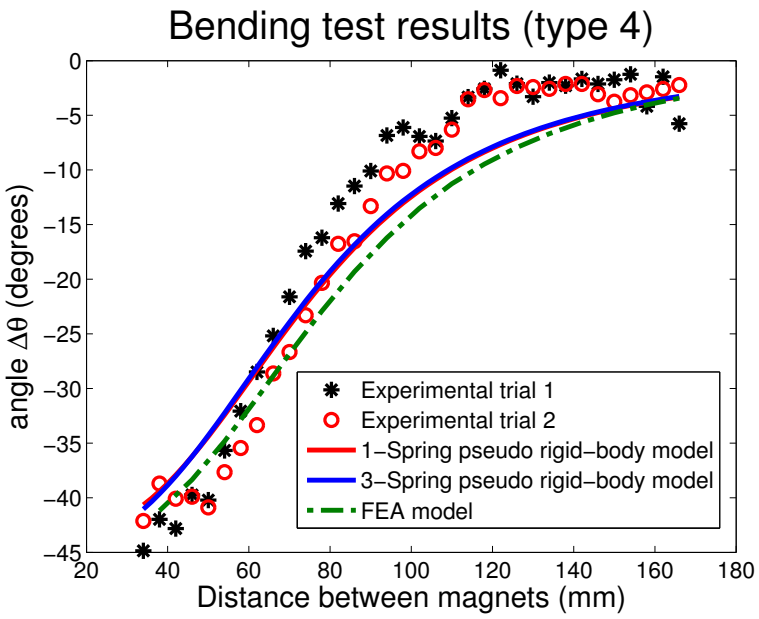

Figure 6.6: Experimental and modeling results for mechanism type 4

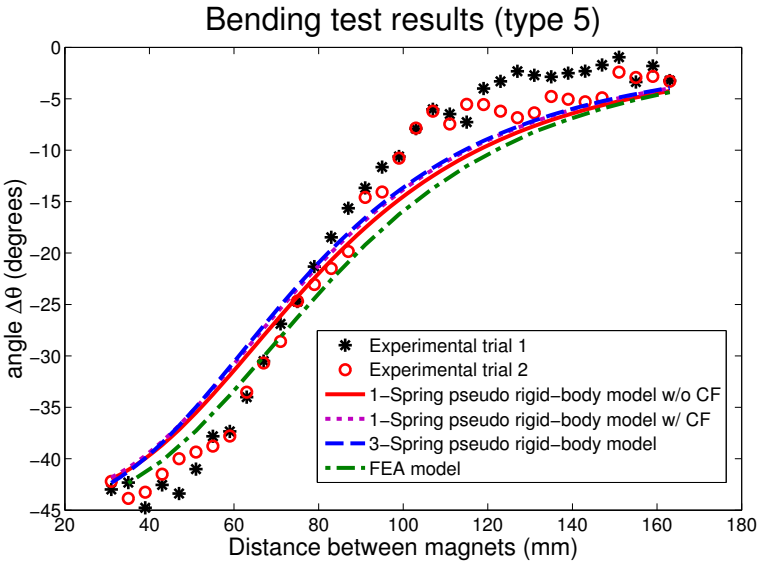

Figure 6.7: Experimental and modeling results for mechanism type 5

Table 6.1: MPE/RMSE for each model for each hinge type. Both PRB models for types 3 and 5 include correction factors.

	1-spring PRB		3-spring PRB		FEA	
	MPE	RMSE	MPE	RMSE	MPE	RMSE
Type 1	1.2%	2.2°	-0.10%	3.1°	-6.8%	3.2°
Type 2	1.9%	4.0°	3.3%	4.7°	-3.1%	4.5°
Type 3	-16.0%	6.4°	-14.6%	5.9°	-12.9%	10.4°
Type 4	-71.9%	3.9°	-69.7%	3.7°	-81.8%	4.5°
Type 5	-41.9%	3.6°	-40.3%	3.5°	-51.3%	3.8°

However, eliminating this factor produces a somewhat unfair comparison, as the difference in accuracy between the models is not due to the number of springs, but the effective length parameter.

For each mechanism type, each model is a fairly good match for the experimental data. The mean percent error (MPE) root mean square error (RMSE) for each type is reported in Table 6.1.

The highest errors are seen in mechanism types 3,4, and 5. Types 4 and 5 have very high MPE values, due to underpredicting the data more significantly at the experimental points near zero, which drives the MPE high quite quickly. However, their RMSE values are still relatively low, around 4°, meaning that the models predict the behavior of these mechanisms to within 4° on average. Additionally, the visually apparent error in types 4 and 5 may be somewhat exaggerated by the difference in scale compared to the plots for types 1-3. The worst performers in terms of RMSE are the models for type 3, with an error of up to 10.4°. This is particularly unexpected, as the models for types 4 and 5 (the two 135° samples) perform similarly well, but

the models for type 3 perform significantly worse than those for type 2 (the two 90° samples).

One initially considered possibility for the higher error on sample 3 might be the odd shape of its hinge. This could be taken as an indication that a simple scaling of the parameter l_{eff} is not sufficient to capture the hinge behavior. However, the FEA model has a similarly difficult time capturing the behavior of this hinge, which was not a problem at the meso-scale. There is a possibility that the FEA model is not accurately capturing the behavior of "oddly-shaped" hinges at the very small scale. However, as mentioned in the previous sections, the volume (and consequently the dipole magnitude, $\vec{m_d}$) of the small devices magnets was observed to vary by up to 20% in some cases. The 3-spring PRB model, subject to a sensitivity analysis of +/- 20% variance in the device magnet dipole (Figure 6.8, shows the behavior of the type 3 mechanism falls quite close to this bounds of this range, with the lower bound's MPE and RMSE reducing to 0.33% and 3.5° respectively, indicating variation in the magnitude of the device magnet is a strong possibility for the error in this sample.

Across all mechanism types, for the loading conditions presented here, the 1-spring and 3-spring PRB models are almost identical in performance. This is most likely due to the fact that the loading condition involves very low forces compared to the applied torques, making the loading conditions almost pure torque, rendering the performance of the two models functionally indistinguishable.

However, because the elastomer hinges do have the ability to stretch and fold

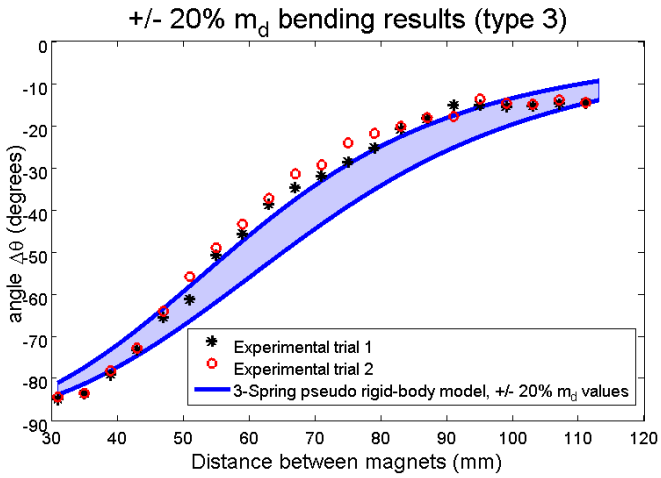

Figure 6.8: Bounds for a type 3 mechanism 3-spring PRB model varied by +/- 20%, compared with experimental data.

in ways that pin joints cannot, other loading conditions, such as those presented in the following section, will take more full advantage of the 3-spring PRB model than the mechanisms presented here.

6.5 Microrobotic leg modeling

The microrobotic leg mechanism was fabricated with the dimensions described in the previous sections, and a sample leg was used to estimate a robot's ability to clear a step of a given height.

6.5.1 Experimental setup

A leg mechanism's ground link was mounted to a stationary platform and allowed to rest over free space. A "step," in this case a long piece of silicon, 300 μm

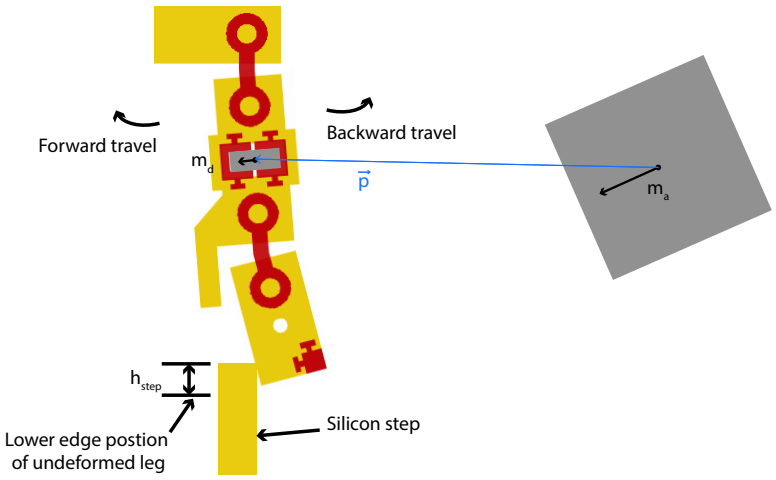

Figure 6.9: Schematic of the experimental setup for characterizing the leg mechanism's maximum step height.

wide, was rigidly affixed to the Thorlabs PT3-Z8 translational stage. The actuator magnet was placed at a distance $|\vec{p}| = 48$ mm in the x-direction, 0 initial y- and z-direction offset and an initial angular offset of 0. The actuator magnet was mounted on the Newport M-RS 40 rotational stage to allow an increasing angular displacement (Figure 6.9).

The position of the translational stage was finely adjusted until the corner position of the undeflected leg mechanism was known relative to the step. The step was then moved away from the leg, and to a desired step height. This was then brought into contact with the leg until the leading edge of the step was in line with the original axis of the leg, representing a moving leg's contact with an obstacle just under its position on the robot body.

The actuator magnet was then rotated slowly to an angular offset of 90° such that the leg's direction of travel was over the step. At a distance of 48 mm, this

corresponds to a maximum torque of 1.16×10^{-6} N-m if the device magnet in the leg is oriented perpendicularly to the actuator magnet orientation. In the case that the leg mechanism does not clear the step, the device magnet will remain in roughly the same position and orientation, while the actuator magnet's orientation is varied. In this case, the orientation offset between the two will become near 90°, and the leg will experience torques near the theoretical maximum.

6.5.2 Modeling

A model of the leg mechanism was created in MSC Adams View using the 3-spring pseudo rigid-body model. The spring constants were defined using equations 3.8 and 3.9 and the hinge geometry listed in the previous sections. The two hinges are identical.

MSC Adams allows the forces and torques on a body to be updated in real time based on the current configuration of the simulation, so the algorithm for finding the equilibrium deflection of the mechanism was not necessary for this model and was not used here. Instead, the instantaneous forces and torques on the point at the center of mass of the device magnet were determined by the applied rotation of the simulated actuator magnet and the resulting real-time angle of the simulated device magnet, according to equations 5.1 and 5.2.

The contacts between the two sides of the foot and the step, as well as the contacts between the two links of the leg at the kneecap were handled by contacts

with coefficients of static friction of $\mu_s = 0.5$, and coefficients of dynamic friction of $\mu_d = 0.3$ for the Si-Si contacts. For the PDMS-Si contacts, the coefficients used were $\mu_s = 1$ and $\mu_d = 0.5$. This range of frictional coefficients is supported by previous work [62].

6.5.3 Results and analysis

A range of step heights were attempted experimentally, from 50 μm to 300 μm using the described method. It was found that, for this configuration, the maximum step height the leg can successfully traverse is 100 μm. The leg was not able to pass over the step with a height increase to even 110 μm. After passing "forward" (as defined in Figure 6.9) over the 100 μm step, the direction of the magnet rotation was reversed and the leg was slowly brought back against the step in the "backward" direction. Due to the kneecap mechanical stop, the leg was not able to cross the 100 μm step in reverse, even with the full expected torque of 1.16×10^{-6} N-m applied. This result represents the intended behavior of the leg mechanism.

The model leg, set up using the magnetic dipole parameters characterized in Chapter 5, could traverse a step height of only 87 μm. However, with an increase of only 2% to the device magnet dipole magnitude, the leg was able to traverse a step of 102 μm, a step height increase of 17%. According to this model, the ability to traverse steps of a given height is highly dependent on the strength of the magnet embedded in the leg. The possibility of embedded a lower-than-average dipole magnet into one

Figure 6.10: Photograph of the MEMS hexapod with a bullet ant (*Paraponera clavata*).

of the legs should be considered during the design phase. Alternatively, a screening for higher-dipole magnets could be implemented at the cost of higher build times.

The leg model was additionally able to capture the behavior of the leg being stopped by its kneecap on the return once it has passed over the step.

6.6 A walking hexapedal microrobot

A walking hexapedal microrobot has been fabricated (Figure 6.10) and its initial performance characteristics have been investigated.

6.6.1 Description

Six of the legs described in the previous sections were fabricated attached to a central body in a configuration as shown in Figure 6.11. The hexapod is fabricated

Figure 6.11: Schematic of the hexapod before out-of-plane assembly. Yellow is silicon. Red is elastomer.

in a planar, unfolded state, then is folded out-of-plane and the sides are held in place with a small amount of Loctite 409 gel superglue.

In order to aid in the out-of-plane assembly, small acrylic assembly pieces were laser cut with sidewall angles of 0° or 10°. The flat hexapods–already assembled with device magnets in the legs, oriented in an alternating tripod fashion as recommended for the meso scale hexapods in Chapter 4–are put into the assembly pieces and held in place against the sidewalls using a small amount of water-soluble wax melted in place underneath the legs. A small amount of superglue is then placed between the robot body and the small slab of silicon where the legs are anchored on each side. The wax keeps the sides of the hexapod against the sidewalls and ensures that they are held at 0° or a slight splay angle of 10° while the glue is setting. Otherwise the glue will pull the sides of the hexapod in slightly during the curing process. The wax also provides a barrier between the hexapod and the assembly piece to prevent accidental affixing of the hexapod to the assembly piece. Once the glue is fully set, the water soluble wax is melted away with an overnight DI water soak. The final hexapod measures 4 mm x 4 mm x 5 mm, with a mass of 25 mg.

6.6.2 Walking performance

The hexapedal microrobot has thus far been demonstrated walking over mostly flat surfaces (though they need not be atomically flat, as a Si wafer) at fair speeds. One hexapod has been filmed walking at a sustained 9 mm/s (2.25 body lengths per second), over a distance of over 100 mm on a sheet of Delrin. The exact specifications of the setup for this result were not recorded. However, from inspection of the video it was measured that the actuator magnet was spinning at 7.5 Hz, or $\omega = 47$ rad/s, at an estimated 50 mm from the walking surface. The hexapod was also walking at an estimated 20 mm lead compared to the centroid of the actuator magnet, for an rough value $\vec{p} = (20, 52, 2)$ for any given device magnet during the duration of the test. Using the equations from the previous chapter for force and torque on a device magnet, this results in a theoretical maximum in-plane torque of $\tau_{max} = 0.6$ mN-mm and an in-plane force vector of f = (0.006, 0.024) mN when the actuator magnet dipole is oriented vertically and the device magnet in a leg is oriented horizontally.

The cost of transport of the micro hexapod is a dimensionless factor that can be used to compare the locomotion efficiency to that of other systems, including both biological systems and other mobile robots. The cost of transport can be defined as

$$COT = \frac{P}{mgv} \tag{6.3}$$

Here, P is the power used to move the micro hexapod, m is the mass, g is

Earth's gravity (g = 9.8 m/s^2), and v is the micro hexapod's forward velocity. For the results given above, a maximum power for each leg during actuation can be found by $P = \tau_{max}\omega$, where τ_{max} was the maximum torque applied to the device magnet and the actuator magnet spinning speed was used as ω. This assumes that the system is running below the step out frequency and the device magnets are actuated at the same frequency as the actuator magnet. Multiplying this result by the number of legs, 6, and using the given mass and sustained velocity, a maximum estimated cost of transport was found to be about 77. A table of costs of transport for an ant (for reference, calculated at about 13) as well as some existing micro robots can be found in [22].

While the result of 2.25 body lengths per second not yet in the ultimate targeted performance range of 10 body lengths per second, these are as yet unoptimized legs that have not yet pushed the limits of the fabrication process or taken advantage of the insights that the now-verified modeling methods can bring. Already, without these improvements, the performance is a marked improvement over other microrobots at this size, and is even approaching some biological systems. This can be seen in Figure 6.12, reproduced from Chapter 1 with the addition of the micro hexapod's best recorded performance.

A micro hexapod was also demonstrated walking across a variety of surfaces. At an actuator magnet distance of 43 mm from the walking surface (maximum τ = 1.4 mN-mm, f = (0, 0.047) mN when the actuator magnet is oriented vertically and

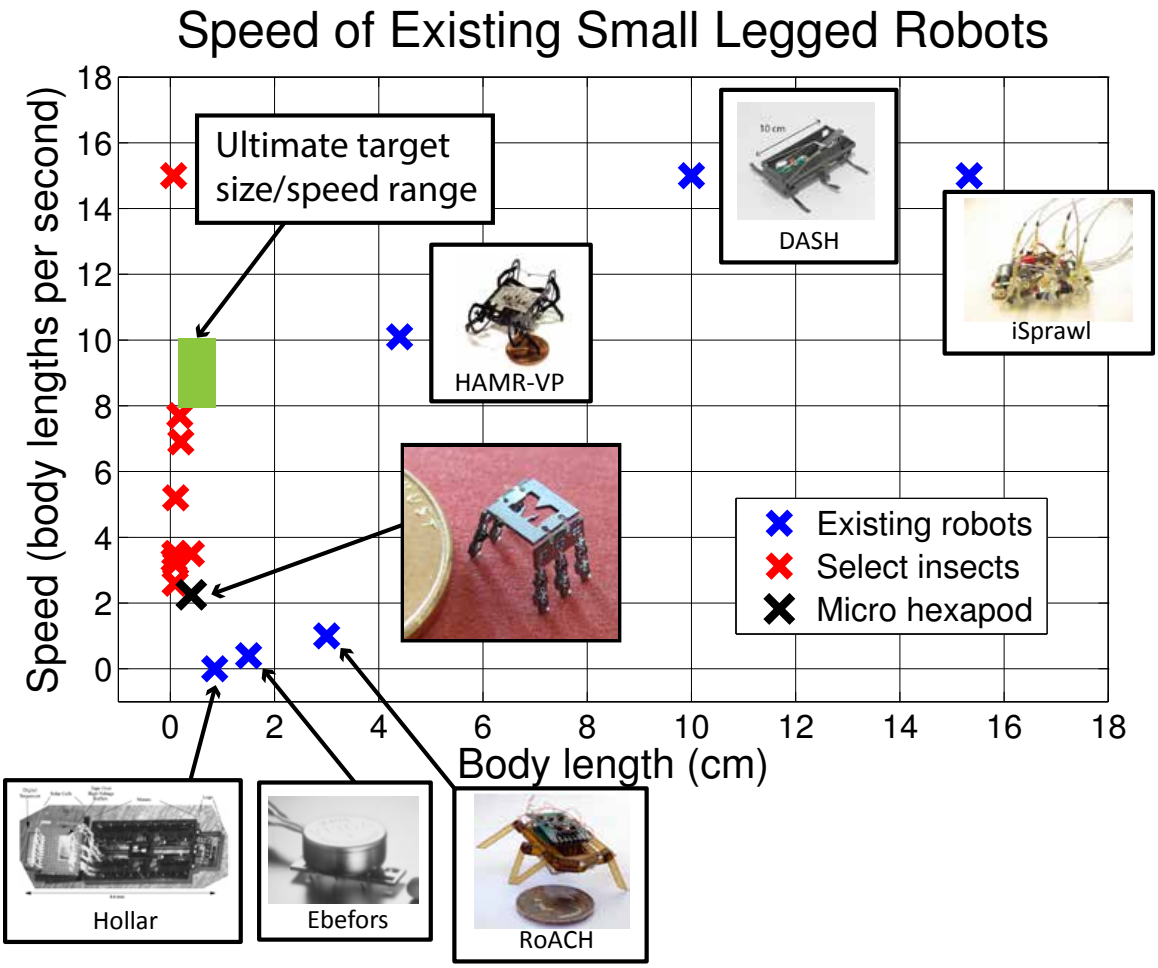

Figure 6.12: Speed vs. Body length of select insects and existing small robots, including the micro hexapod. Data on selected insects are from [1], [2], [3],[4], [5], and [6].

located 45 mm directly below the horizontally-oriented device magnet), an actuator magnet rotation speed of 6.8 Hz, and an actuator magnet translational speed of 2.9 mm/s, the hexapod was demonstrated taking at least a few steps over the following surfaces: Acrylic sheeting, spray-painted acrylic sheeting, plasticized paper film over acrylic, wetted plasticized paper film, common printer paper, wetted printer paper, P100 sandpaper, P320 sandpaper, and two 3D printed randomized terrains.

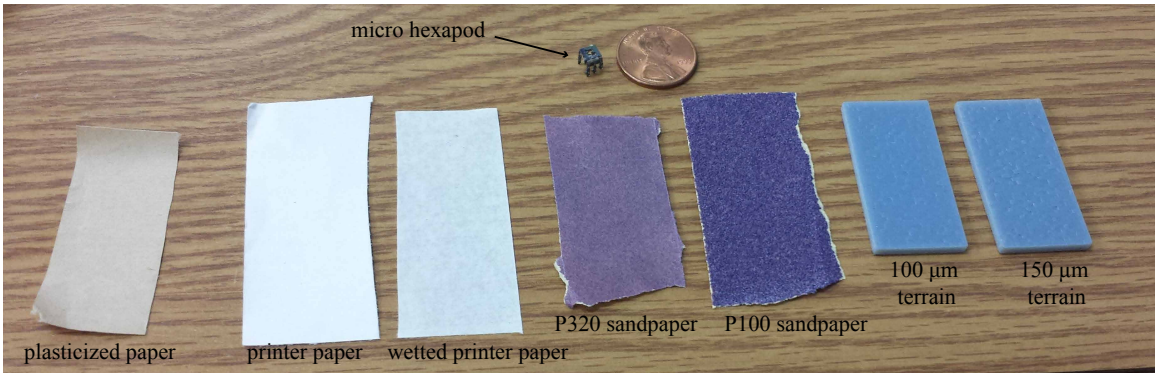

Figure 6.13: Terrains traversed by the micro hexapod. From left: plasticized paper film, printer paper, wetted printer paper, P320 sandpaper, P100 sandpaper, the 100 μm 3D printed terrain, and the 150 μm 3D printed terrain.

The 3D printed terrains are similar to those used in [63], with step lengths/widths of 1 mm. The two terrains were designed with maximum heights of 200 and 300 μm and average heights of 100 and 150 μm, respectively. They were printed on an Objet 30 Pro, with a reported layer thickness of 28 μm and accuracy of 100 μm.

A comprehensive analysis of the data obtained by these tests is still in progress, however, initial results indicate that the micro hexapod performs best on surfaces with some roughness but no large features (the paper surfaces, the spray painted acrylic, and the P320 sandpaper), somewhat worse on surfaces with roughness and large features (the two terrains and the P100 sandpaper), and poorly on very smooth surfaces (the flat acrylic sheeting) due to sticking of the feet. The performance on the wetted surfaces was worst, with only a few steps over these surfaces captured before the feet stick and can no longer be moved by the magnetic actuation of the legs.

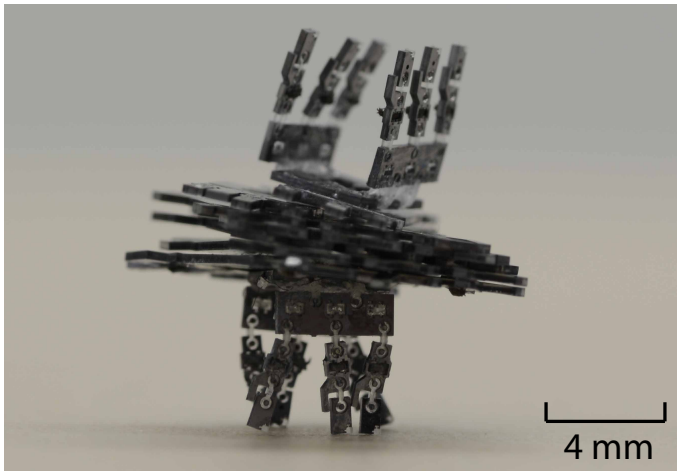

Figure 6.14: A 25 mg micro hexapod loaded with 495 mg. An additional payload mass of 25 mg caused the legs to buckle.

6.6.3 Load bearing capabilities

A micro hexapod was placed in a magnetic field applied by an actuator magnet at a distance 48 mm below the standing surface, oriented perpendicular to the standing surface. This magnet orientation simulates the hexapod's mid-stride configuration. The hexapod was loaded incrementally with 5 unfolded examples of a different hexapod design, weighing 43 mg each. Two unfolded hexapods of similar design to the standing hexapod were additionally placed, weighing 20 mg each. Finally, a folded hexapod of similar design to the standing hexapod, weighing 25 mg, was added. Upon the attempted placement of an additional folded hexapod, the legs of the standing hexapod buckled, resulting in a total load of 495 mg withstood in Figure 6.14. This corresponds to a standing payload capacity of about 20 X the robot's 25 mg mass.

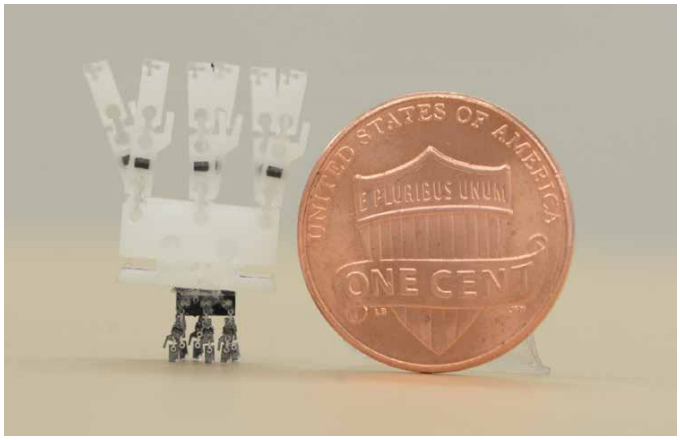

Figure 6.15: A 25 mg micro hexapod loaded with a 310 mg LaCER-fabricated hexapod.

An example of the 1 cm^3 walkers presented in Chapter 4, weighing 310 mg, was also demonstrated loading the micro hexapod (Figure 6.15).

Finally, the hexapod was observed walking over a printer paper surface in a magnetic field applied by a rotating actuator magnet at a distance of 45 mm below the walking surface. The hexapod was incrementally loaded with small and large unfolded silicon hexapods. The performance of the walking hexapod was similar or better to its unloaded performance with a single small hexapod load (20 mg), a single large hexapod load (43 mg), and with a single small and single large hexapod load (63 mg). With two large hexapods (86 mg), the performance of the walking hexapod was noticeably slower, jerkier and prone to collapse after only a few steps as the payload slipped under the more erratic body movements. With two large hexapods and a small hexapod payload (106 mg), the hexapod was no longer able to walk forward.

A properly balanced and well-affixed payload of 86 mg could possibly be more

consistently carried by the hexapod, resulting in a walking payload capacity of about 3.4 X the robot's mass. Compare to the robot in [14], which could carry greater than 30 X its own mass. However, this was achievable at a speed of less than 0.4 body lengths per second and over an atomically flat Si-wafer surface.

6.6.4 Micro hexapod conlusion

The fabrication, modeling, mechanism design and actuation characterization efforts presented in this work have come together to create a small, fast, strong walking microrobot. The micro hexapod, even with a non-optimized leg design has shown improvement over previous walking microrobots at a similar scale, to walk at 2.25 body lengths per second, walk over varied and rough terrain, and to carry up to 3.4 X its own body weight. Using the methods outlined by this work, improved leg mechanisms with optimized hinge geometry can be designed, fabricated, and tested more quickly than ever, putting microrobots with dimensions and performance rivaling those of antlike biological systems closer within our reach.

Chapter 6

Conclusion

This work in the fabrication, modeling, and design of micro robotic legs has led to a robust, magnetically actuated walking microrobot, as well a set of tools which could be used to aid in future designs of highly capable, untethered running microrobotic platforms. This document represents the work I have contributed toward this goal. The primary contributions of the this work are summarized as follows:

- An all-polymer meso-scale prototyping process for the fabrication of elasomteric robotic mechanisms, Laser Cut Elastomer Refill (LaCER).
- A MEMS fabrication process based on previous work by Gerratt et. al. ([23], [19]) and expanded to incorporate magnetic elements, with an improved magnet assembly process.
- A 3-spring pseudo rigid body (PRB) model consisting of two torsional springs and a linear spring arranged in series, for modeling miniature elastomeric hinges.
- A leg mechanism for a meso-scale hexapedal walking robot, used to demonstrate the LaCER process, the 3-spring PRB model, and optimization using the PRB model.
- Asymmetric underactuated robot leg designs for fabrication at the micro scale.

- A 1 cm^3 magnetically actuated walking hexapod fabricated using LaCER, using the best-performing asymmetric underactuated leg design, demonstrated walking at up to 10.6 body lengths per second.

- Magnetically actuated MEMS mechanisms fabricated the magnetic MEMS process.

- A verification of the 3-spring PRB model for micro scale mechanisms.

- A robust microrobot leg design, capable of clearing a step height of up to 100 μm.

- First steps of a magnetically actuated hexapedal microrobot, demonstrated walking at up to 2.25 body lengths per second.

- Demonstration of the hexapod's performance on varied terrain, and while carrying a payload up to 3.4 X its own mass.

Bibliography

[1] Alexandra Lipp, Harald Wolf, and Fritz-Olaf Lehmann. Walking on inclines: energetics of locomotion in the ant camponotus. *Journal of experimental biology*, 208(4):707–719, 2005.

[2] Robert J. Full, Daniela A. Zuccarello, and Alexa Tullis. Effect of variation in form on the cost of terrestrial locomotion. *Journal of Experimental Biology*, 150(1):233–246, 1990.

[3] David Berrigan and John RB Lighton. Energetics of pedestrian locomotion in adult male blowflies, protophormia terraenovae (diptera: Calliphoridae). *Physiological zoology*, pages 1140–1153, 1994.

[4] D Berrigan and JRB Lighton. Bioenergetic and kinematic consequences of limblessness in larval diptera. *Journal of Experimental Biology*, 179(1):245–259, 1993.

[5] John RB Lighton, George A Bartholomew, and Donald H Feener. Energetics of locomotion and load carriage and a model of the energy cost of foraging in the leaf-cutting ant atta colombica guer. *Physiological Zoology*, pages 524–537, 1987.

[6] TF Jensen and I Holm-Jensen. Energetic cost of running in workers of three ant species, formica fusca l., formica rufa l., and camponotus herculeanus l.(hymenoptera, formicidae). *Journal of comparative physiology*, 137(2):151–156, 1980.

[7] S. Kim, Jonathan E. Clark, and Mark R. Cutkosky. iSprawl: design and tuning for high-speed autonomous open-loop running. *The International Journal of Robotics Research*, 25(9):903–912, September 2006.

[8] P. Birkmeyer, K. Peterson, and R. S. Fearing. DASH: a dynamic 16g hexapedal robot. In *Proceedings of IEEE/RSJ International Conference on Intelligent Robots and Systems (IROS)*, pages 2683–2689, October 2009.

[9] Andrew T Baisch, Onur Ozcan, Benjamin Goldberg, Daniel Ithier, and Robert J Wood. High speed locomotion for a quadrupedal microrobot. *The International Journal of Robotics Research*, page 0278364914521473, 2014.

[10] A.M. Hoover, E. Steltz, and R.S. Fearing. RoACH: an autonomous 2.4g crawling hexapod robot. In *Proceedings of IEEE/RSJ International Conference on Intelligent Robots and Systems (IROS)*, pages 26–33, 2008.

[11] Bram GA Lambrecht, Andrew D Horchler, and Roger D Quinn. A small, insect-inspired robot that runs and jumps. In *Robotics and Automation, 2005. ICRA*

2005. Proceedings of the 2005 IEEE International Conference on, pages 1240–1245. IEEE, 2005.

[12] Kathryn A Daltorio, Andrew D Horchler, Stanislav Gorb, Roy E Ritzmann, and Roger D Quinn. A small wall-walking robot with compliant, adhesive feet. In *Intelligent Robots and Systems, 2005.(IROS 2005). 2005 IEEE/RSJ International Conference on*, pages 3648–3653. IEEE, 2005.

[13] Seth Hollar, Anita Flynn, Colby Bellew, and KSJ Pister. Solar powered 10 mg silicon robot. In *Micro Electro Mechanical Systems, 2003. MEMS-03 Kyoto. IEEE The Sixteenth Annual International Conference on*, pages 706–711. IEEE, 2003.

[14] Thorbjörn Ebefors, Johan Ulfstedt Mattsson, Edvard Kälvesten, and Göran Stemme. A walking silicon micro-robot. In *Proc. Transducers 99*, pages 1202–1205. Citeseer, 1999.

[15] Jeong Hoon Ryou and Kenn Richard Oldham. Dynamic characterization of contact interactions of micro-robotic leg structures. *Smart Materials and Structures*, 23(5):055014, 2014.

[16] Steven Floyd, Chytra Pawashe, and Metin Sitti. Microparticle manipulation using multiple untethered magnetic micro-robots on an electrostatic surface. In *Intelligent Robots and Systems, 2009. IROS 2009. IEEE/RSJ International Conference on*, pages 528–533. IEEE, 2009.

[17] Bruce R Donald, Christopher G Levey, Craig D McGray, Igor Paprotny, and Daniela Rus. An untethered, electrostatic, globally controllable mems microrobot. *Microelectromechanical Systems, Journal of*, 15(1):1–15, 2006.

[18] Dominic R Frutiger, Karl Vollmers, Bradley E Kratochvil, and Bradley J Nelson. Small, fast, and under control: wireless resonant magnetic micro-agents. *The International Journal of Robotics Research*, 29(5):613–636, 2010.

[19] Wayne A Churaman, Aaron P Gerratt, and Sarah Bergbreiter. First leaps toward jumping microrobots. In *Intelligent Robots and Systems (IROS), 2011 IEEE/RSJ International Conference on*, pages 1680–1686. IEEE, 2011.

[20] Aaron P Gerratt and Sarah Bergbreiter. Incorporating compliant elastomers for jumping locomotion in microrobots. *Smart Materials and Structures*, 22(1):014010, 2013.

[21] Wayne A Churaman, Luke J Currano, Christopher J Morris, Jessica E Rajkowski, and Sarah Bergbreiter. The first launch of an autonomous thrust-driven microrobot using nanoporous energetic silicon. *Journal of Microelectromechanical Systems*, 21(1):198–205, 2012.

[22] Sarah Bergbreiter. Effective and efficient locomotion for millimeter-sized microrobots. In *Intelligent Robots and Systems, 2008. IROS 2008. IEEE/RSJ International Conference on*, pages 4030–4035. IEEE, 2008.

[23] Aaron P Gerratt, Ivan Penskiy, and Sarah Bergbreiter. Soi/elastomer process for energy storage and rapid release. *Journal of Micromechanics and Microengineering*, 20(10):104011, 2010.

[24] J. A. Hetrick and S. Kota. An energy formulation for parametric size and shape optimization of compliant mechanisms. *Journal of Mechanical Design*, 121(2):229, 1999.

[25] Larry Howell. *Compliant mechanisms*. Wiley, New York, 2001.

[26] Elliot E Hui, Roger T Howe, and M Steven Rodgers. Single-step assembly of complex 3-d microstructures. In *Micro Electro Mechanical Systems, 2000. MEMS 2000. The Thirteenth Annual International Conference on*, pages 602–607. IEEE, 2000.

[27] LE Weiss, R Merz, FB Prinz, G Neplotnik, P Padmanabhan, L Schultz, and K Ramaswami. Shape deposition manufacturing of heterogeneous structures. *Journal of Manufacturing Systems*, 16(4):239–248, 1997.

[28] Robert J Wood, Srinath Avadhanula, M Menon, and Ronald S Fearing. Microrobotics using composite materials: The micromechanical flying insect thorax. In *Robotics and Automation, 2003. Proceedings. ICRA'03. IEEE International Conference on*, volume 2, pages 1842–1849. IEEE, 2003.

[29] JP Whitney, PS Sreetharan, KY Ma, and RJ Wood. Pop-up book mems. *Journal of Micromechanics and Microengineering*, 21(11):115021, 2011.

[30] Jorge G Cham, Sean A Bailey, Jonathan E Clark, Robert J Full, and Mark R Cutkosky. Fast and robust: Hexapedal robots via shape deposition manufacturing. *The International Journal of Robotics Research*, 21(10-11):869–882, 2002.

[31] Robert J Wood. The first takeoff of a biologically inspired at-scale robotic insect. *Robotics, IEEE Transactions on*, 24(2):341–347, 2008.

[32] Wojciech Bejgerowski, John W Gerdes, Satyandra K Gupta, Hugh A Bruck, and Stephen Wilkerson. Design and fabrication of a multi-material compliant flapping wing drive mechanism for miniature air vehicles. In *Proceedings of the ASME International Design Engineering Technical Conferences and Computers and Information in Engineering Conference (IDETC/CIE)*, pages 69–80. American Society of Mechanical Engineers, 2010.

[33] Jonathan Hiller and Hod Lipson. Automatic design and manufacture of soft robots. *IEEE Transactions on Robotics*, 28(2):457–466, 2012.

[34] BD Jensen, LL Howell, and LG Salmon. Design of two-link, in-plane, bistable compliant micro-mechanisms. *Journal of Mechanical Design*, 121(3):416–423, 1999.

[35] Shannon A Zirbel, Quentin T Aten, Melanie Easter, Brian D Jensen, and Larry L Howell. Compliant constant-force micro-mechanism for enabling dual-stage motion. In *Proceedings of the ASME International Design Engineering Technical Conferences and Computers and Information in Engineering Conference (IDETC/CIE)*, pages 191–198. American Society of Mechanical Engineers, 2012.

[36] E Yegan Erdem, Yu-Ming Chen, Matthew Mohebbi, John W Suh, Gregory TA Kovacs, BB Darling, and KF Bohringer. Thermally actuated omnidirectional walking microrobot. *Journal of Microelectromechanical Systems*, 19(3):433–442, 2010.

[37] AP Gerratt, B Balakrisnan, I Penskiy, and S Bergbreiter. Batch fabricated bidirectional dielectric elastomer actuators. In *Solid-State Sensors, Actuators and Microsystems Conference (TRANSDUCERS), 2011 16th International*, pages 2422–2425. IEEE, 2011.

[38] Dana E Vogtmann, Satyandra K Gupta, and Sarah Bergbreiter. Multi-material compliant mechanisms for mobile millirobots. In *2011 IEEE International Conference on Robotics and Automation (ICRA)*, pages 3169–3174. IEEE, 2011.

[39] Dana E Vogtmann and Sarah Bergbreiter. Magnetic actuation of ultra-compliant micro robotic mechanisms. In *Intelligent Robots and Systems (IROS), 2011 IEEE International Conference on*. IEEE, 2014, [submitted].

[40] D Vogtmann and S Bergbreiter. Magnetic actuation of thick film multi-material compliant mechanisms [in preparation]. *Journal of Micromechanics and Microengineering*, 2016.

[41] Dana E Vogtmann, Satyandra K Gupta, and Sarah Bergbreiter. Characterization and modeling of elastomeric joints in miniature compliant mechanisms. *Journal of Mechanisms and Robotics*, 5(4):041017, 2013.

[42] Wojciech Bejgerowski, John W. Gerdes, Satyandra K. Gupta, and Hugh A. Bruck. Design and fabrication of miniature compliant hinges for multi-material compliant mechanisms. *The International Journal of Advanced Manufacturing Technology*, 57(5-8):437–452, April 2011.

[43] Hai-Jun Su. A pseudorigid-body 3R model for determining large deflection of cantilever beams subject to tip loads. *Journal of Mechanisms and Robotics*, 1(2):021008, 2009.

[44] Larry L. Howell, Christopher M. DiBiasio, Michael A. Cullinan, Robert M. Panas, and Martin L. Culpepper. A pseudo-rigid-body model for large deflections of fixed-clamped carbon nanotubes. *Journal of Mechanisms and Robotics*, 2(3):034501, 2010.

[45] Guimin Chen, Daniel L Wilcox, and Larry L Howell. Fully compliant double tensural tristable micromechanisms (DTTM). *Journal of Micromechanics and Microengineering*, 19(2):025011, February 2009.

[46] Dana E. Vogtmann, Satyandra K. Gupta, and Sarah Bergbreiter. Multi-material compliant mechanisms for mobile millirobots. In *Proceedings of IEEE International Conference on Robotics and Automation (ICRA)*, pages 3169–3174, May 2011.

[47] Ellen M. Arruda and Mary C. Boyce. A three-dimensional constitutive model for the large stretch behavior of rubber elastic materials. *Journal of the Mechanics and Physics of Solids*, 41(2):389–412, February 1993.

[48] Dana E. Vogtmann, Satyandra K. Gupta, and Sarah Bergbreiter. Modeling and optimization of a miniature elastomeric compliant mechanism using a 3-spring pseudo rigid body model. In *Proceedings of the ASME International Design Engineering Technical Conferences and Computers and Information in Engineering Conference (IDETC/CIE)*, 2013.

[49] Aaron P Gerratt, Ivan Penskiy, and Sarah Bergbreiter. In situ characterization of pdms in soi-mems. *Journal of Micromechanics and Microengineering*, 23(4):045003, 2013.

[50] Sarah Bergbreiter, Aaron P Gerratt, and Dana Vogtmann. Progress toward mobility in microfabricated millirobots. In *Small-Scale Robotics. From Nano-to-Millimeter-Sized Robotic Systems and Applications*, pages 39–52. Springer, 2014.

[51] Ryan St. Pierre, Dana E. Vogtmann, and Sarah Bergbreiter. Model-based insights on the design of a hexapod magnetic walker. In *International Symposium on Experimental Robotics (ISER)*, 2014.

[52] Arthur W Mahoney and Jake J Abbott. Generating rotating magnetic fields with a single permanent magnet for propulsion of untethered magnetic devices in a lumen. *IEEE Transactions on Robotics*, 30(2):411–420, 2014.

[53] RW Ogden. Large deformation isotropic elasticity-on the correlation of theory and experiment for incompressible rubberlike solids. In *Proceedings of the Royal Society of London A: Mathematical, Physical and Engineering Sciences*, volume 326, pages 565–584. The Royal Society, 1972.

[54] ID Johnston, DK McCluskey, CKL Tan, and MC Tracey. Mechanical characterization of bulk sylgard 184 for microfluidics and microengineering. *Journal of Micromechanics and Microengineering*, 24(3):035017, 2014.

[55] K&J Magnetics, Inc: Neodymium magnet physical properties. https://www.kjmagnetics.com/specs.asp. Accessed: 2016-04-01.

[56] Rob J Hyndman and Anne B Koehler. Another look at measures of forecast accuracy. *International journal of forecasting*, 22(4):679–688, 2006.

[57] Newport: Fundamentals of vibration. http://www.newport.com/Fundamentals-of-Vibration/140234/1033/content.aspx. Accessed: 2016-04-01.

[58] Lionel Birglen, Clément Gosselin, and Thierry Laliberté. *Underactuated robotic hands*, volume 40. Springer, 2008.

[59] Aaron M Dollar and Robert D Howe. A robust compliant grasper via shape deposition manufacturing. *Mechatronics, IEEE/ASME Transactions on*, 11(2):154–161, 2006.

[60] B Moser, K Wasmer, L Barbieri, and J Michler. Strength and fracture of si micropillars: A new scanning electron microscopy-based micro-compression test. *Journal of materials research*, 22(4):1004–1011, 2007.

[61] D Vogtmann and S Bergbreiter. Adaptation of a 3-spring prb model for a magnetically actuated multi-material microrobot leg [in preparation]. *Journal of Mechanisms and Robotics*, 2016.

[62] Ivan Penskiy, Aaron P Gerratt, and Sarah Bergbreiter. Friction, adhesion, and wear properties of pdms coatings in mems devices. In *Micro Electro Mechanical Systems (MEMS), 2011 IEEE 24th International Conference on*, pages 440–444. IEEE, 2011.

[63] Daniel E Koditschek, Robert J Full, and Martin Buehler. Mechanical aspects of legged locomotion control. *Arthropod structure & development*, 33(3):251–272, 2004.